



**HAL**  
open science

# Prior Austenite Grain Size Controlled by Precipitates

Claire Leguen

► **To cite this version:**

Claire Leguen. Prior Austenite Grain Size Controlled by Precipitates. Mechanics [physics.med-ph]. INSA de Lyon, 2010. English. NNT: . tel-00511322

**HAL Id: tel-00511322**

**<https://theses.hal.science/tel-00511322>**

Submitted on 24 Aug 2010

**HAL** is a multi-disciplinary open access archive for the deposit and dissemination of scientific research documents, whether they are published or not. The documents may come from teaching and research institutions in France or abroad, or from public or private research centers.

L'archive ouverte pluridisciplinaire **HAL**, est destinée au dépôt et à la diffusion de documents scientifiques de niveau recherche, publiés ou non, émanant des établissements d'enseignement et de recherche français ou étrangers, des laboratoires publics ou privés.

Thèse

# Prior Austenite Grain Size Controlled by Precipitates

présentée devant  
L'Institut National des Sciences Appliquées de Lyon

pour obtenir  
le grade de docteur

Ecole doctorale : Matériaux de Lyon.  
Spécialité : Matériaux

par  
Claire LEGUEN

Soutenue le 5 mars 2010 devant la Commission d'examen

Jury

Yves BRECHET	Président
Chad SINCLAIR	Rapporteur
Alan CRAVEN	Rapporteur
Michel PEREZ	Directeur de thèse
Thierry EPICIER	Directeur de thèse
Daniel ACEVEDO	Examineur
Thomas SOURMAIL	Invité



# Contents

<b>Introduction</b>	<b>I</b>
<b>I Quantification by EELS spectroscopy</b>	<b>7</b>
I.1 Problematic: Quantitative chemical analysis of carbonitrides in TEM	7
I.2 Background on EELS	10
I.2.1 Experimental technique	10
I.2.2 Pre-treatment of EELS spectra	12
I.3 Methods to quantify chemical species in EELS	14
I.3.1 Basic method	14
I.3.2 Least Mean Square Fitting	15
I.3.3 Jump Ratio	16
I.3.4 Second derivative	18
I.3.5 Conclusion on methods for quantifying chemical species in EELS	19
I.4 Material and treatments	20
I.5 Principle of chemical species quantification	20
I.6 Results and discussion	25
I.6.1 Verification of the references	25
I.6.2 Experimental spectra treatment	25
I.7 Conclusion of the chapter	31
<b>2 Role of nitrogen</b>	<b>33</b>
2.1 Materials and heat treatment	34
2.1.1 The 60SiCrV7+Nb industrial steel	34
2.1.2 Elaboration and heat treatments of FeVNbCN microalloyed steel	35
2.2 Experimental techniques	38
2.2.1 Transmission Electron Microscopy	38
2.2.2 Determination of particles radius	43

---

2.2.3	Precipitate volume fraction . . . . .	43
2.3	Experimental results . . . . .	45
2.3.1	The 60SiCrV7+Nb industrial steel . . . . .	45
2.3.2	The FeVNbCN model alloy . . . . .	49
2.3.3	Comparison of both industrial and model alloys . . . . .	58
2.4	A model for precipitation kinetics . . . . .	60
2.4.1	Hypothesis . . . . .	60
2.4.2	Thermodynamic of carbides, nitrides and carbonitrides . . . . .	61
2.5	Conclusion . . . . .	73
<b>3</b>	<b>Correlation between the precipitation state and grain growth</b>	<b>75</b>
3.1	Materials and treatments . . . . .	77
3.1.1	16MnCr5+Nb industrial steel steel . . . . .	77
3.1.2	FeVNbCN model alloy . . . . .	80
3.2	Experimental techniques . . . . .	81
3.2.1	Characterization of the precipitation state . . . . .	81
3.2.2	Characterization of the Prior Austenite Grain Size . . . . .	81
3.3	Experimental results . . . . .	82
3.3.1	Austenitic grain size of the 16MnCr5+Nb . . . . .	83
3.3.2	Austenitic grain size of the FeVNbCN microalloyed steel . . . . .	88

# Introduction

## Context

ASCOMETAL is specialized in manufacturing special steel components and covers a wide range of applications in automobile, mechanical, springs and bearings domains. These *special steels* are high performance steels used for mechanical components demanding a high level of quality and security.

High temperature thermo-mechanical processes are commonly involved during processing. Austenite grain growth occurs during high temperature exposure of low and medium alloy steels. Mechanical properties are negatively impacted by a large Prior Austenite Grain Size (PAGS). To enhance steel performances, microalloying elements can be added, such as vanadium, niobium, titanium and aluminium. During thermo-mechanical treatments these elements may form carbide, nitride or carbonitride precipitates. These precipitates have long been recognized as an efficient way to restrict the austenite grain growth, and to induce structural hardening, according to their nature and history. Microalloying is therefore widely used, for example, in modern spring or carburizing steel grades. For clarity, we will briefly develop here treatments performed on spring and gear steels, two kinds of steel that will be studied in this work:

◇ Steels for surface treatments such as gear steels:

Steel for surface treatments have generally a carbon content ranging from 0.1 to 0.3 % in weight. The choice of the grade depends on searched end-use properties (hardenability, mechanical properties, ...). The hot rolling can be followed by a step of hot forming and by an air cooling. Then an isothermal annealing over the  $A_{c3}$  temperature is performed. It is followed by a cooling to the pearlitic nose and a holding at this temperature. A cold forming is frequently performed on these steels, after the hot rolling or the isothermal annealing. This forming enables to obtain complex shaped components with



Figure 1: *Gears are made of specific steels for surface treatments. A cold forming is frequently performed on these steels to obtain complex shapes with good surface conditions.*

very good surface conditions. After the cold forming, a surface treatment, such as carburizing or carbonitriding, is performed at high temperature (between  $880^{\circ}\text{C}$  and  $1050^{\circ}\text{C}$ ) followed by a quench.

◇ Spring steels at bulk hardening and annealing state:



Figure 2: *Springs require high yield strength and high impact resistance in order to get the best fatigue behaviour and durability.*

In this range, the choice of the steel is a compromise between several properties such as a high durability or elasticity limit, an impact resistance as high as possible and the best fatigue behaviour. After hot rolling, an isothermal austenitizing treatment is performed, during which the steel is rolled up, and, quenched to obtain a martensitic structure. In these kinds

of steels alloying elements, and in particular carbon, silicon, manganese, chromium and vanadium, lead to an increase of the hardness. Chromium also increases the hardenability, and thus is used for a full hardening of large pieces. The quenched state is then tempered at a temperature lower than 500°C.

During treatments over the  $A_{c3}$  temperature performed on gear and spring steels (the carburizing and austenitizing treatments), the precipitation state evolves leading in general to a decrease of the precipitate volume fraction and to an increase of the precipitate size. Under these conditions, precipitates will not contribute any more to the improvement of mechanical properties, and in particular, to the control of the austenitic grain growth. Moreover, Abnormal Grain Growth (AGG), which is the growth of one large grain at the detriment of its smaller neighbors, may appear, leading to undesirable mechanical instabilities (cavitation, rupture). Thus, it is important for the industry to understand the evolution of the precipitation state during these heat treatments.

Moreover, in order to improve the industrial process, and therefore reduce the costs, it is desirable to perform shorter treatments at higher temperatures. This raises a considerable question: “how far can we go?”

## My PhD project

To shed some light on the above, it is important to understand the evolution of the precipitation state and of the related prior austenite grain size. Therefore, predictive tools are needed to understand these evolutions. The aim of this thesis is then to create and/or improve the link between thermo-mechanical treatments, the precipitation state and the prior austenite grain size.

First, the precipitation state has to be finely characterized:

- The **precipitated volume fraction** must be measured. It has been done by Inductively Coupled Plasma (ICP) spectroscopy coupled to an electrolytic dissolution.
- **Precipitate size distribution** is to be determined. It has been obtained using High Angle Annular Dark Field (HAADF) images in Transmission Electron Microscopy (TEM). This technique has been successfully used during D. Acevedo’s PhD [Acevedo 07].
- **Chemical composition** of precipitates must be known. For metallic elements (Nb, V, Ti, Al), EDX in TEM will be used. In general, industrial steels contain nitrogen, which can form nitrides or carbonitrides

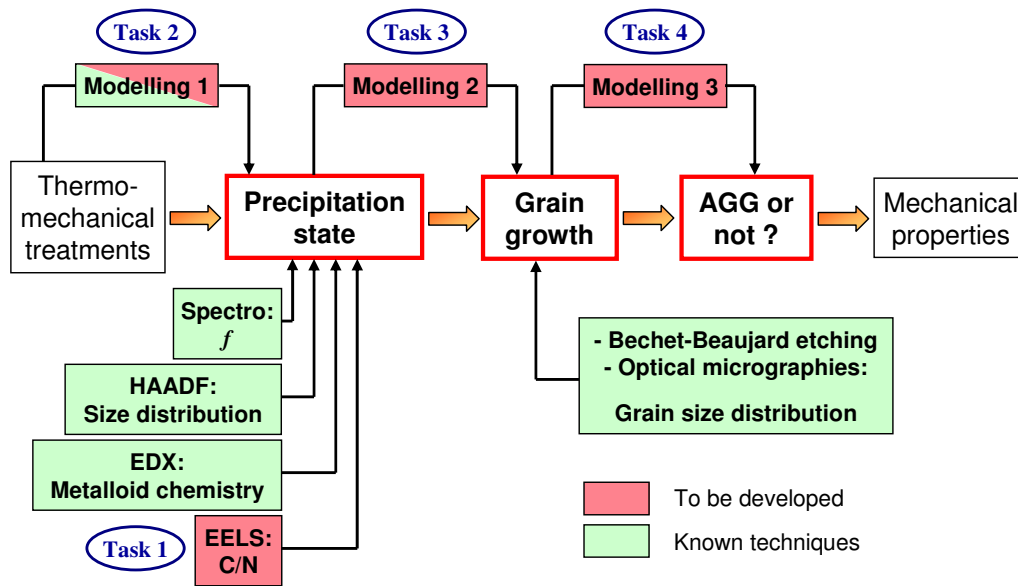


Figure 3: Schematic diagram explaining the major tasks of this project.

if combined with carbon. EDX does not allow the quantification of light elements (C and N), thus another technique is needed: EELS is an excellent tool to measure the chemical composition of sub-micrometric precipitates in such light elements. However, there is no adequate method to treat EELS spectra of complex carbonitrides such as (Nb,V,Ti)(C,N). Thus, a routine has to be developed to analyze the chemistry of these precipitates.

Then, a model is needed to link heat treatments and the precipitation state. Indeed, experimental procedures could be difficult and long to establish. Thus, the modelling can be useful to predict the precipitation state obtained after complex industrial heat treatments and this, without performing systematic experimental characterizations.

Once the precipitation state is finely characterized, the prior austenite grain size (representative of a high temperature microstructure that has been lost during cooling) needs to be determined. To do so, a special etching, which reveals the austenite grain boundaries is performed, followed by optical micrography analysis. A combination of the former precipitation model and a model predicting the austenitic grain size for a given (and evolving) precipitation state enables to predict the prior austenite grain size evolution during heat treatments.

Finally, the importance of controlling the grain growth and, in particular, to avoid abnormal grain growth, has been quoted. Thus, a model is needed to predict the risk of abnormal grain growth for a given precipitation state.

## **Project structure and content of the manuscript**

Along this project, several tasks will be developed to understand and to predict the precipitation state and prior austenite grain size evolution. These tasks are presented in the following.

Chapter 1 is dedicated to the implementation of a routine to treat EELS spectra of complex carbonitrides (task 1). Firstly, the experimental technique is presented, and then a survey on existing methods is given. A new method, well adapted to the characterization of complex carbonitrides will be described. Finally, the routine will be validated on complex (Ti,Nb,V)(C,N) precipitates of an industrial spring steel.

To understand the precipitation state and prior austenite grain size evolution in industrial grades, model alloys can be elaborated with compositions close to those of industrial steels. The aim is to analyze these evolutions in steels whose composition is controlled and therefore well known. In our study, a FeVNbCN model alloy has been elaborated to understand the role of the nitrogen in the evolution of the precipitation state. Its precipitation state will be characterized in Chapter 2. Experimental results will be compared with those of the 60SiCRrV7+Nb industrial spring steel studied during the PhD of D. Acevedo [Acevedo 07], in order to have a better understanding of its experimental results. With the same logic, a model predicting the precipitation kinetics, based on classical nucleation and growth theories, will be proposed to link heat treatments and the precipitation state (task 2). This model will deal with the formation of carbonitrides in order to evaluate the influence of the nitrogen.

In Chapter 3, grain size distributions of the FeVNbCN model alloy and of an industrial gear steel will be given. The aim of this chapter is to present a correlation between the precipitation state and the prior austenite grain size for these two steels. First we will present an experimental correlation. Then, a combination between the precipitation model developed in the previous chapter and a model to predict equilibrium austenitic grain size will be used to understand the evolution of the prior austenite grain size during austenitizing treatments (task 3), i.e. when the precipitation state evolves.

The Chapter 4 is dedicated to the definition of a criterion predicting the risk of abnormal grain growth (task 4). This criterion is based on a previous model from the literature, that had to be improved in order to account for complex precipitate size distributions, as encountered within this work. The new criterion will be applied on both the FeVNbCN model alloy and the industrial steel.

The last chapter summarizes the major conclusions of this project and details some prospects, that could be fruitfully developed in a near future.

Note that every chapter of this manuscript encapsulate its own problematic and therefore could be red separately.

## CHAPTER 1

# Quantification of the chemical composition of carbonitrides by EELS spectroscopy. Application to an industrial alloy

In this chapter we will present a new method to quantify by Electron Energy Loss spectroscopy (EELS) the chemical composition of carbonitrides and, in particular, nitrogen and carbon, which can not be reliably analyzed by EDX.

At first we will introduce the principle of EELS, then we will give the different stages of the preliminary treatment of spectra. Finally, after a presentation of different techniques to analyze the chemistry of carbonitrides, we will expose the method used in this work.

### **I.1 Problematic: Quantitative chemical analysis of carbonitrides in TEM**

During this project, we will characterize the precipitation state evolution during reversion treatments. Different techniques can be used for this:

- The volume fraction is determined by electrolytic dissolution (see Chapter 2 paragraph 2.2.3).
- The precipitates crystallography can be obtained by the analysis of diffraction patterns.
- The precipitates size can be measured using High Angle Annular Dark Field (HAADF) images (see Chapter 2 paragraph 2.2.2 or using Scan-

ning Electron Microscopy (SEM) micrographs in Scanning Transmission Electron Microscope (STEM) mode [Acevedo 07].

- The chemical composition of nanometric precipitates has to be analyzed using the Transmission Electron Microscopy (TEM), which is presented in details in chapter 2.

There are two major problems for this chemical analysis:

1) The classical preparation of samples involves making thin foils, in which precipitates are buried. Under such conditions, the signal-to-noise ratio of the analysis is low due to the nanometric size of particles. Furthermore, contamination by amorphous carbon frequently exists, which makes any carbon quantification extremely delicate. An illustration is presented in figure 1.1 where the analysis of vanadium carbides is performed using EELS (this technique will be developed in section 1.2.1). This figure shows two EELS spectra performed on two precipitates  $V_6C_5$  in a thin foil FeCV (700°C - 15 hours, sample elaborated by D. Acevedo [Acevedo 07]). The green spectrum is obtained without significant contamination: the analysis leads to  $C/V = 0.84 \pm 0.03$ ; while the red spectrum corresponds to a massive contamination due to a carbon pollution (C-K edge is dominated by the second “peak” around 296 eV, characteristic of amorphous carbon). In this example, we obtained a spectrum without amorphous carbon because the precipitate is large enough, so the carbon in the matrix is not analyzed. Moreover, it is sometime possible to analyze a precipitate without amorphous carbon, but this is extremely uncommon and it is not possible to make a reliable quantitative study in those conditions.

To quantify the carbon and nitrogen Craven et al. made carbon extraction replica thin enough so that numerous holes and cracks can be formed. In such conditions some precipitates, which overhung the edge of the carbon film, could be analyzed without presenting an amorphous C-K edge [Craven 00a]. However this technique can be difficult to implement and all precipitates cannot be analyzed.

Thus, for all these reasons we made extraction replicas, which were not made of carbon. As Courtois *et al.* [Courtois 06], Scott *et al.* [Scott 02] and Crooks *et al.* [Crooks 81] these replicas are made of aluminium or oxidized aluminium ( $AlO_x$ ). The protocol for carrying replicas is given in appendix A.

2) The second point is to measure effectively and reliably the chemistry of complex carbonitrides (Ti,V,Nb)(C,N). For metallic elements, such as niobium, vanadium and titanium, the EDX analysis may be sufficient. EDX

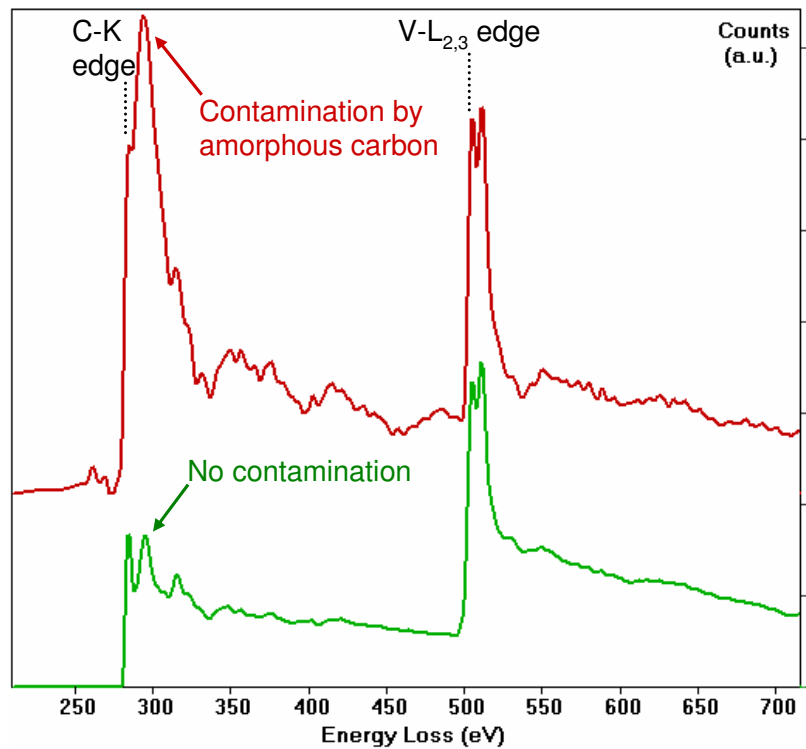


Figure 1.1: *Two EELS spectra from vanadium carbides in a thin foil. The first one (green curve) does not show amorphous carbon while the second one (red curve) shows a massive contamination due to carbon pollution. The presence of amorphous carbon makes the determination of the exact precipitate chemistry harder.*

further presents the advantages of being reliable and fast. But, in the case of light elements (carbon and nitrogen), quantitative and accurate EDX analysis is considered impossible. Thus, we need another technique to measure the chemistry: EELS. This raises the question of the quantification method to be used in EELS. All along this project, we will discuss of the precipitation state evolution during reversion treatments. Therefore, this point is of great importance for all measurements performed during this study, and it is thus worth developing both the EELS technique and the possible quantification methods, to conclude with the approach that we have used here.

There is as well, an interest in modelling to know the exact composition of precipitates. Previous works show that to model the precipitation state evolution, the knowledge of the exact precipitates chemistry is necessary and in particular the composition of carbon and nitrogen [Acevedo 07]. Thus, the modelling of  $M(C,N)$  or  $(M,M')(C,N)$  precipitate type will enable to have a better understanding of the phenomenon of reversion in the model alloy

FeVNbCN , as it will be presented in next chapter.

## 1.2 Background on EELS

### 1.2.1 Experimental technique

As said above, EELS has been used in the present work for a quantitative analysis of the carbon and nitrogen contents of the precipitates, since this technique is better adapted than EDX for light elements. Furthermore, EELS can give information on the atomic and crystallographic local environment of the probed atoms. The collected signal consists in incident electrons, which have lost an energy  $\Delta E$  throughout the sample. The energy loss experienced by primary electrons, thus transferred to the target atoms, is mainly dissipated in the emission of visible photons, X photons or Auger electrons; EELS concerns only the particular case involving the formation of an electron-hole pair, where the hole is located on a heart level of an atom.

The acquisition of spectra is performed using a spectrometer with parallel detection, in our case a digiPEELS Gatan 766 model placed under the column of the JEOL 2010F microscope. It is a magnetic prism curved at  $90^\circ$  where the electrons are dispersed according to their energies. The spectrum is recorded on a strip of photodiodes (1024 diodes). An amplifier provides a variable dispersion from 2 to 0.05 eV/channel. The acquisition of a spectrum can be made when the microscope is in image mode or diffraction mode. In our case, all data were recorded in the so-called “image-coupling” mode, where a diffraction pattern is obtained on the screen, thus enters in the spectrometer.

The collection angle  $2\beta$  is the maximum angle of “acceptance” of electronic trajectories analyzed by EELS. It is an experimental parameter, the value of which has a great influence on the total electron intensity collected. In all cases it is necessary to have  $\beta > \theta_E$  where  $\theta_E$  is a characteristic angle of ejection of electrons involved in studying a given edge and given by:  $\theta_E = E_{edge}/2E_o$  with  $E_o$  the energy of incident electrons (200 keV) and  $E_{edge}$  the energy loss of the edge of interest [Egerton 86] (see figure 1.2). In the “image-coupling” mode, the collection half-angle is defined by the relationship:

$$\beta = \frac{d}{2L} \times \frac{b}{b'} \quad (1.1)$$

where  $d$  is the diameter of the spectrometer entrance (mm),  $L$  the camera length,  $b$  the distance between the cross-over and the screen, and  $b'$  the distance between the cross-over and the entrance of the spectrometer. For the

JEOL 2010F microscope, the factor  $h/h'$  was previously measured to 0.56.

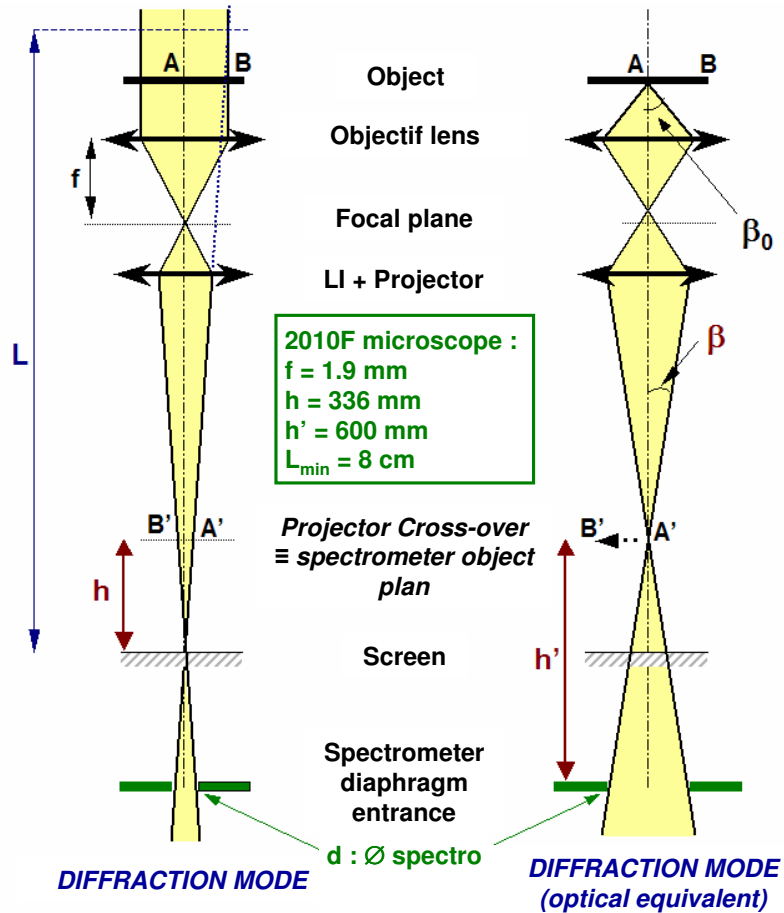


Figure 1.2: Schematic presentation of the collection angle  $2\beta$ .

A typical EELS spectrum is shown in Figure 1.3.

The first region corresponds to the *Zero Loss* intense peak due to elastic electrons. The lower is the *Zero Loss* peak width (or Full-Width at Half Maximum *FWHM*), the better is the energy resolution. In the case of the Shottly-field emission gun of the JEOL2010F microscope, the energy-resolution of the microscope was measured to be  $(0.75 \pm 0.05) \text{ eV}$  under the best instantaneous acquisition conditions, and about  $(1 \pm 0.2) \text{ eV}$  under realistic working acquisition conditions.

The second area is that of low losses. It begins after the *Zero Loss* and spans several tens of electron volts. This region corresponds to the plasmons excitations, that is the collective oscillation of free electrons. The intensity and

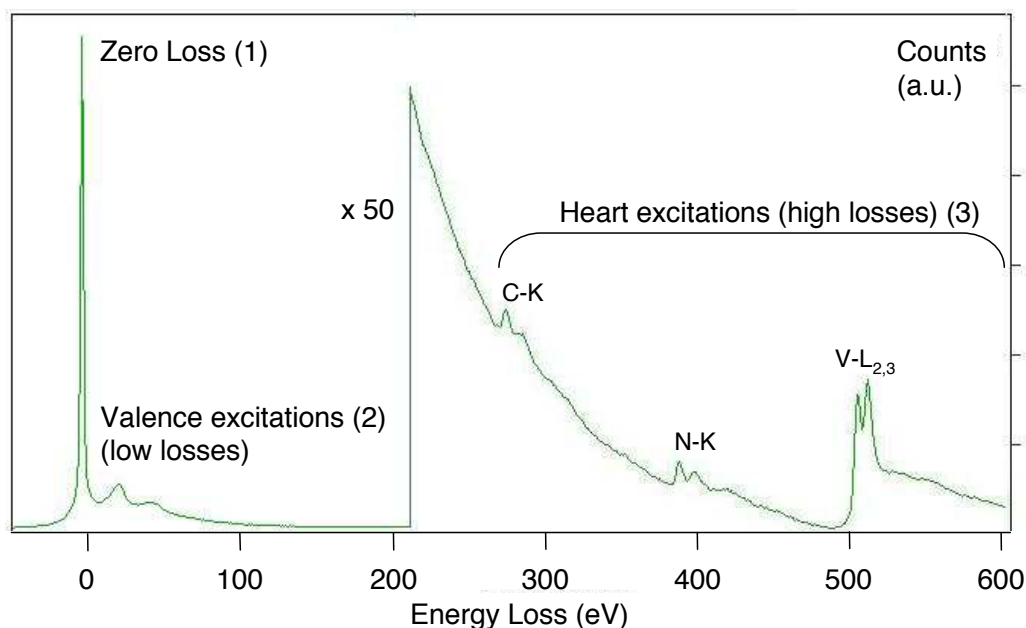


Figure 1.3: *EELS spectrum obtained on a vanadium carbonitride.*

the number of plasmon peaks increases with the thickness of the sample.

Finally, the third area is that of core losses. It typically starts around 50 eV and extends to several thousands electron-volts. It corresponds to excitations of atomic electrons from well-localized internal atomic levels, to Bloch free states and/or to the *continuum* (corresponding to ionization events). In the EELS spectrum, ionization edges or edges onset at energy corresponding to the binding energy of heart electrons, and are superimposed on a continuously decreasing background, which can be approximated by a power-law.

### 1.2.2 Pre-treatment of EELS spectra

In order to quantify the ionization edges, a dedicated treatment of EELS spectra must be performed in three steps. The first step is to correct the spectrum from “noises” related to the acquisition conditions: a first background noise, or “black noise” from the electronic noise acquired by diodes, and a second gain or “white noise”, associated with the non-uniform response of these diodes. The second stage involves the subtraction of the continuous background under the edges, extrapolated by a power-law. The third step is to deconvolve the edges from the multiple scattering. Experimentally the recorded edges are the result of a convolution of the intrinsic edge, or simple diffusion signal, by the low-loss region (see figure 1.4). This means

that an electron suffering the characteristic plasmon energy loss  $E_p$ , and exciting a core atomic electron at the energy  $E_s$ , will sustained a total loss  $E_p + E_s$ . Thus, the corresponding edge will consist in a major signal of simple diffusion (true diffusion), increased by a contribution due to the plasmons (multiple diffusion). A dedicated deconvolution treatment has to be performed in the case of thick samples (typically, thicknesses larger than 0.2-0.3 in  $\lambda_p$  units [Egerton 86], that is typically for thicknesses larger than 20-30 nm).

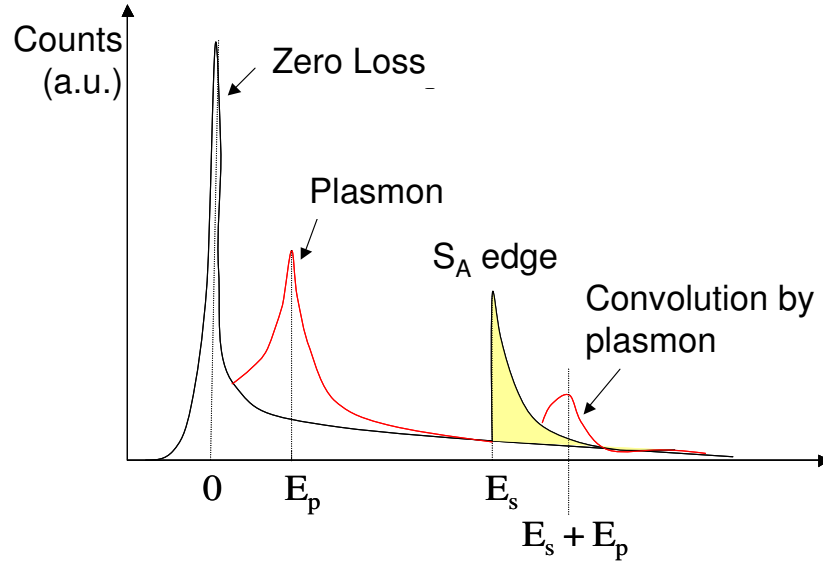


Figure 1.4: Scheme of the convolution by plasmons.

For that purpose, the most often used technique is the so-called Fourier ratio method, which consists in retrieving the true signal  $R_{true}(E)$  by dividing the Fourier transform ( $TF$ ) of the experimental spectrum by that of the low-losses regions  $R_{plasmon}(E)$ , and then Fourier back-transforming this ratio.

$$R_{true}(E) = TF^{-1} \frac{TF[R_{exp}(E)]}{TF[R_{plasmon}(E)]} \quad (1.2)$$

with  $R_{exp}(E) = R_{true}(E) \otimes R_{plasmon}(E)$  where  $\otimes$  means a convolution product.

From a numerical point of view, the Fourier transform will be performed by a Fast-Fourier Transform algorithm ( $FFT$ ). In order to minimize artifacts due to the truncature of the signal during this  $FFT$ , it is necessary to ensure that

the spectra to deal with does not present discontinuities at their extremities, which would lead to undesired oscillations in the result. This condition is naturally fulfilled after subtracting the continuous background (with a power law of type  $AE^{-r}$  where  $E$  is the energy loss and  $A$  and  $r$  are constants), which brings the starting and end regions of the spectrum to zero. The code used for these treatments is implemented in a software developed by T. Epicier to treat EELS spectra.

## 1.3 Methods to quantify chemical species in EELS

### 1.3.1 Basic method

The first case we can discuss in terms of chemical quantification corresponds to the absolute measurement of the quantity of a given element present in the sample. This element can be identified by the shape and position of some ionization edges in the EELS spectrum. In the ideal case, the spectrometer collects electrons in a solid angle large enough to detect all the elastic and inelastic electrons, or for the latter, an energy window sufficiently large for measuring the total intensity  $I_X$  of the ionization edge. This intensity is linked to the number of probed atoms (say,  $N$  atoms per unit area). It depends directly on the probability  $P_X$  that an incident electron excites the probed atomic transition (Type X = K, L ...): thus, in the case of a K transition,  $I_K$  can be written as [Egerton 86]:

$$I_K = \frac{t}{\lambda_K} \exp\left(-\frac{t}{\lambda_K}\right) I = N\sigma_K \exp(-N\sigma_K) I \quad (1.3)$$

where  $I$  represents the intensity of the incoming electron beam,  $t$  the sample thickness,  $\lambda_K$  and  $\sigma_K$  the mean free path and the effective cross-section for the ionization of the layer K and  $N$  the number of probed atoms per unit area. The value of  $\lambda_K$  for internal layers is a few micrometers and that of the thickness  $t$  does not exceed 100 nm in practice to obtain a good edge signal over the background. We can therefore estimate the exponential factor close to unity, giving:

$$I_K = N\sigma_K I \quad (1.4)$$

This expression allows the absolute determination of  $N$ , providing that the exact incoming intensity is known. In practice, we mostly need to determine the ratio between say two elements A and B (a particular case of the general case where more than two species are present), and a relative measurement is then

sufficient. It is possible to quantify each atomic species present in the sample volume studied by measuring the area  $I_A$  or  $I_B$  under the corresponding ionization edge after background subtraction. Since this background is extrapolated, it is better to integrate the electron intensity over a limited energy window  $\Delta$  in order to minimize the errors due to that extrapolation (see paragraph 1.2.2). Cross sections  $\sigma_K(\beta, \Delta)$  are obtained by atomistic calculations (hydrogenic model or Hartree-Slater calculations well described in [Egerton 79] and [Leapman 80] respectively). They depend upon the solid angle of collection  $\beta$ . Tabulated values or parameterized analytical expressions for these cross-sections are available in the processing software used: in our case, the EL/P software provided by Gatan, or a software written by T. Epicier, containing the codes developed by R.F. Egerton [Egerton 86]. Thus, the ratio of the numbers of atoms  $N_A$  and  $N_B$  in the area of analysis is given by:

$$\frac{[N_A]}{[N_B]} \approx \frac{\sigma_j^B(\beta, \Delta) \times I_K^A(\beta, \Delta)}{\sigma_j^A(\beta, \Delta) \times I_K^B(\beta, \Delta)} \quad (1.5)$$

This method appears to be difficult to apply in our case. Regarding the carbo-nitrides of transition metals, a major problem arises from the presence of niobium, as it is frequently the case in the systems studied in the present work. Close to the carbon and nitrogen K-edges, the niobium element exhibits a so-called “delayed” edge Nb-M<sub>4,5</sub>, starting at around 200 eV and spreading over a wide energy range, which is superimposed with the K edges of carbon and nitrogen (at 286 and 400 eV respectively), and has even a partial recovery with the L-edges of titanium and vanadium (at 455 to and 520 eV respectively). This complicates the measurement of areas associated with each basic chemical element. In addition, another additional difficulty appears if we use the M edge for the Nb quantification: the cross sections of M transitions are difficult to calculate and are generally unreliable. Experimentally it is hardly possible to use the Nb L<sub>2,3</sub> edge, which lies at a very high energy-loss (around 2370 eV), thus having a very unfavorable signal-to-noise ratio.

### 1.3.2 Least Mean Square Fitting

Another known method for analyzing EELS spectra is the Least Mean Square Fitting (LMSF) or adjustment by reference spectra. This method has been used by Craven *et al.* [Craven 00a] to analyze (Ti,Nb)(C,N) particles, and particularly the nitrogen and carbon contents in the precipitates. In their study, they used extraction replicas of carbon with many holes and cracks, then working with precipitates lying partly outside of the replica, which permits to only analyze the carbon from the precipitates and not the amorphous carbon from the film.

In order to treat their spectra obtained on the precipitates, they achieved standard spectra on commercial powders of NbC, NbN and  $\text{TiN}_{0.88}$ . These standards were used to analyze experimental data using a LMSF method, which consists in reconstructing the spectrum as a linear combination of the different standards. Coefficients of the linear combination that weight the standard spectra enable the chemical composition of the precipitate to be determined; they also give directly the atomic composition if standards have already been normalized to the same atomic content (e.g. one atom). Some results are presented in figure 1.5. From these results, Craven *et al.* conclude that the particles analyzed are of core-shell structure with a TiN rich core and a NbC rich shell.

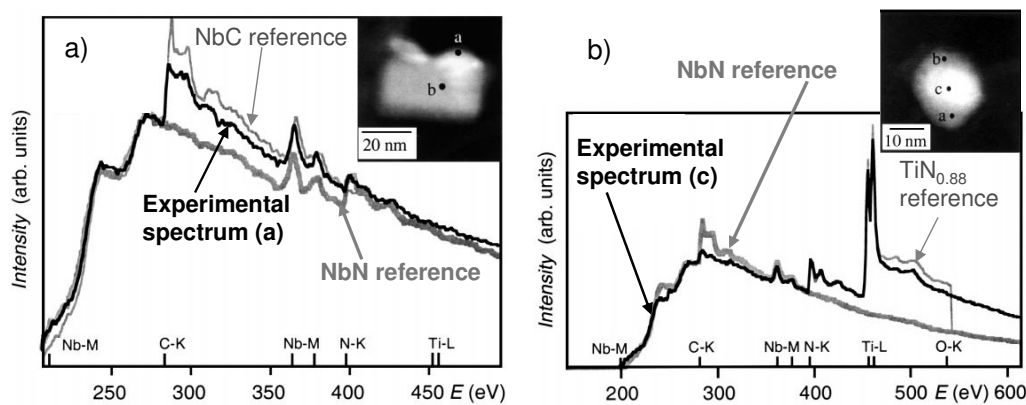


Figure 1.5: Adjustment of experimental spectra with a linear combination of standards NbN, NbC and  $\text{TiN}_{0.88}$ . a) Spectrum of a precipitate shell with no titanium and nitrogen, b) Spectrum of a precipitate core, with nitrogen and titanium. There appears to be an enrichment of Ti and N in the core of particles [Craven *et al.*].

### 1.3.3 Jump Ratio

A third method to determine the composition of carbonitrides by EELS is the “Jump ratio” method used in particular by Courtois *et al.* [Courtois 06]. This technique involves the measurement of the difference between the initial maximum  $H_C$  of C-K ionization edge and the maximum  $H_{\text{Nb}}$  of Nb-M<sub>4,5</sub> ionization edge (see Figure 1.6), this difference being proportional to the atomic ratio C/Nb. A calibration of the “Jump ratio” as a function of the chemical composition C/Nb was established from samples of known composition  $\text{NbC}_x$  (see figure 1.7).

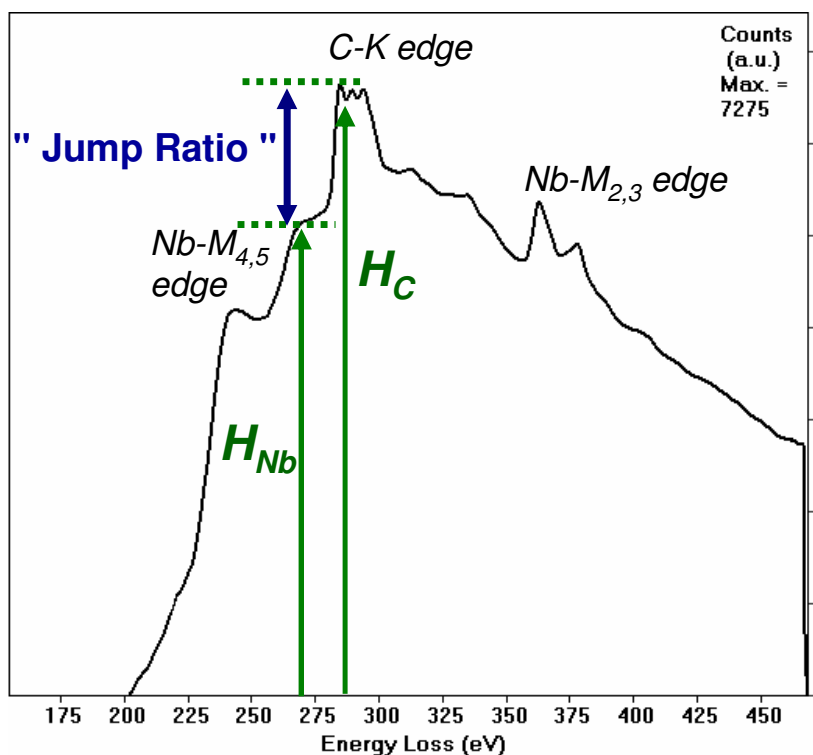


Figure 1.6: Carbon "Jump Ratio" of an EELS spectrum obtained from a bulk Nb<sub>6</sub>C<sub>5</sub> [Courtois 06].

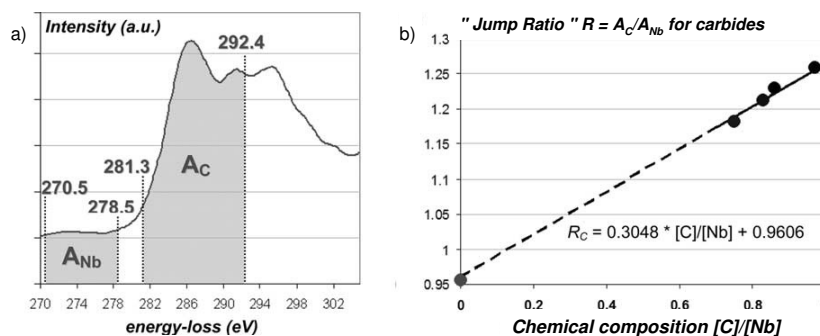


Figure 1.7: Determination of the dependence calibrated curve of "Jump ratio" versus the chemical composition C/Nb. a) Calculation of areas A<sub>Nb</sub> and A<sub>C</sub> to determine the "Jump Ratio"; b) calibration curve of the "Jump ratio" on the carbon K edge citeCourtois06.

The same method was used to determine the atomic ratio N/Nb by measuring the height between the first maximum H<sub>N</sub> of the N-K ionization edge and the maximum H<sub>Nb</sub> of the Nb-M<sub>2,3</sub> ionization edge (see Figure 1.8).

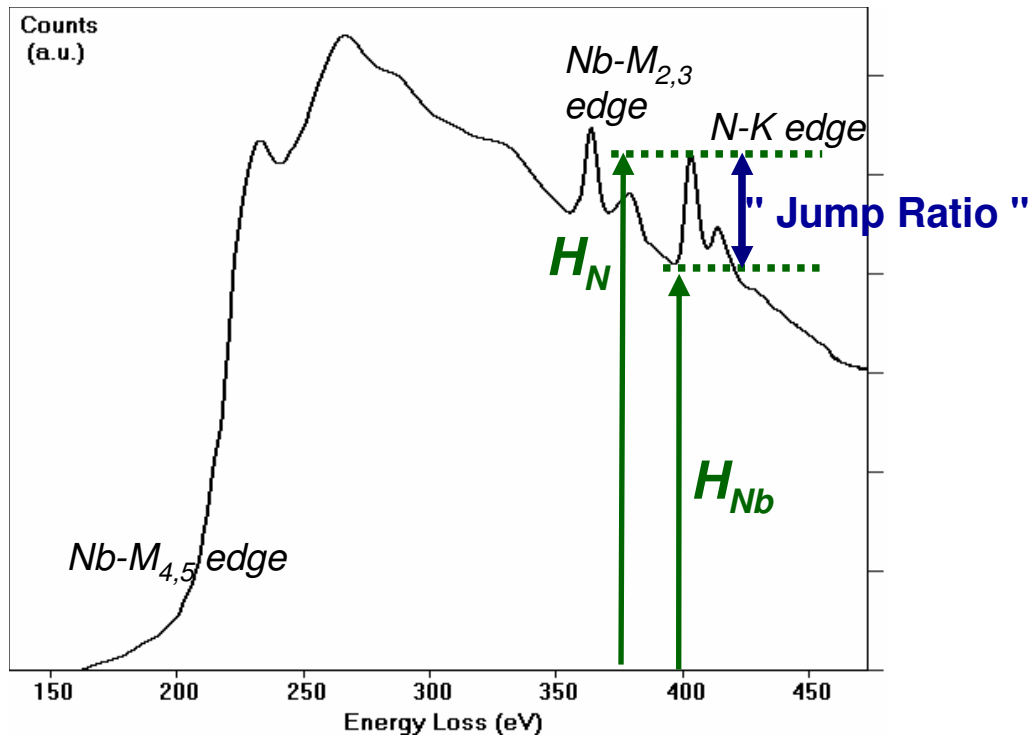


Figure 1.8: Nitrogen "Jump Ratio" of an EELS spectrum obtained from a bulk NbN [Courtois 06].

In the same way as before, Courtois *et al.* determined a calibration line of the "Jump ratio" on the edge K of nitrogen. The equation of that line is given by:

$$\text{"JumpRatio"}_{(N)} = 0.2061 \times \frac{[N]}{[Nb]} + 0.9492 \quad (1.6)$$

This method has given good results in the case of simple carbonitrides such as NbC, NbN or Nb(C,N) but is difficult to implement in the case of complex carbonitrides such as (Nb,V,Ti)(C,N) due to the number "Jump Ratio" to take into account.

### 1.3.4 Second derivative

Finally, there is another method, which consists in achieving a second derivative of the EELS spectrum. This method, used by Scott *et al.* [Scott 02], amplifies any variations within a spectrum, and especially the ionization

edges. Figure 1.9 illustrates this treatment for an EELS spectrum of TiN. We can see, in fact, that the peaks corresponding to the N-K and Ti-L<sub>2,3</sub> edges are exacerbated on the second derivative with respect to the continuous background of the spectrum.

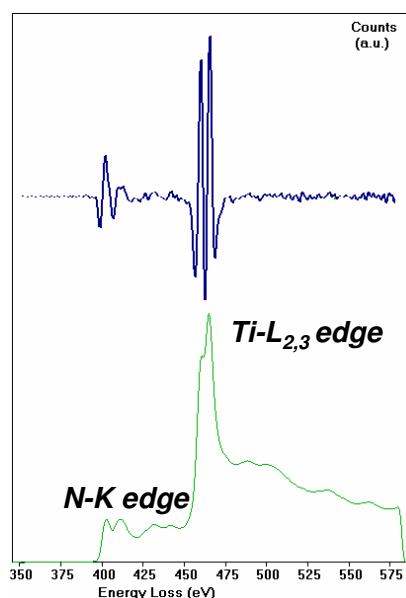


Figure 1.9: *EELS spectrum of a TiN sample and its second derivative. Peaks corresponding to the N-K and Ti-L<sub>2,3</sub> edges are exacerbated by the second derivative (this treatment was performed on an experimental spectrum acquired on a TiN precipitate [Sennour 02]).*

Once the second derivative has been achieved, the peak heights have simply to be compared with the ones obtained from standards previously acquired and processed under the same conditions. This method can be very effective for detecting weak signals but is also prone to errors because of its high sensitivity.

### 1.3.5 Conclusion on methods for quantifying chemical species in EELS

The above paragraphs have shown that there is a number of techniques available to quantify the chemical species from an EELS spectrum. However, several preliminary trials during this work have shown that none of the methods described here did allow us “ex-abrupto” to treat conveniently EELS spectra from complex carbonitrides. It was therefore necessary to develop a method to reliably deal with this kind of spectra, “mixing” the benefits and

flexibility of some of the approaches previously described. First we will briefly present the material used for this study and then we will expose a new method to quantify the chemical species of complex carbonitrides.

## 1.4 Material and treatments

A spring steel previously studied by [Acevedo 07], the 60SiCrV7+Nb grade, has been used to apply our method of chemical species quantification. Its chemical composition is given in table 1.1. This steel is microalloyed with niobium, vanadium and titanium and contains nitrogen in significant quantity.

C	Si	Mn	Cr	V	Nb	Ti	N
0.594	1.621	0.802	0.224	0.152	0.015	0.0025	0.0075

Table 1.1: *Chemical composition of the 60SiCrV7+Nb given in wt%*

After a hot rolling, which can lead to the precipitation of titanium nitrides and niobium carbides, the steel is cooled in air, leading to a fine ferrite-pearlite structure. The state obtained is called “*As Rolled*” state. Moreover, during cooling, precipitation of vanadium and niobium carbonitrides occurs. D. Acevedo highlighted the presence of core-shell type carbonitrides in the *As Rolled* state with a core rich in titanium and a shell rich in vanadium and niobium. However, no EELS analysis have been performed on these particles, therefore he could not concluded on the core and shell composition in carbon and in nitrogen. In order to quantify the carbonitrides chemical composition in light elements, we applied our method to particles obtained on the *As Rolled state*.

## 1.5 Principle of chemical species quantification

The method used to quantify the different elements is based on the “Least Mean Square Fitting” method presented in paragraph 1.3.2. However, in order to optimize the adjustment of the experimental spectra we selected the important areas where the adjustment would be performed, named “fitting windows” (see figure 1.10).

The adjustment of the experimental spectra by a linear combination of reference edges enables, if these reference spectra are properly normalized between them, to estimate the atomic ratio through the coefficients of the linear

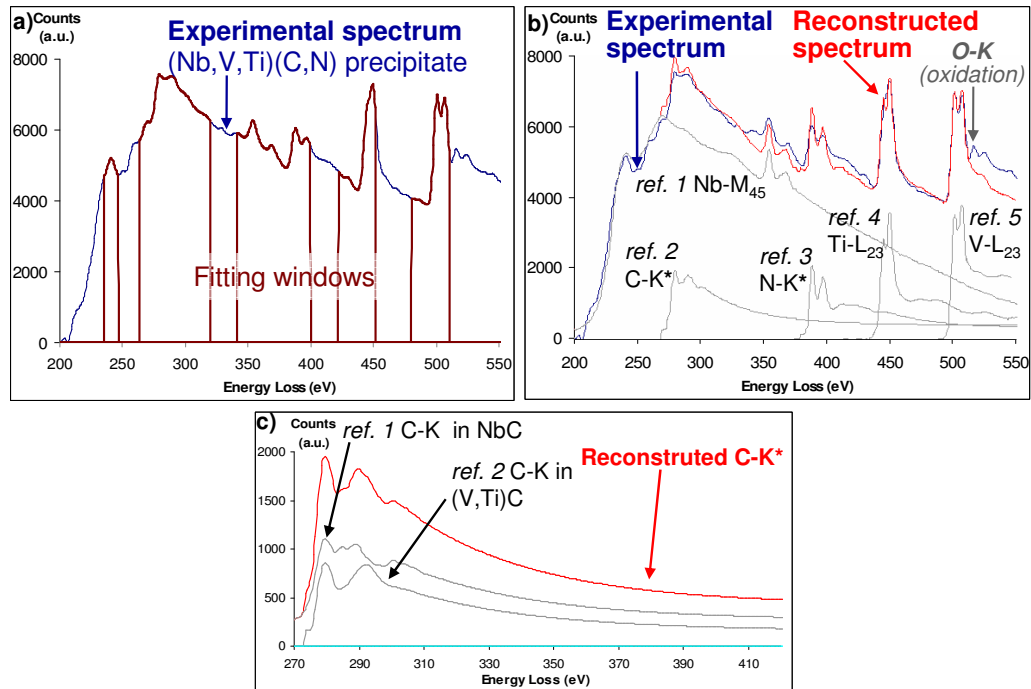


Figure 1.10: Example of a reconstruction of an experimental spectrum from spectra of reference edges. a) Choice of “fitting windows” for the EELS spectrum to adjust; b) superposition of the experimental spectrum and rebuilt spectrum. Spectra of reference edges are plotted on the graph. There is a fairly good superposition of two spectra; c) details of the reconstructed C-K edge. The spectrum is a linear combination of C-K edge in NbC and C-K edge in VC (or TiC). We have done the same for the N-K edge for (linear combination of N-K edges in TiN, NbN and VN).

combination weighting these spectra. So, the first step is to get good references.

In this study we want to apply this technique to the system V-Nb-Ti-C-N. To do this, we need the different edges of these elements. Some edges were obtained from previous work made in the MATEIS group on the same microscope as used here (JEOL 2010F). This is the case for the niobium  $M_{4,5}$  edge and for the carbon K edges in NbC, which come from the work of E. Courtois [Courtois 06] on niobium carbide. Similarly, the titanium L edge and the nitrogen K edge in TiN come from the study of M. Sennour [Sennour 02] on transition metals nitrides in steel. All these edges have been standardized so that their area corresponds to one atom (multiplied by a constant factor). The vanadium  $L_{2,3}$  edge was obtained from the Gatan Atlas [Ahn 83] and normalized (using the Egerton method described in paragraph 1.3.1) to the nitrogen K edge from TiN.

Figures 1.11 and 1.12 show the various ionization edges of the elements studied here. Figure 1.12 shows an additional difficulty for non-metallic light elements, because of ELNES features (Energy-Loss Near-Edge Structures): owing to the sensitivity of EELS to the chemical bond, the C-K and N-K edges are not strictly similar whether they are bonded to niobium, vanadium or titanium. Specifically, we note that the two K-edges of carbon and nitrogen are very similar in appearance in titanium and vanadium carbides (nitrides), which corresponds to the fact that Ti and V elements are very close in the periodic table. This obviously depends on the resolution, at which spectra are acquired. Work done with a VG microscope [Scott 01] with a much better energy resolution than our 2010F (0.5 eV compared to 1-1.2 eV) shows that it is possible to differentiate these spectra in the case of VC and TiC carbides (see figure 1.12.c). A convolution of these edges by a gaussian function describing our poorer energy resolution around (1.1±0.1) eV “erase” these differences, and so we can properly consider these 2 C-K<sub>TiC</sub> and C-K<sub>VC</sub> edges as identical (and N-K<sub>TiN</sub> and N-K<sub>VN</sub> edges reciprocally). For each light elements, we therefore consider:

- for nitrogen N-K: 2 references N-K<sub>(Ti,V)N</sub> and N-K<sub>NbN</sub>
- for carbon C-K: 2 references C-K<sub>(Ti,V)C</sub> and C-K<sub>NbC</sub>, to which we add a reference related to the possible presence of residual carbon contamination, that is of amorphous-type (C-K<sub>Cam</sub>)

These choices will lead us to a slightly better description of spectra at the edge of light elements, but they cannot treat properly any deviation from the sub-stoichiometry in detail: if there is, for example a global sub-stoichiometry in carbon (or in nitrogen), it is strictly impossible to attribute the sub-stoichiometry at Ti or V bond, which are described by the same C-K<sub>(Ti,V)C</sub> edge (similarly, N-K<sub>(Ti,V)N</sub>). Moreover, even if references related to Nb on the one hand, and the V/Ti on the other hand are different, various preliminary tests have shown that it is not possible to assign accurately the sub-stoichiometry to the Nb or V/Ti bond.

A routine was then written to fit the experimental spectrum with standard edges. This program first allows to match all energy dispersions (according to the fact that experimental spectra may have been recorded with a different energy dispersion compared to that of the references). Preliminary tests with the original LMSF method showed that it was difficult to get good results over a wide energy range (i.e. about 180 to 530 eV). This is essentially because the subtraction of the continuous background (by a power law) is known to be not very reliable for energy ranges typically larger than 100 or 200 eV. To correct the inaccuracy of this subtraction, we allowed an additional local treatment of

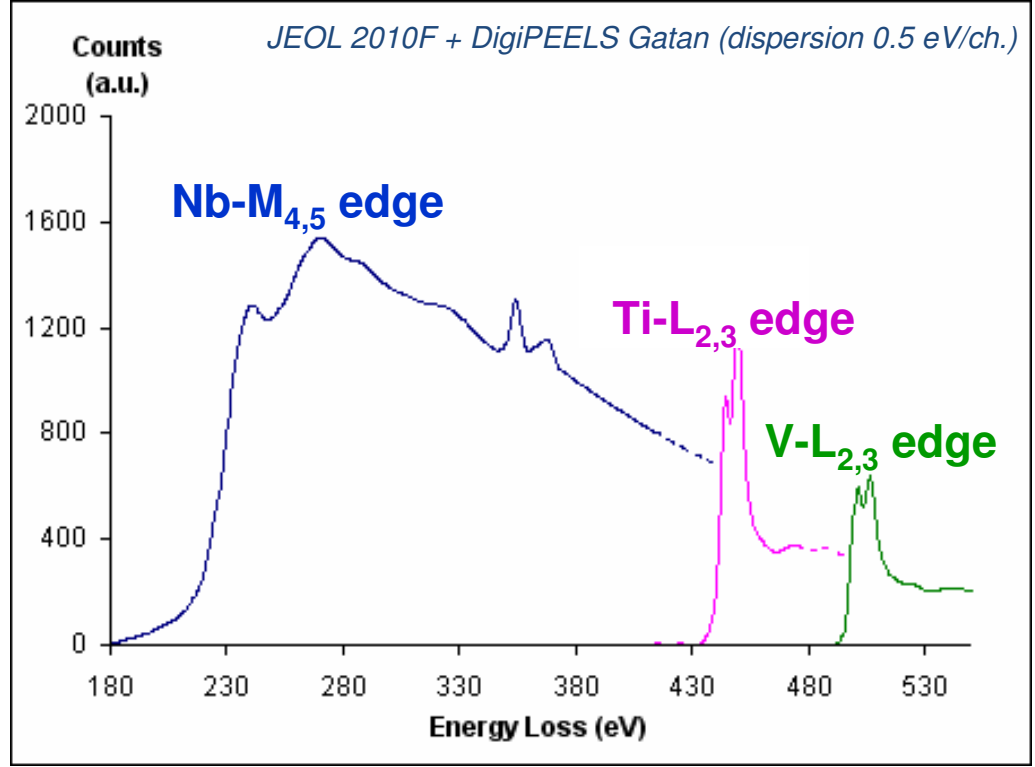


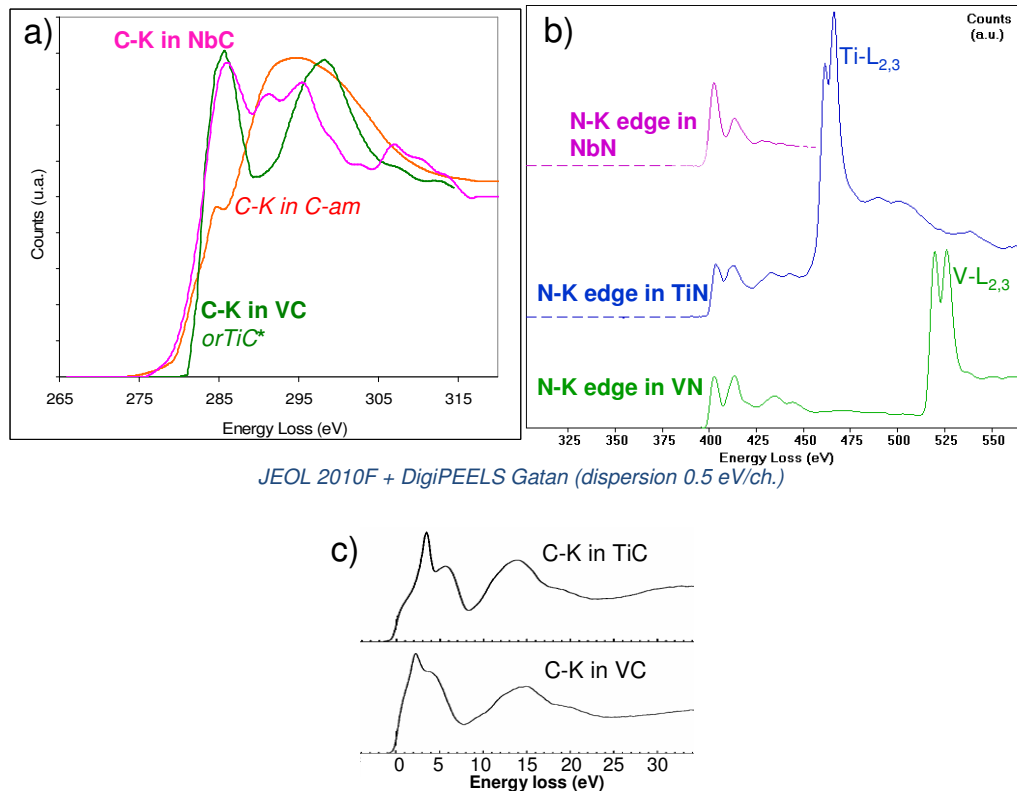
Figure 1.11: Ionization edges of the elements Nb, V and Ti. Each spectrum is normalized to one atom.

the background through the use of further exponential laws attached to each reference spectrum. This can be analytically expressed as:

$$N(E) = \sum \left[ C^i \left( R^i(E) + C_{Bg}^i \exp[-\alpha_{Bg}^i \ln(E - E_o^i)] \right) \right] \quad (1.7)$$

where  $N(E)$  is the number of counts for the final spectrum at the energy loss  $E$ ,  $R^i(E)$  the number of counts for the reference spectrum for the element  $i$ ,  $C^i$  the coefficient of the linear combination for that element  $i$ ,  $C_{Bg}^i$  and  $\alpha_{Bg}^i$  coefficients of the exponential law for the local background treatment near the edge  $i$  and starting at  $E_o^i$  (the onset energy of the edge for the element  $i$ ; This correction is ignored if  $E$  is less than  $E_o^i$ ). The matching procedure is performed with the Excel solver, and values of the different coefficients are obtained using the Newton-Raphson method.

By using this method we were able to improve the “reconstruction” of experimental spectra. However, to facilitate the calculation done by the Excel solver we proceeded in several stages:



JEOL 2010F + DigiPEELS Gatan (dispersion 0.5 eV/ch.)

Figure 1.12: Ionization edge of non-metallic elements. a) C-K edge in NbC, VC (or TiC) and C-amorphous. b) N-K edge in NbN, VN and TiN. c) C-K edge in VC and TiC [Scott 01]. We note that both edges are quite similar, which is why we had not differentiated.

- step 1: search of  $C^i$  coefficients of the linear combination; the coefficients of the exponential laws are set to zero.
- step 2: search of  $C_{Bg}^i$  and  $\alpha_{Bg}^i$  coefficients of the exponential laws; values of  $C^i$  are set to previous values.
- step 3: iterative improvement of  $C^i$  with the new coefficients.

A constraint has finally been added with regard to nitrogen and carbon. In the case where the metallic element M (M = Nb, V or Ti) is not present in the experimental spectrum, the contribution of N-K and C-K levels in MC and MN is forced to zero.

## 1.6 Results and discussion

### 1.6.1 Verification of the references

The first step in the treatment of experimental spectra has been to check our references on spectra from carbonitrides of which we knew the chemical composition. We can see on figure 1.13 that the combination of reference spectra edges are very well superimposed with the experimental spectra. In addition, the table at the bottom of the figure shows that the values obtained by the solver are consistent with expected values.

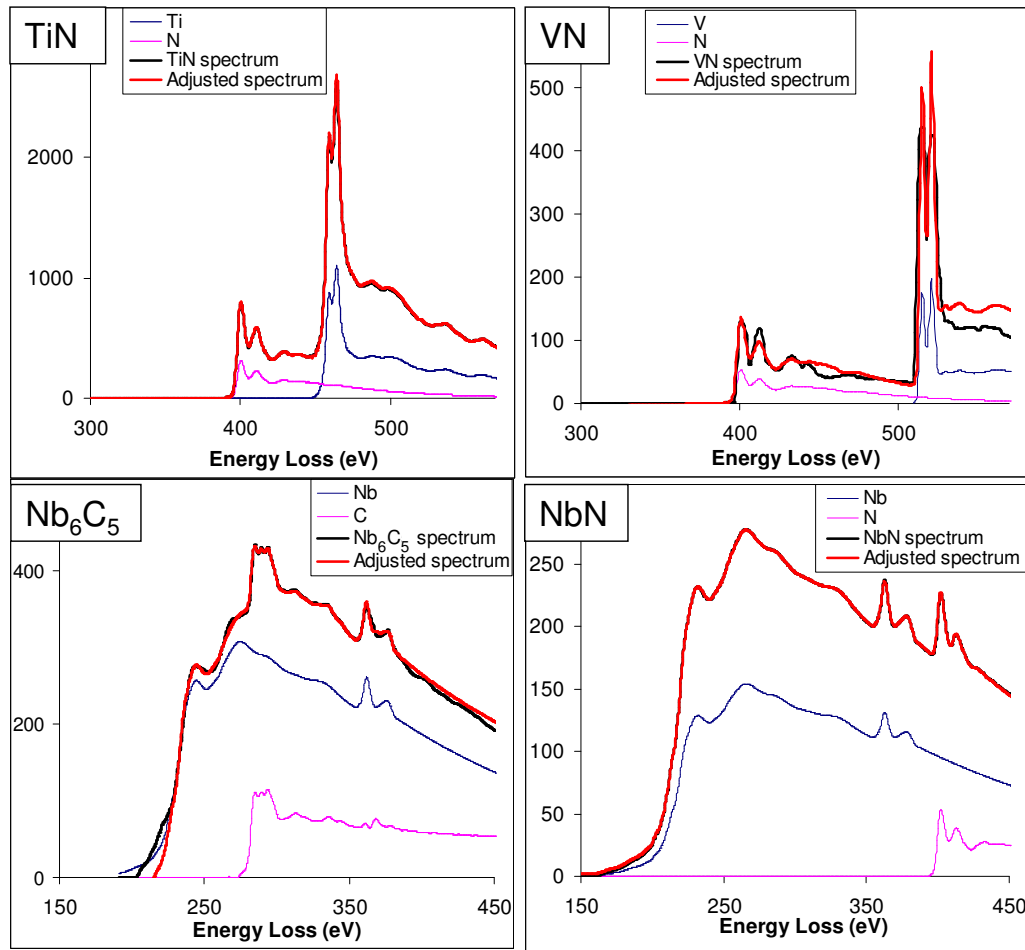
### 1.6.2 Experimental spectra treatment

Once the reference spectra edges analyzed, we can use the method to treat experimental EELS spectra from carbonitride precipitates. To prevent the carbon contamination all EELS analysis were performed at the liquid nitrogen temperature. As a first step we will compare, for metallic elements, the values obtained by this new technique with the values obtained by EDX. Then we will validate this method on precipitates observed in the work of D. Acevedo [Acevedo 07].

#### 1.6.2.1 Results and comparison with EDX

Chemical compositions of precipitates from the 60SiCrV7+Nb industrial steel at the *As Rolled* state, obtained by the LMSF method with “fitting windows” were compared with those obtained by EDX for the carbonitrides metallic elements Nb, V and Ti. Figure 1.14 presents the case of a carbonitride with fairly balanced quantities of niobium, vanadium and titanium. The table on the figure shows that for the metallic elements, the values obtained by the EELS method are in agreement with those obtained from the EDX.

We have verified for each treated spectrum that the concentrations obtained for the metallic elements correspond to the values given by the EDX analysis (Figure 1.15). For a given precipitate, the results of EELS (“filled circles” symbols) and EDX (“empty squares” symbols) partners are connected by a segment, in order to have a better appreciation of the dispersion: there is indeed a correct agreement for most of the spectra, and we can appreciate the correspondence of the 2 methods, with an accuracy of about 5 at.%. Thus, the method we have developed gives good results for metallic elements, giving thus credit to quantifications that we can deduce from EELS for light elements such as nitrogen and carbon. In fact, the good “EDX/EELS” agreement proves that the normalization of EELS reference spectra is correct. We therefore



	EELS	Expected
<b>N/Ti</b>	1.168	1
<b>N/V</b>	0.938	1
<b>N/Nb</b>	0.990	1
<b>C/Nb</b>	0.814	0.8333

Figure 1.13: Reconstruction of spectra from carbonitrides with known chemical composition in order to verify our spectra of reference edges. The  $Nb_6C_5$  and NbN spectra come from the work of [Courtois 06], the TiN spectrum comes from the work of [Sennour 02] and the VN spectrum comes from [MacKenzie 06] (as an exercise, we have reconstructed an experimental spectrum of stoichiometric VN different from that used to extract the  $V-L_{2,3}$  edge - that is the Gatan spectrum). There is a good agreement between the values obtained by the EELS method and those expected.

use EELS for examining the quantities of non-metallic elements present in

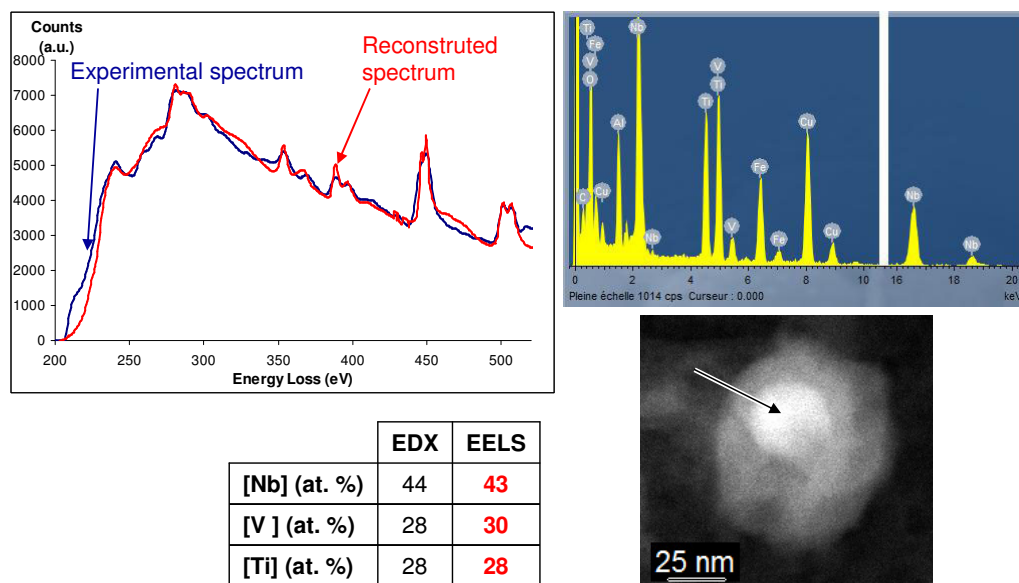


Figure 1.14: Experimental EELS spectrum of a carbonitride (Nb,V,Ti)(C,N) from the As Rolled state of the 60SiCrV7+Nb steel. The reconstructed spectrum shows a good fit. The spectrum obtained by EDX allows us to view the metallic elements but it is impossible to quantify the nitrogen and carbon. The table shows the results of the EDX and EELS analysis for metallic elements. We note that both methods give very close values.

carbonitrides, which cannot be done with EDX. The x-axis on figure 1.16 shows the percentage of nitrogen compared to the non-metallic elements and the y-axis shows the ratio (C + N)/Metals. Thus, we see a quasi-systematic sub-stoichiometry in most of the analyzed carbonitrides. A sub-stoichiometry in carbides or carbonitrides was observed several times, notably in the work of D. Acevedo [Acevedo 07] on  $V_6C_5$  carbides, which the composition have been determined using diffraction patterns, or in that of E. Courtois [Courtois 05] on  $NbC_xN_y$  carbonitrides and using the “Jump Ratio” method to quantify the chemistry.

#### 1.6.2.2 Application to the analysis of precipitate type core-shell

Having a method to reliably and quantitatively analyze the various constituent species of carbo-nitride precipitates, it appears interesting to come back on a point raised in the earlier work of D. Acevedo [Acevedo 07] and concerning the heterogeneities in composition of particles with a core-shell structure. In a vanadium, titanium and niobium microalloyed steel (60SiCrV7+Nb alloy), the existence of core-shell precipitates was revealed, with a core apparently

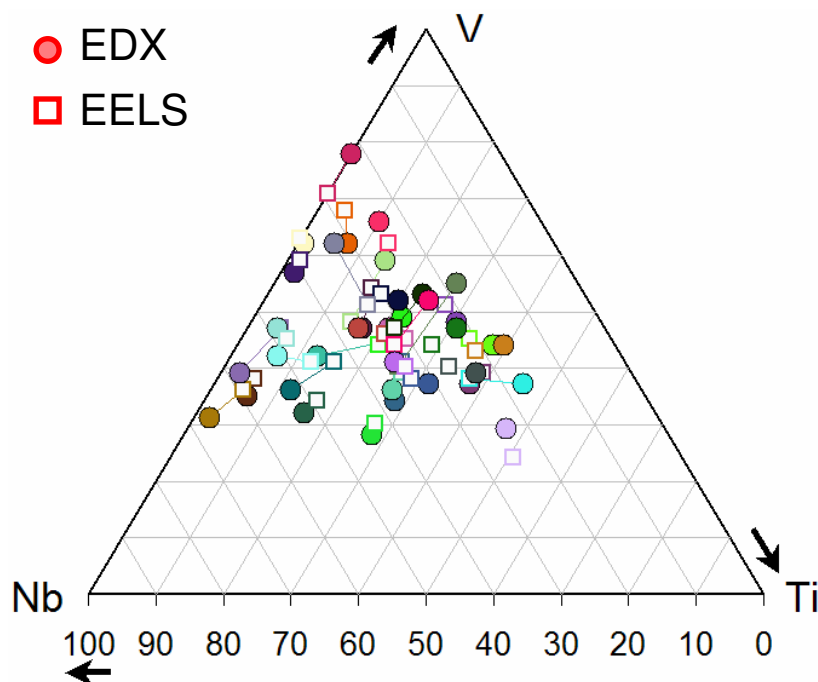


Figure 1.15: Graphical representation of results obtained by EDX and EELS analysis for all treated spectra of the 60SiCrV7+Nb steel at the As Rolled state. The ternary diagram allows to view the quantities of metallic elements in the carbonitrides. Each colour represents a test. Results show that values obtained by EDX are very close to those obtained by EELS (each square is associated with the disk of same colour).

rather rich in TiN and a (Nb,V)(C,N) shell-rich. This hypothesis was simply deduced from EDX measurements and could not be confirmed by the direct EELS analysis of light elements, due to the use of carbon extraction replicas. It therefore seemed useful to repeat this issue with new observations and analysis to provide some more detailed information on the concentrations of nitrogen and carbon, and hopefully to treat separately the cores and the shells. It is further noted that these observations of core-shell structures are in agreement with several previous studies, including Craven *et al.* [Craven ooa] (see paragraph ??) or Fu *et al.* [Fu 07], who characterized the precipitation state in a 2.25Cr-1Mo-0.25V steel microalloyed with niobium, vanadium and titanium. They highlight the presence of complex precipitates type core-shell with a core enriched in TiN and a shell composed of (V,Nb)(C,N).

During our observations we have found many precipitates with a heterogeneous composition: core-shell type. The results obtained with a nano-probe of typically 2 nm are plotted on figures 1.17 and 1.18.

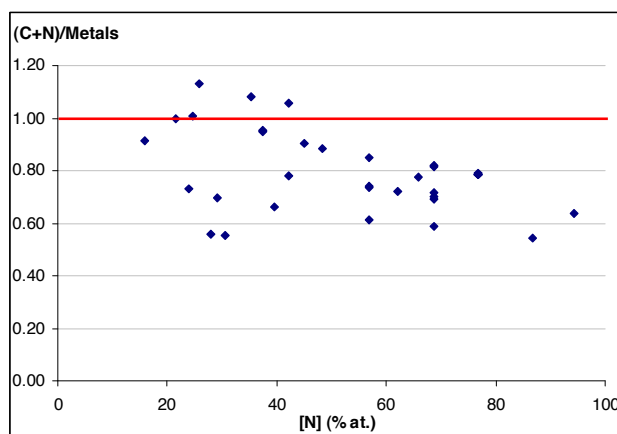


Figure 1.16: Results obtained by EELS for the quantification of carbon and nitrogen. The graph shows the percentage of nitrogen in precipitates and the stoichiometry particles. We can see that most of the precipitates are sub-stoichiometric (the stoichiometry is represented by the red line).

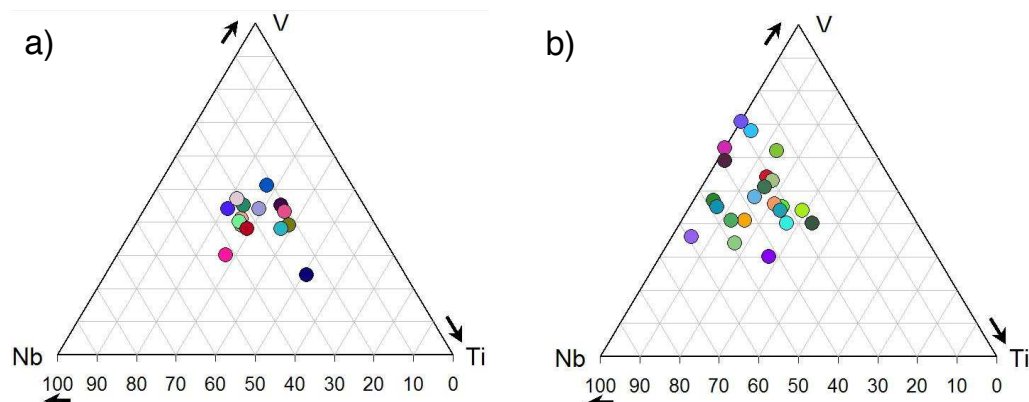


Figure 1.17: Graphical representation of results obtained by EELS for all treated spectra. a) Analysis performed in the core of precipitates and b) in the shell. There is a clear titanium enrichment in cores of precipitates.

Figure 1.17 shows that there is an enrichment in titanium for the cores of precipitates (see figure 1.17.a) while the shell (figure 1.17.b) are rather rich in vanadium and niobium. In addition, figure 1.18 shows a clear enrichment in nitrogen in core of precipitates (see figure 1.18.b). Figure 1.18.c presents a correlation of previous data, which shows a “TiN” enrichment in the core. It should be noted that all tests conducted in the core of precipitates cannot get an exact composition. Indeed, it is systematically related to the contribution of

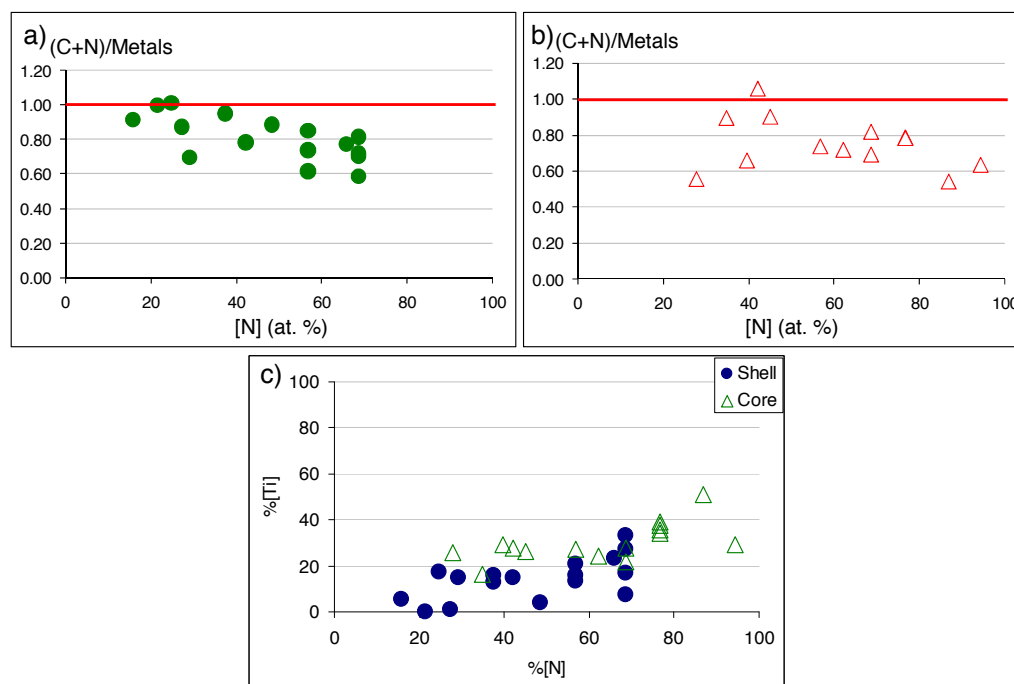


Figure 1.18: Results obtained by EELS for the quantification of carbon and nitrogen in the shells and cores of precipitates (x-axis: percentage of nitrogen in precipitation, y-axis: ratio of non-metallic to metallic elements). a) Analysis carried out in the shells; b) Analysis carried out in the cores. We see an enrichment of nitrogen in the cores of carbonitrides; c) Correlation of the previous data for the non-metallic elements with the Ti contents, showing a similar “TiN” enrichment in the core.

the precipitate shell over and below the central area (effect of superposition in projection), which may explain, particularly for nitrogen, that the enrichment cannot always be easily evidenced (see figure 1.18).

Some tests have been performed on core-shell precipitates in order to model the precipitate volume and obtain the correct core composition. We supposed that precipitates are spherical and the core is situated at the sphere center. Furthermore, we assumed that all core measurement are exactly performed in the center of the core. Then, the analysis obtained at the center of the particle contains two contributions: one due to the surrounding shell, which can be deduced from the analysis of the shell periphery, and one due to the core, which can then be obtained by difference. Figure 1.19 presents an example of this treatment. We can see that there is effectively an enrichment in nitrogen in the core. To obtain better results we need to model more precisely the precipitate shape and note the exact probe position during the analysis.

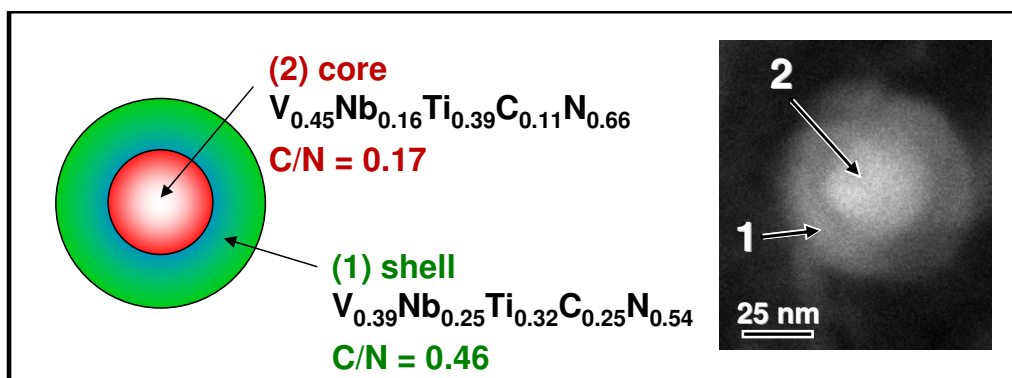


Figure 1.19: Precipitate chemical composition obtained in the core and in the shell of the precipitate after a modelling of its shape. We effectively observe an nitrogen enrichment in the core. The apparently high Ti contents of the shell is probably linked to the non-ideal shape of the particle and uncertainty of the probe position.

## 1.7 Conclusion of the chapter

To quantify light elements such as nitrogen and carbon, we have developed a methodology for the treatment of EELS spectra. The results for metallic elements Nb, V and Ti were compared with those obtained by EDX analysis and present a very good agreement. Thus, we are quite confident in the measures derived from the EELS for carbon and nitrogen.

We observed a quasi-systematic sub-stoichiometry in the analysis of precipitates. Such sub-stoichiometry has been observed previously, particularly in the study of D. Acevedo on a model alloy FeCV [Epicier 07], which highlighted in a formal way the precipitation of the sub-stoichiometric phase  $V_6C_5$ , or during the thesis work of E. Courtois [Courtois 05] on systems Fe-Nb-C-N, and also in the work of Craven et al. [Craven 00a] on (Ti,Nb)(C,N) particles.

In our study, we also observed type core-shell precipitation. The EELS analysis has been demonstrated that there was an enrichment of titanium and nitrogen in the precipitate cores while the shells are rather rich in (V,Nb)(C,N). However, the results for precipitate core can not give the exact composition because of a systematic contribution due to the surrounding shell. We showed that with a geometrical model we can approach the exact core composition. However, many parameters must be taken into account in this kind of model, such as the real precipitate shape, the precise location of the analysis, etc... (see figure 1.19). This would then certainly be interesting to refined this geometrical approach and perform more accurate measurements

on these complex precipitates.

Finally, there is an interest to know the carbon and nitrogen composition in order to model the precipitation kinetics of  $M(C,N)$  or  $(M,M')(C,N)$  carbonitrides during austenitizations.

## CHAPTER 2

# Role of nitrogen in the dissolution of complex (V,Nb)(C,N) precipitates

Microalloying elements (such as vanadium, niobium, titanium,...) are commonly used in industrial steels in order to improve their mechanical properties. During thermo-mechanical treatments performed on these steels, the microalloying elements form precipitates such as carbides, nitrides or carbonitrides. These precipitates can in particular restrict the Prior Austenitic Grain Growth (PAGG) at high temperatures due to their low solubility in austenite and their ability to pin grain boundaries [Gladman 92], [Ooi 06], [Maruyama 98], [Fernandez 07], [Vega 06]. They can also induce structural hardening with a fine precipitation in the ferrite [Caifu 00], [Klinkenberg 04], [Baker 09].

Very few studies are devoted to the fine characterization of the evolution of the precipitation state in steels containing several microalloying elements. In the case of vanadium and niobium microalloyed steels containing nitrogen, most of these studies assume that precipitates are mixed (V,Nb)(C,N) [Crooks 81], [Speer 87]. Very few works assume the existence of two precipitate types, such as one rich in vanadium and the other one rich in niobium in this case. In his PhD D. Acevedo characterized the evolution of binary  $V_6C_5$  and NbC during reversion on a FeVNbC model alloy [Acevedo 07]. Furthermore, many papers do not conclude on the exact composition of the vanadium or niobium rich precipitates [Kuziak 95], [Källqvist 00], [Hald 03]. In order to characterize the precipitation state it is important to perform many thermo-mechanical treatments, sometimes delicate or impossible to be implemented. Thus, we need models, validated on experimental results, to simulate these treatments.

Our study follows the PhD of D. Acevedo [Acevedo 07] on the evolution of precipitate state during austenite treatments on vanadium and niobium

microalloyed steel. During this previous work, a first FeCV model alloy was elaborated to obtain experimental data on the precipitation state evolution, in order to validate a model of precipitation kinetics. Then, niobium was added in a FeVNbC model alloy to study and model the evolution of precipitates in steels containing more than one microalloying elements. Finally, an industrial steel microalloyed with vanadium, titanium, niobium and nitrogen was studied, the 60SiCrV7+Nb spring steel. Its study shown the presence of core-shell precipitates structure. Moreover, predictions of the software PreciSo developed by D. Acevedo was not in total agreement with the precipitation state evolution of the 60SiCrV7+Nb steel. Indeed, the model does not take into account the nitrogen, which is present in the industrial steel.

To understand the influence of nitrogen on precipitation state, a FeVNbCN model alloy has been elaborated. After briefly recalling results of the study on the 60SiCrV7+Nb microalloyed steel, we will present the FeVNbCN model alloy (chemical composition, heat treatment). Then we will give results obtained for the precipitation state (volume fraction, precipitate size distribution and precipitate chemical composition) and will compare the two alloys. In particular, we will presents EELS analysis, which allows us to quantify the carbon and nitrogen contents in precipitates. Finally, results of the FeVNbCN will be compared with prediction of a model based on the software PreciSo, and which take into account the nitrogen. This new model is an help to understand the precipitation state evolution during austenitizing treatments.

## 2.1 Materials and heat treatment

### 2.1.1 The 60SiCrV7+Nb industrial steel

In this section we recall thermal treatments performed on the 60SiCrV7+Nb industrial alloy studied by D. Acevedo [Acevedo 07] during his PhD.

The chemical composition of this steel is based on the French standard NF EN 10089 and is given in table 2.1.

C	Si	Mn	Cr	V	Nb	Ti	N
0.594	1.621	0.802	0.224	0.152	0.015	0.0025	0.00075

Table 2.1: *Chemical composition of the 60SiCrV7+Nb industrial steel given in wt%.*

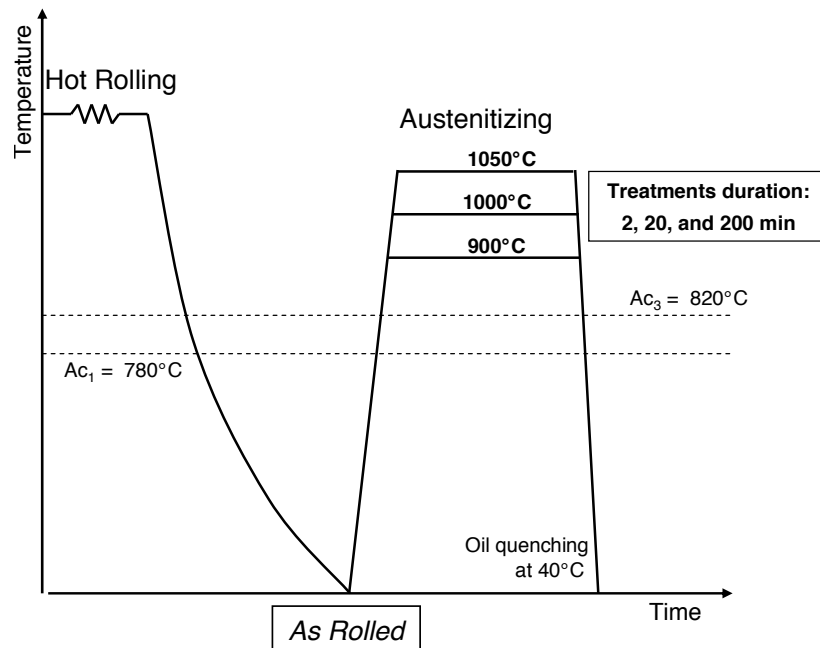


Figure 2.1: Heat treatments performed on the 60SiCrV7+Nb microalloyed steel.

During previous investigation [Acevedo 07], different heat treatments performed on the industrial steel, which are presented on figure 2.1. The hot rolling performed at Ascometal, leading to a 15 mm diameter bar, is followed by a slow cooling to obtain the “As Rolled” state. Then several austenitizing treatments of 2 to 200 minutes at temperature within 900°C and 1050°C are performed on this state. These treatments are followed by an oil quenching at 40°C. All austenitizing treatments were performed under vacuum in quartz capsules.

### 2.1.2 Elaboration and heat treatments of FeVNbCN microalloyed steel

To understand the influence of nitrogen in the evolution of precipitation state a microalloyed steel with vanadium, niobium and nitrogen has been elaborated. In this section, we present the elaboration and chemical composition of this alloy, and the heat treatments performed on the investigated steel.

### 2.1.2.1 Elaboration and chemical composition of the model alloy

The model alloy FeVNbCN was synthesized at the research center CREAS of Ascometal. The cast is performed in a smelting furnace ALD VIM. It starts with the melting at 1500°C of raw materials (ARMCO Iron, iron-nitride, vanadium, niobium and carbon). A first analysis is performed in order to verify the alloy composition. Then it undergoes different heat treatments detailed in the next paragraph.

Despite the care taken in its elaboration, this alloy presents many impurities in its composition (see table 2.2). They may come from the crucible used to make the cast, or from the ARMCO Iron, which is not totally pure. The chemical composition of the FeVNbCN alloy is based on that of two steels studied by D. Acevedo: the industrial microalloyed steel 60SiCrV7+Nb for niobium and nitrogen and the model alloy FeCV for vanadium and carbon to obtain the composition Fe-0.2wt%-V-0.015wt%Nb-0.5wt%C-0.008wt%N.

	<b>C</b>	<b>Si</b>	<b>Mn</b>	<b>S</b>	<b>Ni</b>	<b>Cr</b>
wt. %	<b>0.48</b>	0.028	0.088	0.017	0.023	0.049
at. %	<b>2.2</b>	0.055	0.088	0.029	0.021	0.052
	<b>Mo</b>	<b>Ti</b>	<b>Nb</b>	<b>V</b>	<b>N</b>	
wt. %	0.007	0.001	<b>0.012</b>	<b>0.202</b>	<b>0.0063</b>	
at. %	0.004	0.0011	<b>0.0071</b>	<b>0.217</b>	<b>0.025</b>	

Table 2.2: Chemical composition of the FeVNbCN steel (in wt.% and at.%)

### 2.1.2.2 Heat Treatments

The thermal cycle undergone by the model alloy FeVNbCN is presented in figure 2.2. This cycle can be decomposed in three parts: solutionizing treatment realized in the research center CREAS, treatment for “fully-precipitated” state and reversion treatments. These two last treatments are performed at MATEIS.

#### **Solutionizing treatment:**

At first a solutionizing treatment was performed at 1280°C during 30 minutes under argon followed by a water quench. It was carried out on disk 8 mm thick to avoid the formation of “Troostite” (fine lamellar structure of pearlite) at prior austenite grain boundaries. Optical micrographies confirmed the absence of this structure. After this treatment, the disk is cut in small sample

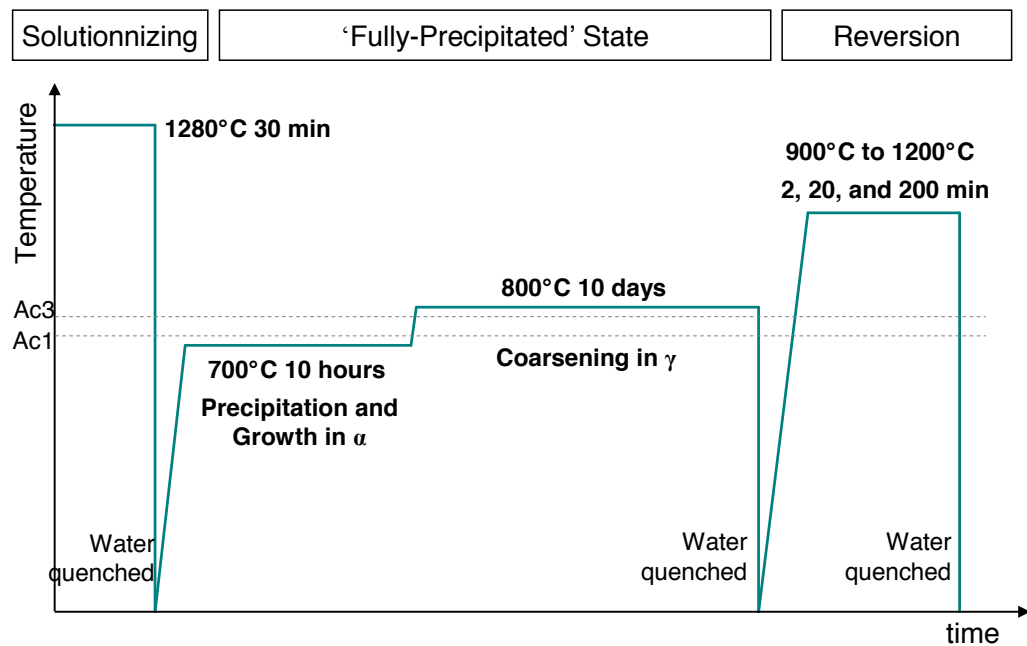


Figure 2.2: *Thermal cycle performed on the model alloy FeVNbCN.*

(see figure 2.3 for the sample preparation)

#### “Fully-precipitated” state treatment:

The treatment following the solutionizing is called “Fully-precipitated” state treatment (more details are given in [Epicier 07]). It aims at achieving an advanced precipitation state with relatively large precipitates. This treatment is divided into three steps:

- 700°C during 10 hours to nucleate and grow in ferrite and thus obtain a large precipitate volume fraction.
- 800°C during 10 days in order to allow the coalescence of precipitates in austenite.
- quick cooling by water quenching.

The state obtained will be the starting point of all reversion treatments.

### Isothermal reversion treatments:

Several reversion treatments (or austenitizing treatments) were realized to observe the evolution of precipitation state and austenitic grain size over time.

In order to compare results obtained from both the 60SiCrV7+Nb industrial steel and the FeVNbCN model alloy, temperatures have been chosen between 900°C and 1200°C for treatment times between 2 and 2000 minutes. Samples are then water quenching for a rapid cooling.

Reversion and “Fully-precipitated” state treatments have been realized on small samples in quartz capsules under vacuum to avoid decarburizing. The sample preparation is illustrated in figure 2.3. Sections of as received material are cut to obtain samples of 5 mm × 5 mm × 30 mm, taking care to remove segregated areas (sections center) or decarburized areas (sections surface). It has been checked that no decarburization occurs in the bulk of the sample (from 1 mm to the surface).

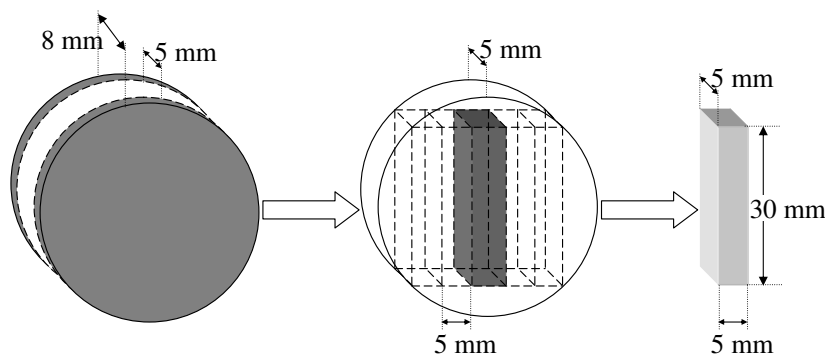


Figure 2.3: Samples preparation for the FeVNbCN alloy. Grey parts are removed to avoid decarburized and segregated areas.

## 2.2 Experimental techniques

### 2.2.1 Transmission Electron Microscopy

To study accurately the evolution of the precipitation state during various heat treatments, we used Transmission Electron Microscopy (TEM) and related techniques. This allowed us to determine the size but also the chemistry of particles with radii of the order of tens of nanometers. Indeed, although Scanning Electron Microscopy (SEM) allows to observe these precipitates (and thus obtain size distributions as demonstrated by D. Acevedo [Acevedo 07]),

it does not give the chemical composition of these small particles, especially regarding the carbon and nitrogen contents. Therefore, TEM was preferably used.

### 2.2.1.1 Microscope characteristics

The study of precipitation states was done using a transmission electron microscope working at 200 KeV: the JEOL 2010F, and whose characteristics are reported in table 2.3. This microscope has, in particular, equipments to do imaging in High Angle Annular Dark Field (HAADF) and Electron Energy Loss Spectroscopy (EELS). It is a high resolution, analytic microscope equipped with a Schottky field emission gun, which allows to have a high brightness ( $10^4$  times greater than for a tungsten filament) and excellent spatial and temporal coherence, leading to an information limit of 0.12 nm or slightly better.

	JEOL 2010F
Tension	200 kV
Emission mode	Field emission (Schottky)
Point resolution (nm)	0.194
Information limit	0.12
Probe minimal size (nm)	~0.4 - 0.2
$C_s$ (mm)	0.5
$C_c$ (mm)	1
Object slides	Simple tilt $\pm 20^\circ$ Double tilt ( $\pm 20^\circ - \pm 20^\circ$ ) Cold (Temperature $\sim -180^\circ\text{C}$ )
Analysis accessories	EDX Oxford (Ultrathin window UTW) Digi-PEELS Gatan

Table 2.3: JEOL 2010F microscope characteristics.

### 2.2.1.2 Imaging modes

#### Conventional Transmission Electron Microscopy

There are several imaging modes. First of all conventional imaging, which consists in selecting a dedicated electron beam after the sample with an objective (or contrast) aperture. Conventional Transmission Electron Microscopy (CTEM) is carried out typically in Bright Field (BF) and Dark Field (DF)

imaging modes. To achieve a Bright Field, the transmitted beam is selected with a contrast aperture, while for a Dark Field a diffracted beam is selected. Since the 1950's many works use the CTEM to study the precipitation in steels, and characterize particles in thin foils of extracted replicas. Such approaches are still relevant, for example we can cite some recent studies: the precipitation of chromium, vanadium and niobium carbonitrides in steel containing chromium [Onizawa 06], and the study of the precipitation in microalloyed steels with niobium [Courtois 05]. In thin foils, CTEM can view the exact location of precipitates and study the possible orientation relationships between them and the matrix. Indeed, CTEM is relatively easy to undertake in such a case, because all precipitates sharing the same orientation relationship with the iron phase can be imaged simultaneously in DF, once the grain is viewed along an adequate zone axis. However, this situation is not encountered in the present study, and further arguments will be developed in the next sub-section to justify the use of another imaging mode.

### HAADF in STEM

When working in the austenitic domain, precipitates lose their orientation relationship with the matrix and are therefore more difficult to study as reported above, when orientation relationships exist, it is easy to observe simultaneously the matrix on "zone axis" (i.e. in specific crystallographic directions), and the precipitates. This allows, on one hand to bring these precipitates in diffraction contrast, and on the other hand to identify the sections of the reciprocal lattice through the associated diffraction spots. In the absence of orientation relations, precipitates can be difficult to find and zone axis are usually hazardous to find because of their small size and the magnetism of the ferritic matrix. In this case, another imaging technique can be used to characterize the precipitation: the High Angle Annular Dark Field (HAADF) associated with the Scanning Transmission Electron Microscopy mode (STEM). This technique enables to collect electrons scattered incoherently at angles well above the Bragg angle through a suitable annular detector. For one atomic species, the scattered intensity  $I$  is theoretically proportional to the square of the atomic form factor  $F(q)$ :

$$F(q) = \frac{Z}{2\pi^2 a_0 q^2} \quad (2.1)$$

With  $q = 2 \sin \theta / \lambda$ ,  $a_0 = \epsilon_0 h^2 / (\pi m_0 e^2)$  the Bohr's radii, and  $Z$  the atomic number. Thus, the scattered intensity is proportional to the square of atomic number  $Z^2$ , which allows, in principle, images with a chemical contrast to be obtained. The HAADF detector is coupled with a scanning device of the incident beam (STEM module), which enables to perform a regular scan of the

sample and, is thus, a particularly powerful tool to observe phases with a high chemical contrast. We have used this technique in our study of precipitates, i.e. transition metals carbonitrides, collected on carbon or aluminium replicas. The method of preparation of these replicas is described in appendix A. This approach has in fact a threefold advantage over imaging in thin foil: (i) extraction of precipitates on replicas allows to override the magnetism of the matrix, which makes the observations very tedious; (ii) high chemical contrast of carbides and nitrides lying on the light support constituting the replica (C or Al(O<sub>x</sub>)) facilitates the observation of all sizes of all particles, down to about 2 to 3 nm [Courtois 06]; (iii) chemical analysis of carbon and/or nitrogen content in the precipitate becomes possible using replicas aluminium type (or Al oxide), while it is very difficult in thin foil (signal to noise ratio unfavorable due to the surrounding iron matrix).

Figure 2.4 presents the schematic principle of the electron detection in the case of Bright Field, Dark Field or HAADF images.

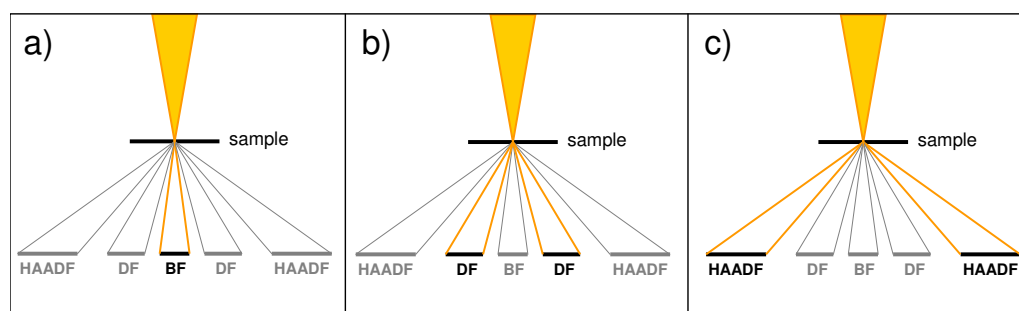


Figure 2.4: *Detection principle of electron in a) Bright Field; b) Dark field and c) HAADF.*

### 2.2.1.3 Chemical analysis by Energy Dispersive X-ray spectroscopy

The principle of chemical analysis by Energy Dispersive X-ray spectroscopy (EDX) is simple and is well detailed in the textbook of Williams and Carter [Williams 96]. The incident electrons excite the target atoms, which then emit X photons during their desexcitation. These X photons are collected and analyzed by an appropriate detection system, which allows to determine the nature of chemical elements and also to quantify their relative quantities.

The X photon detector is a p-i-n diode in silicon doped with lithium, which creates a current proportional to the X photon energy. In TEM, analysis volume is very small since the sample is thin. Thus, individual particles can be

easily analyzed with a small (i.e. nanometric) probe.

During EDX analysis some photons propagated in the direction of the detector are partially absorbed, either by the sample atoms (absorption effect of photons of lower energy) or by the detector protection window before reaching the analyzing crystal. These absorption effects are troublesome in the case of the study of nanometric precipitates composed by light elements (carbon, nitrogen, ...). Even with an ultra-thin window (UTW) as on the JEOL 2010F, the detection efficiency of light elements is less than unity (see table 2.4), which prevents any quantitative analysis of both carbon and especially nitrogen species. This problem with light elements has justified the dedicated EELS strategy developed in chapter 1.

Element	Be	B	C	N	O	F	Na	Al
Transmittance	0.1	0.36	0.6	0.38	0.6	0.7	0.95	1

Table 2.4: *Transmittance of the detector window for some elements*<sup>1</sup>.

Calibrations and various adjustments and/or corrections (noise peaks and peaks overlapping) are made automatically by the INCA software (by Oxford Instruments). After measurement of the area under a given peak for, say, two elements A and B, the atomic ratio between them is given by the formula including the so-called Cliff and Lorimer coefficients [Cliff 75] (see figure 2.5).

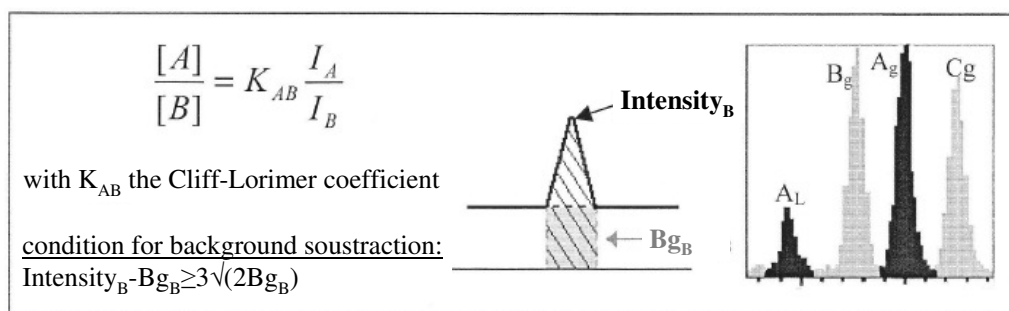


Figure 2.5: *Principle and limit of the EDX detection.*

For these reasons EDX has been employed here to determine the relative contents of the metallic species (V, Ti, Nb). However, accuracy of the analysis is not a stringent problem in the present work. Furthermore, the comparison

<sup>1</sup>supplied by Oxford Instruments, <http://www.oxinst.com>

of the EDX analysis with the EELS quantification methods as described in chapter 1 shows a concordance of both results within about 5 at.% uncertainty (see for example figure 1.14 in chapter 1).

### 2.2.2 Determination of particles radius

From HAADF images the particles are identified and dropped out manually by the analysis software developed at MATEIS by T. Epicier. The method consists in adjusting the particle contour with an ellipse of identical area. At the end of the analysis step we obtain a data file containing in particular the particle area, the two characteristic lengths of the ellipse (or the diameter in case of circular particles), the deviation from circularity and the equivalent spherical diameter. In our case, we have essentially circular particles (that can then be assumed to be spherical) but we also observe sometimes elongated particles (see figure 2.6). Thus, radius of precipitates are calculated from the two characteristic lengths of the equivalent ellipse.

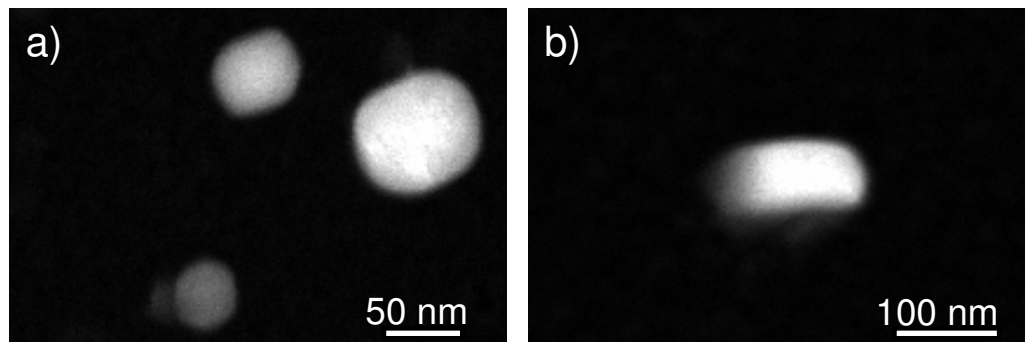


Figure 2.6: HAADF microographies of particles of the FeVNbCN alloy on an aluminium film: a) Spherical precipitates of the state treated 20 minutes at 900°C; b) Elongated precipitate of the state treated 200 minutes at 1050°C.

### 2.2.3 Precipitate volume fraction

#### 2.2.3.1 Determination of precipitate mass fraction

Among all experimental techniques available to estimate the precipitate volume, Thermoelectric Power measurement (TEP) is an easy to use and powerful technique [Perez 09]. Unfortunately, D. Acevedo showed that the influence of the martensitic structure is dominant and overcome the effect of precipitates

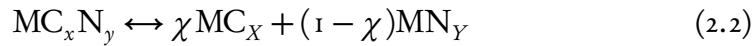
themselves. SEM in the BSE mode is also unable to quantify nanometric precipitate volume fraction because the resolution is too low to get any contrast. SEM in the SE mode combined with etching, is also inefficient in our case since the etching depth cannot be accurately measured. We may also consider scattering techniques (e.g. neutrons or X-rays) fruitfully used by F. Perrard during his PhD [Perrard 04]. However, chemical contrast between iron matrix and carbonitrides precipitates is low, leading to a very low signal over noise ratio with the SAXS technique. Finally, neutron scattering has been discarded from the point of view of accessibility and easy-to-use considerations.

Thus, for this study, we used the combination of electrolytic dissolution and inductively coupled plasma spectrometry (ICP). This technique has been employed for several years in CREAS to measure the content of precipitated elements in industrial steels.

The electrolytic dissolution method consists in the dissolution of the matrix into an electrolytic solution (lithium chloride + salicylic acid + methanol). Precipitates are collected by filtering this solution and the filter is then rinsed several times in methanol before being dissolved in a solution of H<sub>2</sub>O, HCl, HF, HNO<sub>3</sub> and HClO<sub>4</sub>. The residue is redissolved in a solution of HF and HNO<sub>3</sub> and is analyzed by an ICP spectrometer to give the precipitated mass fraction  $f_m$ . Further details are given in Appendix B.

### 2.2.3.2 Precipitate volume fraction calculation

In our material we can have precipitation of carbides, nitrides or carbonitrides. Thus, we suppose that all precipitates are a combination of a carbide and a nitride such as:



where M is the metallic element (vanadium or niobium) and  $\chi$  is the fraction of MC<sub>x</sub> molecules within the precipitate:

$$\chi = \frac{n_{MC}}{n_{MC} + n_{MN}} \quad (2.3)$$

$\chi = 1$  for a carbide and 0 for a nitride.

The volume fraction can be expressed as:

$$f_v^{M(C,N)} = \frac{v_{MC_xN_y}}{v_{tot}} \quad (2.4)$$

where  $v_{MC_xN_y}$  and  $v_{tot}$  are the atomic volumes of the precipitates and the matrix. In the case of a dilute solid solution (i.e. the density of the alloy is

considered equal to that of the iron), if the mass fraction of the precipitated element is defined as  $f_m^M = m_M^{M_{C_xN_y}} / m_{tot}$  (ratio of the mass of element M within the precipitates over the total mass of the alloy):

$$f_v^{M(C,N)} = f_m^M \frac{\rho_{Fe}}{\rho_{M(C_x,N_y)}} \left( \frac{\chi X M_C + (1 - \chi) Y M_N}{M_M} + 1 \right) \quad (2.5)$$

with  $\rho_{Fe}$  and  $\rho_{M(C_x,N_y)}$  the density of iron and precipitate respectively, and  $M_C$ ,  $M_N$  and  $M_M$  the atomic weight of C, N and M ( $M = Nb$  or  $V$ ) respectively.  $\rho_{M(C_x,N_y)}$  depends on the value of  $\chi$  such as:

$$\rho_{M(C_x,N_y)} = \frac{4 (M_M + X \chi M_C + Y (1 - \chi) M_N)}{(X \chi a_{MC} + Y (1 - \chi) a_{MN})^3 N_a} \quad (2.6)$$

with  $a_{MC}$  and  $a_{MN}$  the lattice parameters of the carbide and the nitride respectively, and  $N_a$  is the Avogadro number.

Note that  $M_C \approx M_N$ ,  $\chi$  has then almost no influence on precipitate volume fraction  $f_v^{M(C,N)}$ . Since  $\chi$  varies between 0 and 1, its influence on  $f_v^{M(C,N)}$  will be taken into account through uncertainties represented here after by error bars.

## 2.3 Experimental results

### 2.3.1 The 60SiCrV7+Nb industrial steel

In a first step, results of [Acevedo 07] obtained on the 60SiCrV7+Nb microalloyed steel are presented. For statistical interest some further data were collected on this material during the present study. They will then be compared with the experimental results obtained for the FeVNbCN model alloy in order to qualify the influence of the titanium and the nitrogen.

#### 2.3.1.1 Precipitate mass fraction

Determination of precipitate phases have been performed on all states of the 60SiCrV7+Nb industrial alloy. Results are shown on figure 2.7. The mass fraction of titanium does not really vary during heat treatments at all temperatures. Indeed, titanium in presence of nitrogen form titanium nitrides TiN at high temperature, which are stable in austenite. The solutionnizing of niobium is extremely small and this for all treatment temperatures, on the contrary of vanadium, which presents a fast solutionnizing for temperatures over 1000°C.

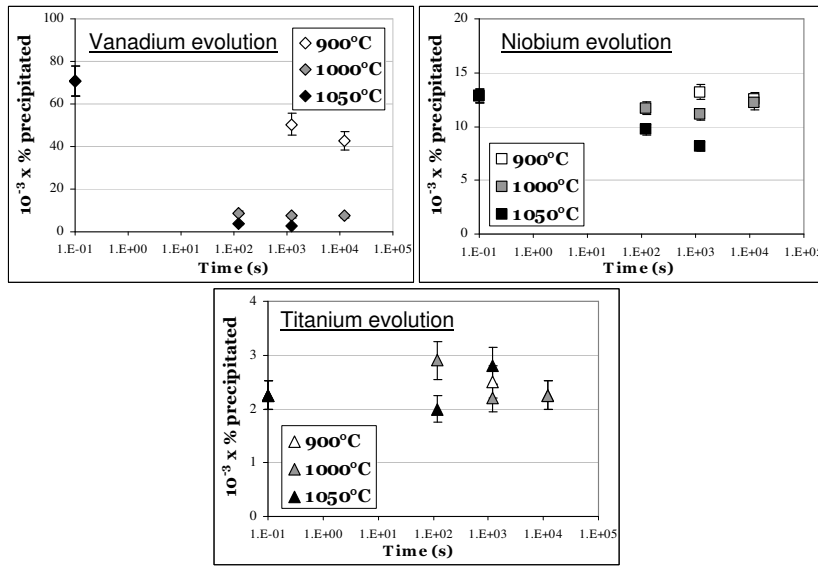


Figure 2.7: Evolution of vanadium, niobium and titanium precipitated mass fractions during heat treatment at 900°C, 1000°C and 1050°C for the 60SiCrV7+Nb industrial steel. Time 0.1 s corresponds to the As Rolled state.

### 2.3.1.2 Chemical composition of precipitates

During D. Acevedo's work, the chemical composition of precipitates were determined by EDX, thus only metallic elements such as Nb, V and Ti were analyzed. Some particles observed exhibit a core-shell structure with a core rich in titanium and a shell rich in niobium and vanadium. Figure 2.8.a presents an HAADF micrograph of a precipitate with such a structure. Figure 2.8.b shows the EDX line-scan performed on this precipitates, which highlights the enrichment in Ti in core. The existence of the "second shell" explains intensity difference observed on the HAADF image. Indeed, the presence of niobium increases the atomic number.

This kind of particles have been previously observed in similar systems containing titanium and nitrogen. Indeed, complex precipitates with a core-shell structure have been characterized in (Ti,V)(C,N) [Ooi 06], (Ti,Nb)(C,N) [Craven 00a], [Craven 00b], [Hong 02] and in (Ti,V,Nb)(C,N) [Hong 03] systems.

The evolution of the precipitates chemistry have been determined by the characterization of precipitate populations in the *As Rolled* state and in the reversion states. Figure 2.9 presents results obtain by EDX in TEM. Data are represented as ternary diagrams, which facilitates the visual perception of the general trends regarding the chemistry of particle. In the *As Rolled* state, pre-

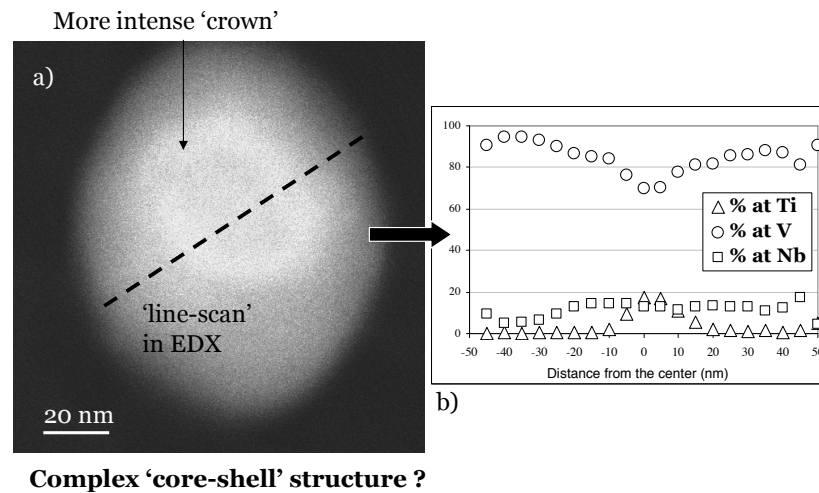


Figure 2.8: a) HAADF in STEM micrograph of a core-shell structure; b) Results of the EDX line-scan performed on this precipitate [Acedo 07].

precipitates are mainly rich in vanadium. After reversion treatments at  $1000^{\circ}\text{C}$  and  $1050^{\circ}\text{C}$ , particles get richer in niobium and titanium and the fraction of V-rich particles decreases. This can be explained as follows:

- Proportionally we observe more Nb-rich and Ti-rich particles due to the dissolution of V-rich precipitates.
- Some particles appear rich in titanium and niobium because of the selective solutionizing of vanadium.

### 2.3.1.3 Evolution of particles size

Figure 2.10 shows the particles mean radius for the *As Rolled* state and for heat treatments at  $1000^{\circ}\text{C}$  and  $1050^{\circ}\text{C}$ . Values presented correspond to the arithmetic average of measured radius. No variation of the mean radius for treatments at  $1000^{\circ}\text{C}$  was observed. Moreover, a light decrease was observed at  $1050^{\circ}\text{C}$ .

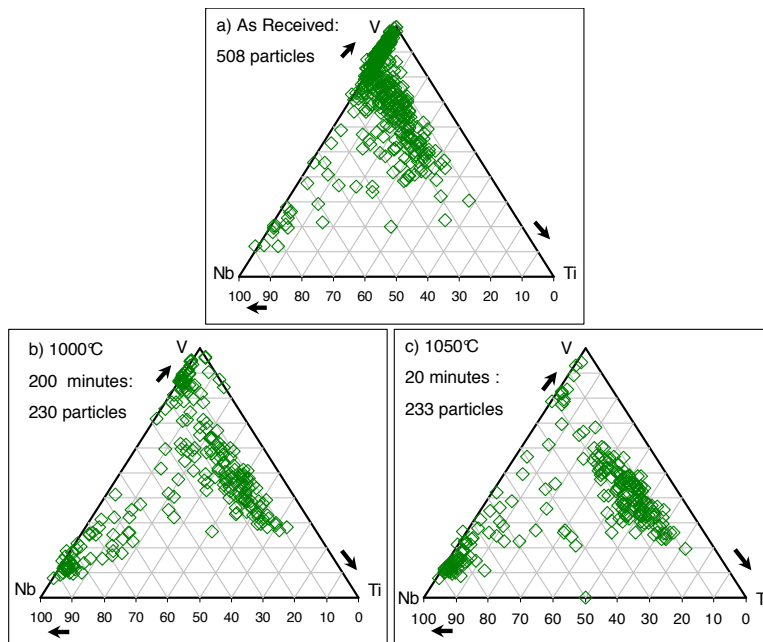


Figure 2.9: Particles chemistry evolution obtain by EDX in TEM. a) “As Rolled” state: many V-rich particles; b) “200 minutes at 1000°C” state and c) “20 minutes at 1050°C” state: particles are richer in niobium and titanium due to the solution-izing of vanadium. Results from the D. Acevedo’s PhD and from the further study performed during this work are reassembled on the figure.

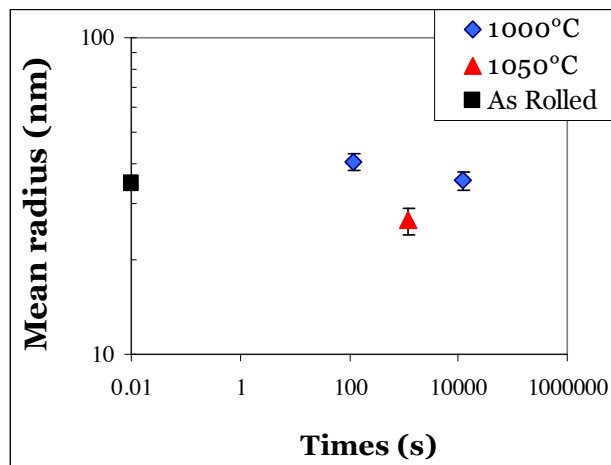


Figure 2.10: Mean radius measured for three states using HAADF in STEM micrographies. Results from D. Acevedo’s PhD have been completed by the analysis of a few hundreds additional particles.

### 2.3.2 The FeVNbCN model alloy

In this paragraph, results obtained for the FeVNbCN microalloyed steel are presented. Firstly the precipitate chemical composition obtained by EDX and EELS analysis will be reported. Then the evolution of precipitate size distribution will be discussed and finally, we will focus on the precipitate volume fraction.

#### 2.3.2.1 Chemical composition of precipitates

##### 2.3.2.1.1 EDX analysis

First, chemical analysis are performed by EDX to obtain the precipitate composition in “heavy” elements such as vanadium, niobium and also titanium expected to be present in a very minor content (see table 2.2). Analysis is performed on all states, and some HAADF in STEM micrographs are presented in figure 2.11. Figure 2.12 shows the evolution of precipitate chemical composition.

From figures 2.11.a and 2.12.a, EDX analysis on the *Fully Precipitated* state shows two kinds of precipitates, V-rich and Nb-rich. This is in agreement with [Frisk 08] and [Inoue 01] findings (see figure 2.13). However, V-rich precipitates are not totally pure (see figure 2.12.a) They indeed contain nearly 10 at.% of niobium. For the “Fully Precipitated” state, very few Nb-rich particles have been observed, compared to vanadium rich particles. This is due to the small Nb/V ratio of the investigated alloy (see alloy composition in table 2.2).

The number of Nb-rich particles increases with the temperature and or treatment duration. This is due to the solutionizing of V-rich precipitates, which have a lower stability. Small Nb-rich precipitates are detected for after 2 minutes at 1050°C (figure 2.11.d-e) while not in the initial state (*Fully Precipitated State*). This can be explained by (i) dissolution of vanadium rich precipitates followed by nucleation of niobium rich precipitates; or (ii) progressive enrichment in Nb of vanadium rich precipitates by selective dissolution of vanadium. The presence of mixed particles for treatments at 900°C and 1050°C (figure 2.12.d-g) gives some confidence in the scenario (ii) presented above: selective dissolution of the vanadium.

For a treatment of 2 minutes at 1200°C, figure 2.11.h presents a mixed precipitate but contiguous to a MnS particle. This precipitate may indeed consist in a fortuitous superposition of two precipitates V-rich and Nb-rich. Note that MnS were observed in all precipitation states. In the particular

case of the “1200°C-2 minutes” state, a large majority of analyzed particles were MnS precipitates: almost no vanadium or niobium rich particles were found. These particles were in all cases, contiguous to a MnS or mixed with MnS. Thus, for the following, all (Nb,V)(C,N) precipitates are supposed to be dissolved after 2 minutes at 1200°C.

During TEM observations, no precipitate with a core-shell structure have been found. It can be postulated that the titanium content of the alloy is too low to form precipitates with a core rich in titanium, as observed in the 60SiCrV7+Nb industrial steel, which contains 2.5 times more titanium.

### 2.3.2.1.2 EELS analysis

Two precipitate populations have been observed. From the EDX results, it is not possible to know if Nb-rich and V-rich precipitates are carbides, nitrides or carbonitrides, and for that reason EELS is required. We have seen in chapter 1 that compositions obtained by EELS are in good agreement with those obtained by EDX for niobium, vanadium and titanium. We are thus confident for results on carbon and nitrogen composition.

According to the fact that EELS experiments are relatively time-consuming, especially when performed at the liquid nitrogen temperature, we performed these measurements only on a selection of states: *Fully Precipitated*, “200 minutes at 900°C” and “2 minutes at 1050°C” states. Figure 2.14 presents two EELS spectrum of carbonitrides from the “200 minutes at 900°C” state. We report on figure 2.14.a the EELS spectrum of a niobium carbide with some vanadium, and on figure 2.14.b the EELS spectrum of a vanadium carbonitride. More results are given in figure 2.15, which presents ternary diagrams of investigated states to see the precipitate chemical composition in both metallic elements (V, Nb, Ti) and in nitrogen and carbon. We can also report here the average composition  $MX_{1-\delta}$ , when M yields for all metallic species, and X for both carbon and nitrogen content. Overall particles at all any treatments, we found a systematic slight sub-stoichiometry  $MX_{0.85\pm 0.05}$ , which was already noticed in previous work [Courtois 05]. The error bar is essentially due to the accuracy of the EELS analysis [Courtois 06].

It is observed that Nb-rich precipitates are mainly rich in carbon for all temperatures. For V-rich particles we observe an evolution of the nitrogen content. Indeed, precipitates analyzed in the *Fully Precipitated* state are mainly rich in carbon. We can see a similar behavior for precipitates observed in the state treated 200 minutes at 900°C. However, after the treatment of 2 minutes at 1050°C V-rich particles are much richer in nitrogen in comparison with

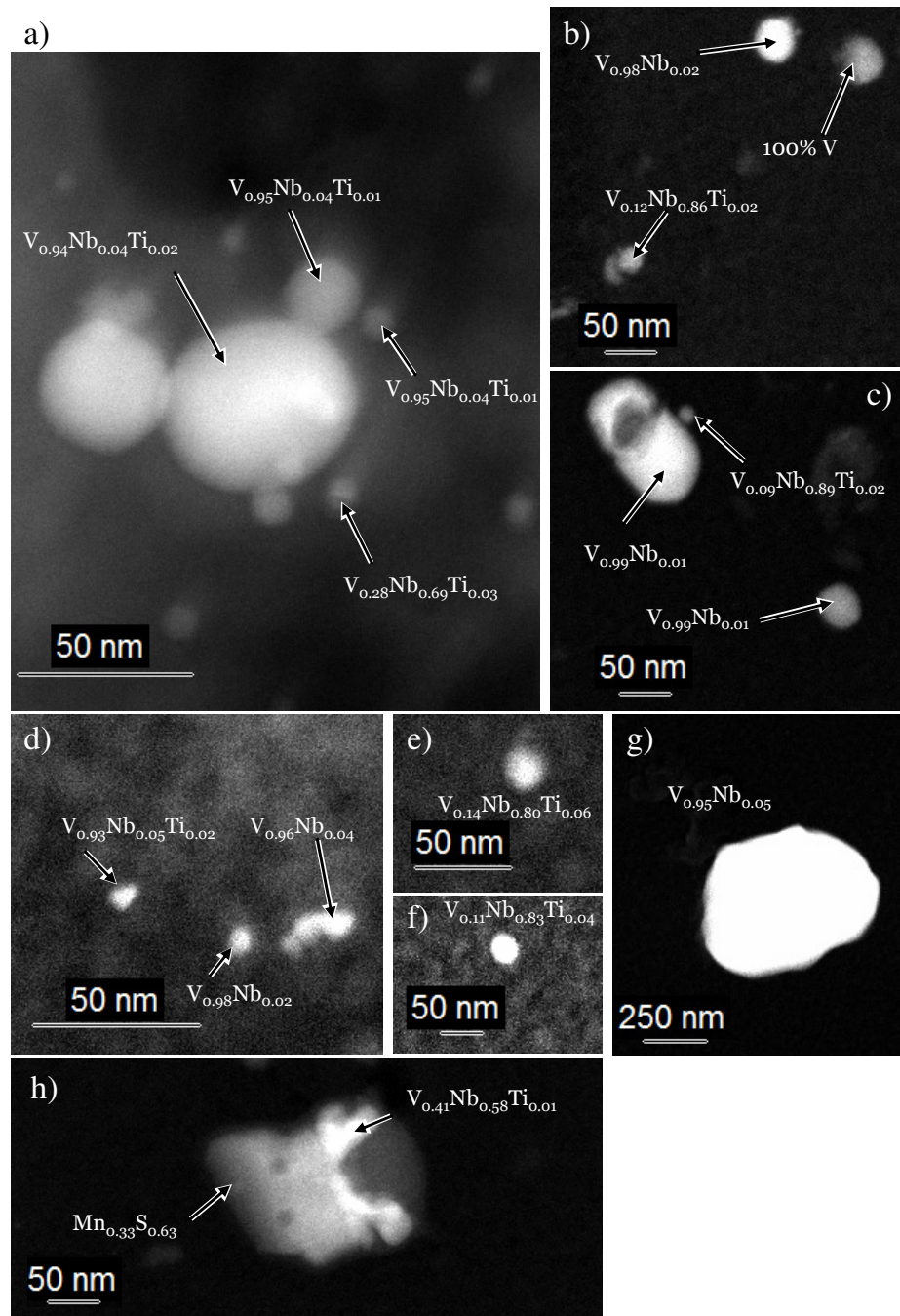


Figure 2.11: HAADF in STEM microographies of microalloyed steel FeVNbCN for states: a) Fully Precipitated State; b) 900°C - 20 minutes; c) 900°C - 200 minutes; d) and e) 105°C - 2 minutes; f) and g) 105°C - 20 minutes; h) 1200°C - 2 minutes. Precipitate chemical composition shown on the figure were obtained by EDX.

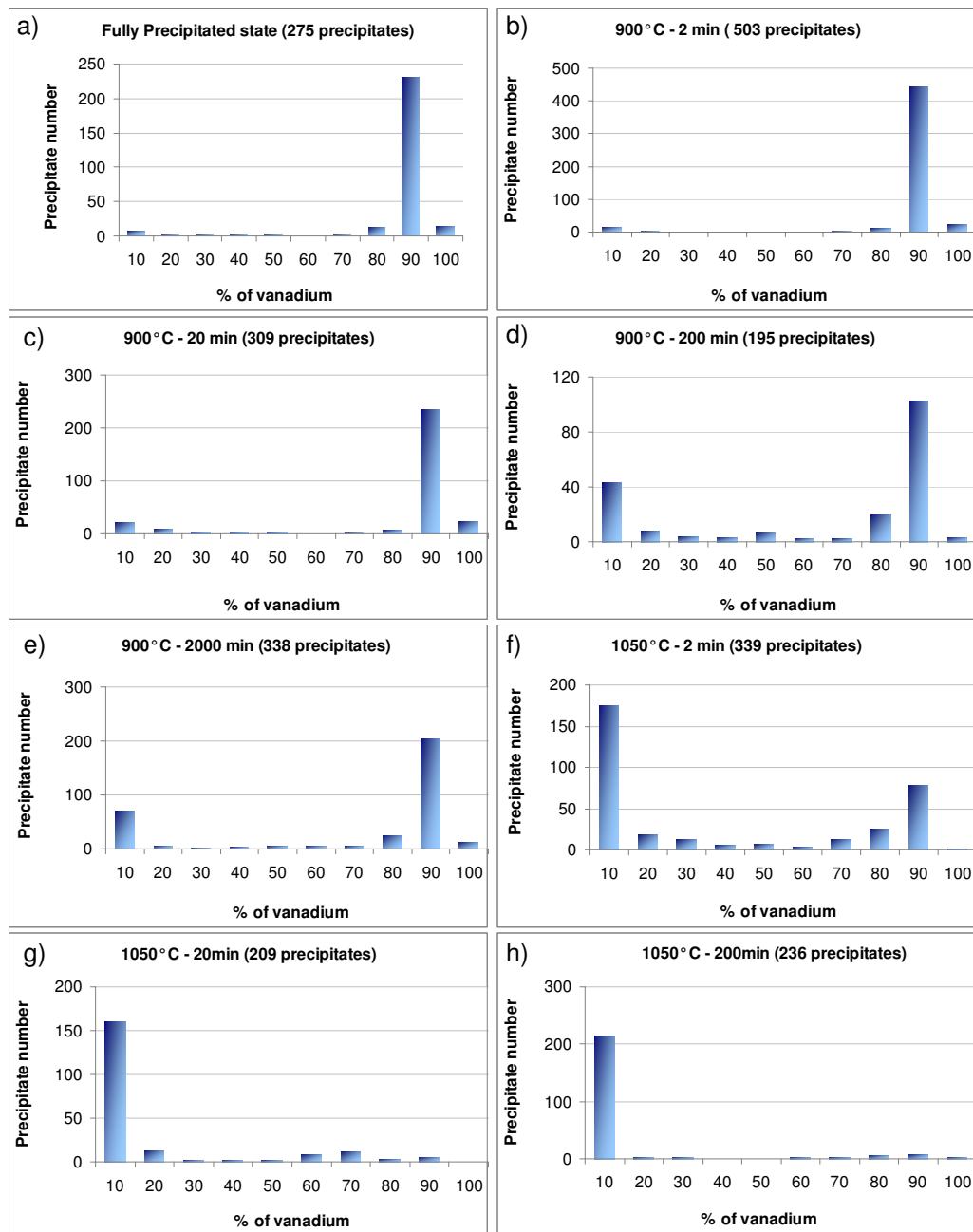


Figure 2.12: *Time evolution of precipitate chemical composition for several temperatures (EDX analysis).*

the two previous state. Thus, we will consider later that Nb-rich precipitates are niobium carbides whereas, V-rich precipitates are vanadium carbonitrides.

To complete this chemical analysis, equilibrium thermodynamic cal-

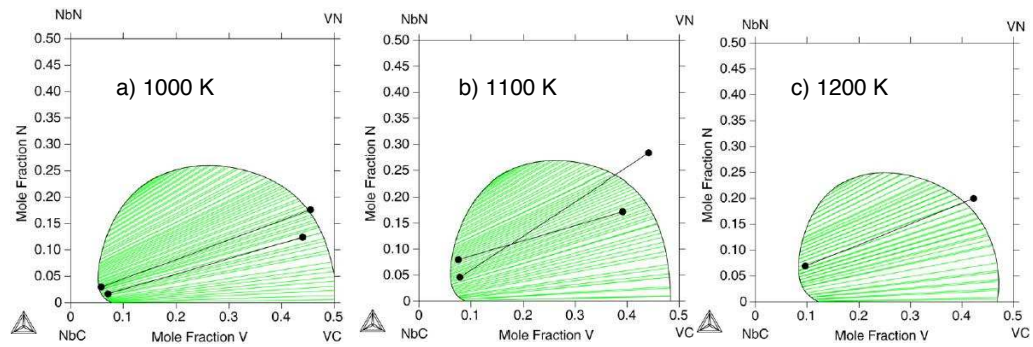


Figure 2.13: The calculated miscibility gap from in the Nb-V-C-N system at a) 1000 K, b) 1100 K and c) 1200 K, in equilibrium Fe-base matrix [Frisk 08], compared with experimental results (dark dots and lines) from the work of [Inoue 01].

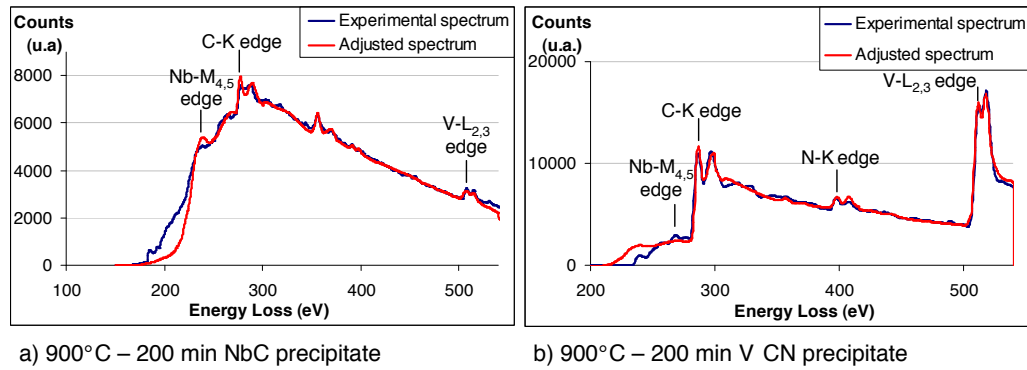


Figure 2.14: EELS spectra from carbonitrides on aluminium replica of the FeVN-bCN alloy treated 200 minutes at 900°C. a) Spectrum of niobium carbide with some vanadium; b) spectrum of vanadium carbonitride with some niobium.

calculations have been performed with Thermo-Calc software and the TCFE<sub>5</sub> database [TCFE<sub>5</sub> 05]. Figure 2.16.a presents the V(Nb)CN and Nb(V)CN precipitate mass fraction versus temperature. Figure 2.16.b gives the mass fraction of vanadium and niobium. TCFE<sub>5</sub> database predicts two mixed precipitates (V,Nb)(C,N) kinds: one rich in vanadium and the other one rich in niobium. Vanadium starts to be solutionized before niobium but remains within precipitates up to 1100°C. This explains the presence of vanadium within carbonitrides experimentally demonstrated at 1050°C (see figure 2.15).

Figure 2.17 shows carbon over nitrogen ratio for both Nb and V-rich precipitates predicted by TCFE<sub>5</sub> [TCFE<sub>5</sub> 05]. It is clear that niobium rich particles are extensively rich in carbon (C/N > 20), whereas vanadium rich precipitates exhibit a C/N ratio of about 1, in total agreement with EELS measure-

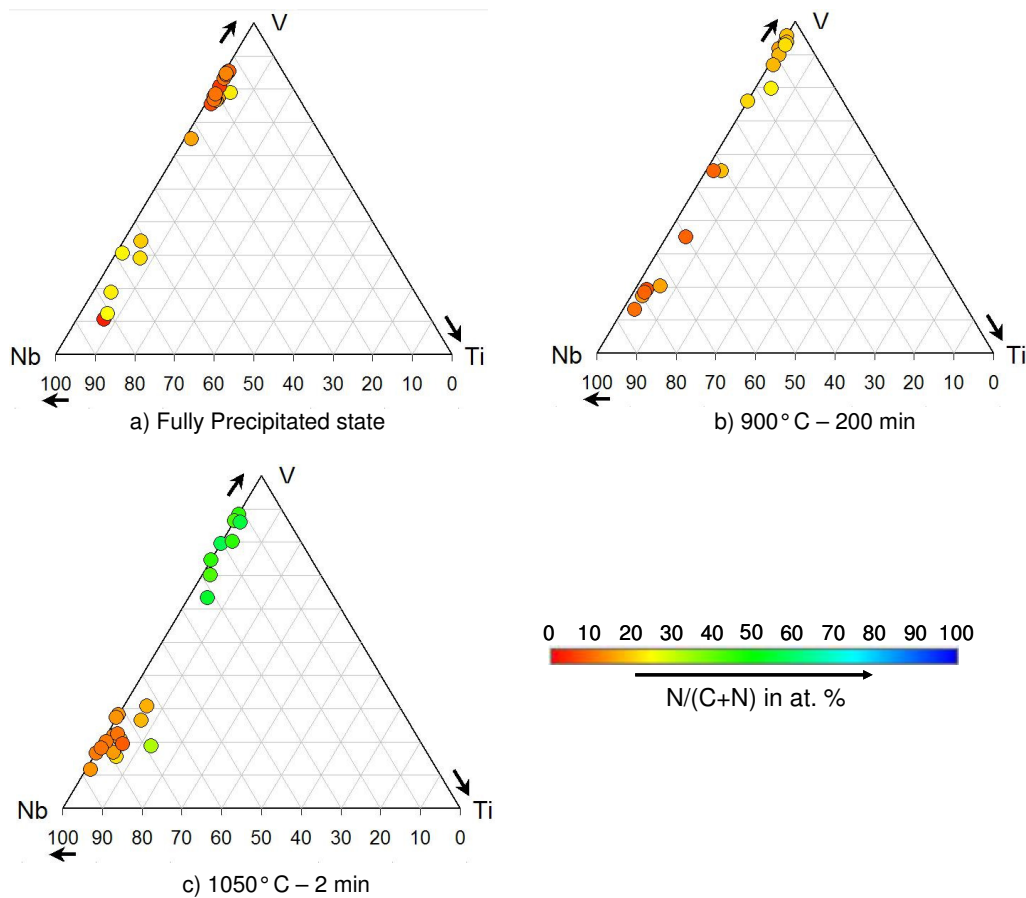


Figure 2.15: Ternary diagrams showing the chemical composition of each analyzed precipitates for: a) the Fully Precipitated state, b) the 900°C - 200 minutes state and c) the 1050°C - 2 minutes state. A nitrogen content scale is presented on the figure, from red for pure carbides to blue for pure nitrides. We can see that Nb-rich precipitates are mainly rich in carbon, while V-rich particles are rich in both carbon and nitrogen.

ment (see figure 2.15). Moreover, for both precipitate kinds, there is a decrease in the C/N ratio when increasing temperature. Finally, vanadium rich precipitates become richer in nitrogen than in carbon for temperatures greater than 1000°C, which is, once again, in agreement with EELS experimental results.

### 2.3.2.2 Evolution of precipitate size

#### 2.3.2.2.1 Mean radius evolution

The precipitate mean radius is deduced from measurements performed

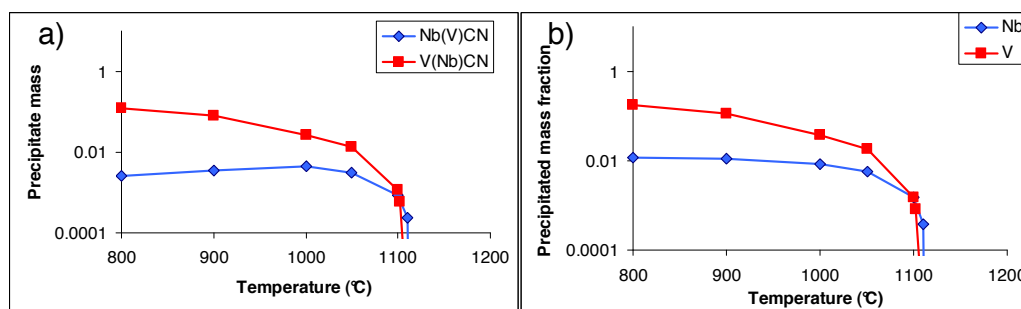


Figure 2.16: Evolution with the temperature of a)  $V(Nb)CN$  and  $Nb(V)CN$  precipitates mass and b) precipitated mass fraction of vanadium and niobium in the  $FeVNbCN$  model alloy (results obtained with the Thermo-Calc software [TCFE5 05]).

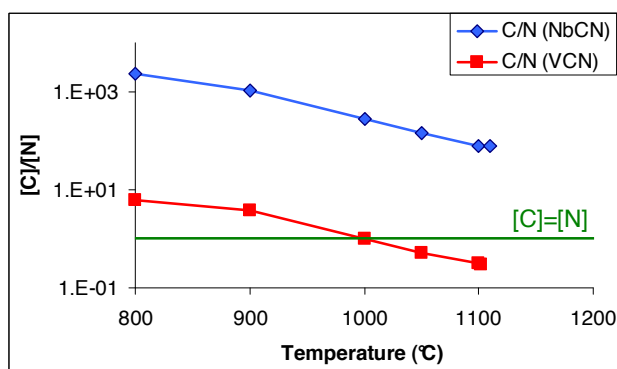


Figure 2.17: Thermo-Calc calculation of the  $C/N$  ratio in vanadium and niobium particles [TCFE5 05].

on HAADF images, and the quoted value in the following corresponds to the arithmetic average of all measured radii. These size measurements, and systematic associated EDX analysis, were performed on about 300 particles in each state. It was obviously not possible to perform EELS analysis on all these particles. Thus, according to the EDX identification of V-rich and Nb-rich particles, particles with more than 50% atomic of vanadium are considered as VCN, and the others as NbC particles. Figure 2.18 presents the evolution of the precipitate mean radius for these two particles types.

For a reversion at 900°C there is no significative evolution of VCN and NbC mean radii even for long treatments. Whereas we observe a slight increase of the mean radius of both precipitate types for reversion at 1050°C. Furthermore, the sizes of VCN are systematically larger than that of NbC particles.

Error bars present on the figure are the sum of errors of measures (due to the manual treatment of HAADF micrographies), and the statistic error of the measure (which depends of number of observed particles: the weaker the number is, the more important is the errors).

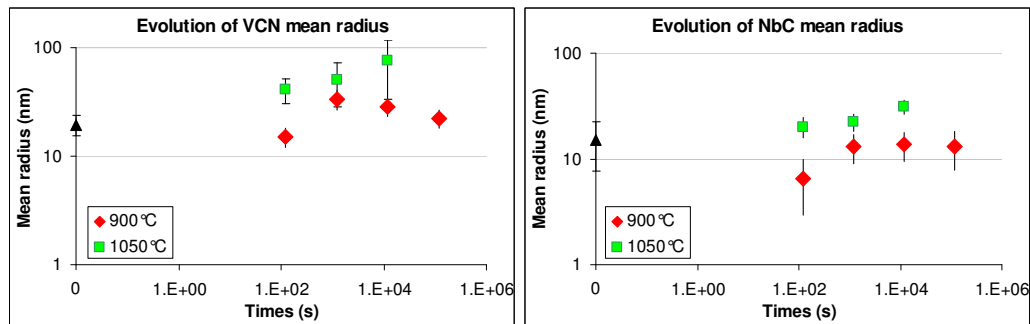


Figure 2.18: *Evolution of VCN and NbC mean radius with treatment duration and temperature in the FeVNbCN model alloy. Precipitates with more than 50% of vanadium are considered as VCN. Error bars take into account the quantity of observed particles.*

#### 2.3.2.2.2 Correlation between the precipitate size and chemistry

Figure 2.19 presents the correlation between the precipitate chemical composition (in terms of the metallic elements) and the precipitate size for all investigated states. Each mark represents an analyzed particle. For the *Fully Precipitated State*, Nb-rich particles are systematically smaller, and large particles are V-rich precipitates. With a reversion treatment, the Nb-rich precipitates fraction increases and so does their radius. The number of V-rich particles decreases with the increase of treatment temperature. We also observe some mixed particles with a composition of vanadium within 25% to 75%. These particles may come from the dissolution of V-rich precipitates present in the *Fully Precipitated State*, and which contain niobium, which is in agreement with the EDX analysis.

#### 2.3.2.3 Evolution of precipitate volume fraction

The precipitate volume fraction is calculated using the equation 2.5 given in paragraph 2.2.3.2. As previously said, V-rich particles are treated as vanadium carbonitrides, while for Nb-rich precipitates we consider niobium carbide.

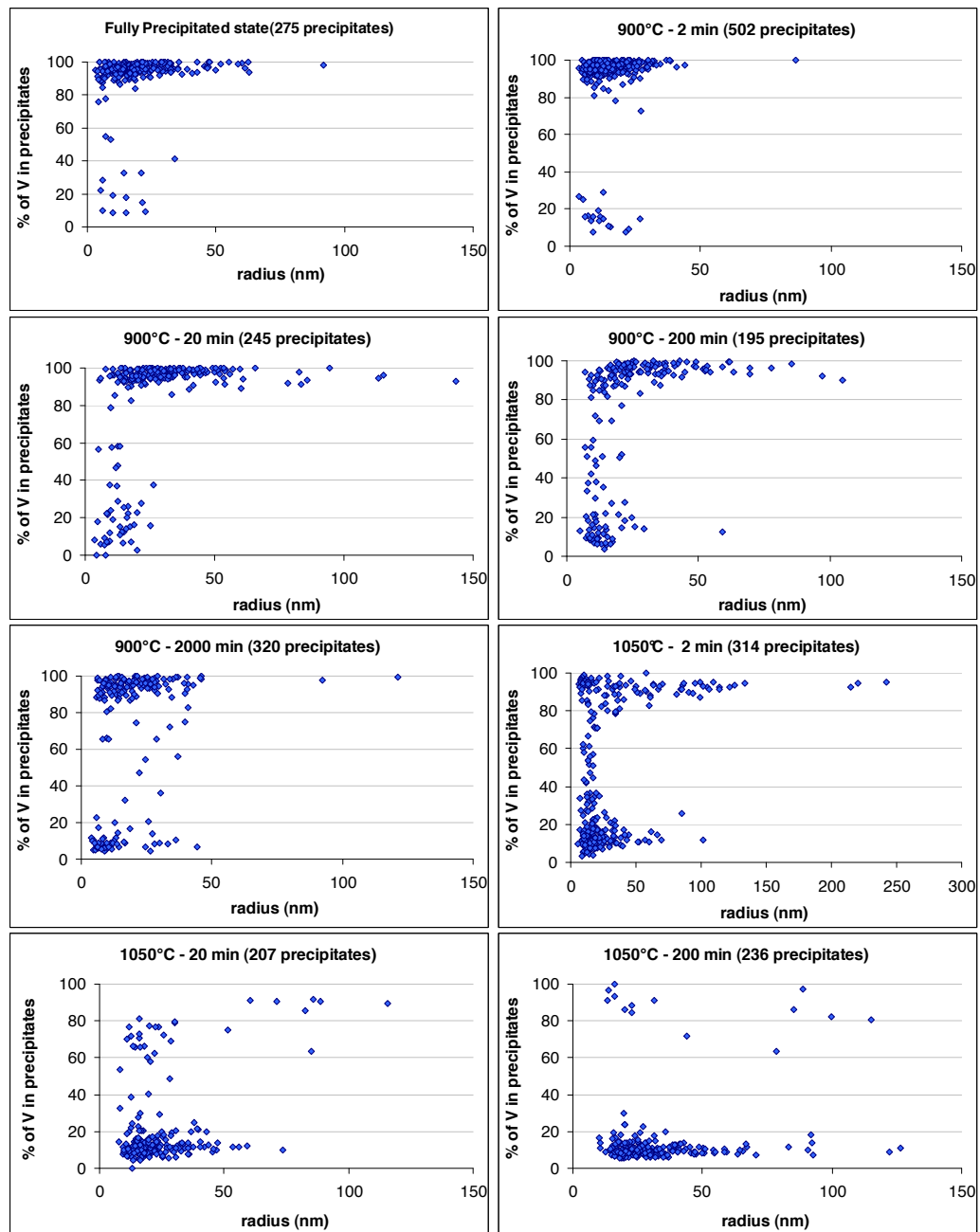


Figure 2.19: Correlation between precipitate chemical composition measured by EDX and their size measured on HAADF images for all investigated states. We observe an evolution of the particle sizes but also of the chemistry: the higher the temperature, the higher the ratio of niobium particles.

Parameters used are given in table 2.5.

Vanadium atomic weight	50.94 g.mol <sup>-1</sup>
Niobium atomic weight	92.91 g.mol <sup>-1</sup>
Carbon atomic weight	12.01 g.mol <sup>-1</sup>
Nitrogen atomic weight	14.01 g.mol <sup>-1</sup>
Iron density	7874 kg.m <sup>-3</sup>
VC lattice parameter (cfc)	4.165 10 <sup>-10</sup> m
VN lattice parameter (cfc)	4.118 10 <sup>-10</sup> m
NbC lattice parameter (cfc)	4.471 10 <sup>-10</sup> m

Table 2.5: Parameters used for the precipitate volume fraction calculation from the results of the electrolytic dissolution.

Figure 2.20 presents the evolution of the volume fraction of VC<sub>x</sub>N<sub>y</sub> and NbC. Vanadium carbonitrides start to be slightly solutionnized at 900°C. At 1050°C and over, nearly all the vanadium is solutionnized even for short treatments. For niobium, at 900°C there is no change in the volume fraction but from 1050°C it starts to be solutionnized.

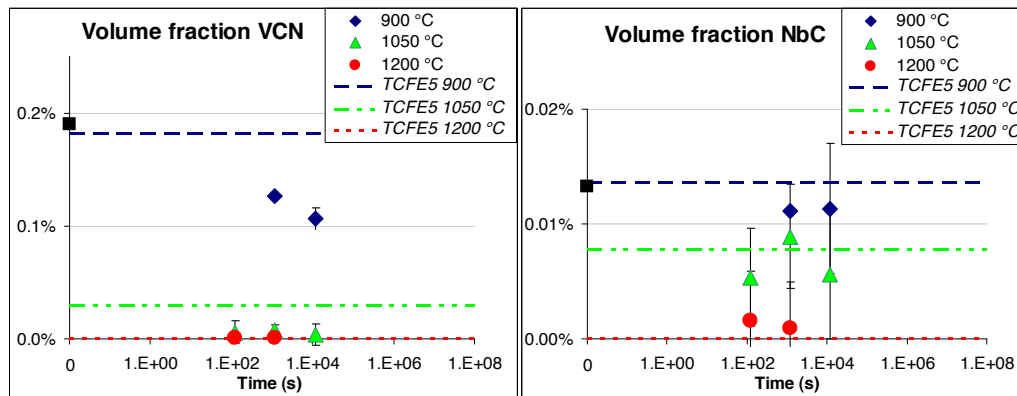


Figure 2.20: Evolution of volume fraction of a) VCN and b) NbC. Thermodynamic equilibria calculated with the ThermoCalc software [TCFE5 05] are given on the figure.

### 2.3.3 Comparison of both industrial and model alloys

In this section, we have presented and completed results of a previous work on the 60SiCrV7+Nb industrial steel [Acevedo 07], and we also reported those of the FeVNbCN model alloy elaborated during this study. The aim was to compare the evolution of precipitation state of these two alloys in order to

understand the nitrogen and titanium roles in this evolution (see figures 2.21 and 2.22). Principal results of this experimental study are the following:

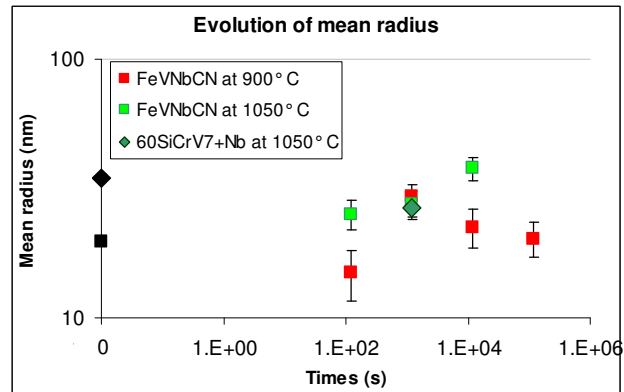


Figure 2.21: Evolution of the precipitate mean radius for the FeVNbCN and the 60SiCrV7+Nb microalloyed steel.

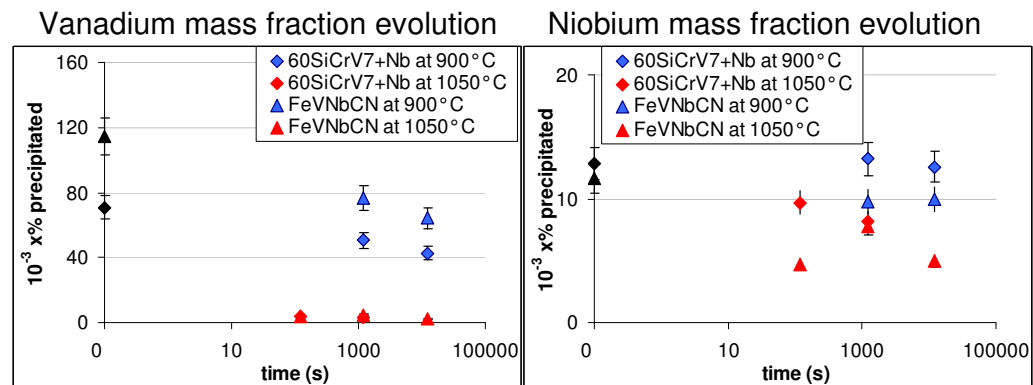


Figure 2.22: Evolution of mass fraction for the 60SiCrV7+Nb industrial steel and for the FeVNbCN model alloy of a) Vanadium and b) Niobium.

- Both industrial and model alloys contain separated populations of V-rich and Nb-rich precipitates. Owing to its larger titanium content, the industrial grade exhibits some Ti-rich precipitates, while the model alloy contains few mixed precipitates.
- The increase of temperature leads to an increase of niobium precipitates ratio and of precipitate size in both alloys.

- No significant differences have been observed in the precipitation state evolution (mean radius and precipitated mass fraction) for the two investigated steels.
- For the FeVNbCN microalloyed steel, EELS analysis demonstrated the presence of niobium carbides and vanadium carbonitrides with an enrichment in nitrogen with the increase of the temperature. According to the resemblance of both alloys, we may extrapolate that this is also the case for the industrial alloy (although EELS was not performed).
- The main difference between both steels is that core-shell particles have been observed only in the 60SiCrV7+Nb steel. The presence of titanium in a very small quantity does probably not allow the formation of this structure in the model alloy.

At this stage, it would be appreciable to have thermodynamical elements to complete the understanding of the precipitation state, and its evolution during reversion treatments, and also to predict this evolution. For that purpose a tentative model of precipitation/reversion is presented in the next section. Results obtained in the experimental part allow to build the initial precipitate size distribution for the reversion modelling of the *Fully Precipitated State*. These precipitate size distributions will be obtained by considering two precipitate kinds: VCN and NbC. Precipitates with more than 50% of vanadium will be considered as VCN.

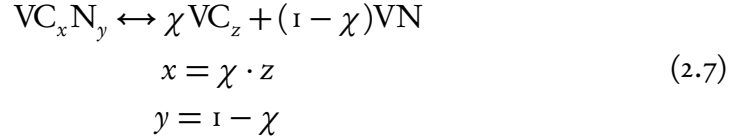
## 2.4 A model for precipitation kinetics

In this section, a model, based on classical nucleation and growth theories (see the review of Kampmann and Wagner [Kampmann 91]), is developed in order to follow the precipitation state evolution within a steel containing vanadium, niobium, carbon and nitrogen. The aim is to further document the nitrogen influence in the precipitate solutionizing kinetics during reversion treatments. This model will take into account the evolution of carbides, nitrides and carbonitrides.

### 2.4.1 Hypothesis

The main and probably more important result deduced from the previous experimental studies is that we have essentially two particle types: V-rich precipitates and Nb-rich precipitates. Furthermore, in his work on a FeVNbC model

alloy, [Acevedo 07] showed that precipitates were NbC and  $V_6C_5$ . While, the study of the FeVNbCN microalloyed steel shows the presence of NbC and VCN precipitates. Thus, in the present model we take into account two precipitate types: NbC pure and complex ternary  $VC_xN_y$ . The composition of the vanadium carbonitride  $VC_xN_y$  is treated as an ideal solution of  $VC_z$  ( $z = 0.8333$ ) and VN such as:



with  $\chi$  the fraction of  $VC_z$  precipitates on the precipitate total number:

$$\chi = \frac{n_{VC_z}}{n_{VC_z} + n_{VN}} \quad (2.8)$$

The precipitation thermodynamic model has been developed by D. Acevedo [Acevedo 07]. Details of thermodynamic calculation are given in his thesis, we just summarize here the principal points of this model:

1. Precipitates are spherical.
2. The growth is controlled by long distance diffusion.
3. There is a local equilibrium at the precipitate/matrix interface, corrected by the Gibbs Thomson effect (interface curvature).
4. The driving force corresponds to that of the regular dilute solution.

Starting from these general assumptions, the next sub-section describes the model developed for the situation considered here.

## 2.4.2 Thermodynamic of carbides, nitrides and carbonitrides

### 2.4.2.1 Equilibrium

In the case of a dilute solid solution, the carbides and nitrides formation energy in equilibrium with the matrix is given by a variation of  $\Delta G_{NbC}$ ,  $\Delta G_{VC_z}$  and  $\Delta G_{VN}$  free enthalpy:

$$\Delta G_{NbC} = kT \ln \left( X_{Nb}^i X_C^i \right) \quad (2.9)$$

$$\Delta G_{VC_z} + (1 - \chi)^2 \Omega_{CN}^{VC_x N_y} = kT \ln \left( \frac{X_V^i (X_C^i)^z}{3^z \chi} \right) \quad (2.10)$$

$$\Delta G_{VN} + \chi^2 \Omega_{CN}^{VC_x N_y} = kT \ln \left( \frac{X_V^i X_N^i}{1 - \chi} \right) \quad (2.11)$$

where  $k$  is the Boltzmann's constant,  $T$  the temperature,  $X_M^i$  the atomic fraction of the element  $M$  in solid solution at equilibrium and  $\Omega_{CN}^{VC_x N_y}$  an interaction parameters of the elements  $C$  and  $N$  in  $VC_x N_y$ . Calculation details of equations 2.10 and 2.11 are given in appendix C

From equations 2.9 to 2.11 we can define  $K_{NbC}$ , and regular  $K_{VC_z}^R$  and  $K_{VN}^R$  solubility products, which are function of ideal  $K_{VC_z}$  and  $K_{VN}$  solubility products:

$$K_{NbC} = \exp \left( \frac{\Delta G_{NbC}}{kT} \right) = X_{Nb} X_C \quad (2.12)$$

$$\begin{aligned} K_{VC_z}^R &= \frac{X_V^i (X_C^i)^z}{3^z \chi} = 3 \exp \left( \frac{\Delta G_{VC_z} + (1 - \chi)^2 \Omega_{CN}^{VC_x N_y}}{kT} \right) \\ &= K_{VC_z} \exp \left( \frac{(1 - \chi)^2 \Omega_{CN}^{VC_x N_y}}{kT} \right) \end{aligned} \quad (2.13)$$

$$K_{VN}^R = \frac{X_V^i X_N^i}{1 - \chi} = \exp \left( \frac{\Delta G_{VN} + \chi^2 \Omega_{CN}^{VC_x N_y}}{kT} \right) = K_{VN} \exp \left( \frac{\chi^2 \Omega_{CN}^{VC_x N_y}}{kT} \right) \quad (2.14)$$

$K_{VC_z}$  and  $K_{VN}$  are obtained from  $VC_z$  carbide and  $VN$  nitride as  $K_{NbC}$  (see equation 2.12).

#### 2.4.2.2 Driving force for precipitation

In the case of  $NbC$  and  $VC_x N_y$  precipitates, the volumes of one molecule of these particles are given by  $v_{NbC}^p = 2v_{at}^{NbC}$  and  $v_{VC_x N_y}^p = (1+x+y)v_{at}^{VC_x N_y}$  (where  $v_{at}^{NbC}$  and  $v_{at}^{VC_x N_y}$  are the mean atomic volume within the precipitate). The driving force for these precipitates is then:

$$\delta g^{\text{NbC}} = \frac{kT}{v_{\text{NbC}}^p} \ln \left[ \frac{X_{\text{Nb}}X_{\text{C}}}{K_{\text{NbC}}} \right] \quad (2.15)$$

$$\delta g^{\text{VC}_x\text{N}_y} = \frac{kT}{v_{\text{VC}_x\text{N}_y}^p} \ln \left[ \frac{(X_{\text{V}}X_{\text{C}}^z)^\chi (X_{\text{V}}X_{\text{N}})^{(1-\chi)}}{(3^{(z-1)}\chi K_{\text{VC}_z})^\chi [(1-\chi)K_{\text{VN}}]^{(1-\chi)}} \right] \quad (2.16)$$

Equations 2.15 and 2.16 can be expressed as:

$$\delta g^{\text{NbC}} = \frac{kT}{v_{\text{NbC}}^{\text{NbC}}} S_{\text{NbC}} \quad (2.17)$$

$$\delta g^{\text{VC}_x\text{N}_y} = \frac{kT}{v_{\text{VC}_x\text{N}_y}^{\text{VCN}}} S_{\text{VC}_x\text{N}_y} \quad (2.18)$$

with:

$$S_{\text{NbC}} = \ln \left[ \frac{X_{\text{Nb}}X_{\text{C}}}{K_{\text{NbC}}} \right] \quad (2.19)$$

$$S_{\text{VC}_x\text{N}_y} = \ln \left[ \frac{(X_{\text{V}}X_{\text{C}}^z)^\chi (X_{\text{V}}X_{\text{N}})^{(1-\chi)}}{(3^{(z-1)}\chi K_{\text{VC}_z})^\chi [(1-\chi)K_{\text{VN}}]^{(1-\chi)}} \right] \quad (2.20)$$

where  $S_{\text{NbC}}$  and  $S_{\text{VC}_x\text{N}_y}$  can be defined as the solution supersaturation in NbC and  $\text{VC}_x\text{N}_y$ , respectively.

### 2.4.2.3 Nucleation<sup>1</sup>

The free energy formation in the solid solution of a NbC or  $\text{VC}_x\text{N}_y$  nucleus of radius  $R$ , if neglecting any effect of elastic deformation, is given by:

$$\Delta G(R) = \frac{4}{3}\pi R^3 \Delta g + 4\pi R^2 \gamma \quad (2.21)$$

where  $\gamma$  is the precipitate/matrix interface energy. The first term corresponds to an energy gain due to the formation of a more stable phase, while the second term corresponds to an energy loss due to the formation of a new interface.

<sup>1</sup>Although not used within this work, the classical nucleation theory is briefly recalled here.

The formation free energy variation  $\Delta G$  versus the precipitate radius  $R$  in the case of a supersaturated matrix is shown on figure 2.23. This function presents a maximum, thus the surface and volume effects are antagonistic. For small radius, the surface energy dominates, whereas for larger radius, the volume energy becomes dominant and makes the  $\Delta G$  value negative.

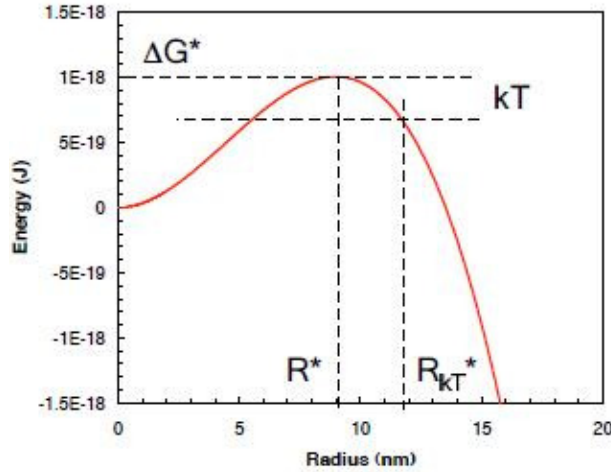


Figure 2.23: Schematic representation of the nucleation free energy variation versus precipitate radius.

The critical radius  $R^*$  is the limit between stable and unstable precipitates. The value of  $R^*$  is given by:

$$R^* = -\frac{2\gamma}{\Delta g} = \frac{R_o}{S_p} \quad (2.22)$$

where the value of  $S_p$  is given by equations 2.19 and 2.20 ( $p = \text{NbC}$  or  $\text{VC}_x\text{N}_y$ ) and the expression of  $R_o$  (the capillarity length) can be written as:

$$R_o^{\text{NbC}} = 2 \frac{\gamma v_{\text{NbC}}^p}{kT} \quad (2.23)$$

$$R_o^{\text{VC}_x\text{N}_y} = 2 \frac{\gamma v_{\text{VC}_x\text{N}_y}^p}{kT} \quad (2.24)$$

We can then define  $\Delta G^*$ , the nucleation barrier, by introducing the  $R^*$  expression into equation 2.21:

$$\Delta G^* = \frac{16}{3} \pi \gamma^3 \Delta g^2 = \frac{\Delta G_o}{S_p} \quad (2.25)$$

with:

$$\Delta G_o = \frac{4}{3}\pi R_o^2 \gamma \quad (2.26)$$

$\Delta G^*$  is the energetic barrier that sub-critical nuclei have to overpass to become supercritical.

The nucleation rate is calculated via the classical Becker-Döring theory, modified by Zeldovich, taking into account the driving force and the free energy increase due to the creation of an interface between both phases. This approach gives the nucleation rate as the derivation of the precipitate density  $N$  of each phase given by [Kampmann 91] and modified by [Maugis 05]:

$$\frac{dN}{dt} = N_o Z \beta^* \exp\left[-\frac{\Delta G^*}{kT}\right] \left(1 - \exp\left[-\frac{t}{\tau}\right]\right) \quad (2.27)$$

Parameters of equation 2.27 come from the works of Russell [Russell 68] and of Wagner *et al.* [Wagner 91].  $N_o$  is the number of nucleation sites per unit volume ( $\approx 1/v_{at} = 2/a^3$  for a bcc structure with a lattice parameter  $a$ ),  $Z$  is the Zeldovitch's factor and  $\tau$  the incubation time. The other parameters of equation 2.27 are expressed as follows:

$$\beta^* = \frac{4\pi R^{*2} DX}{a^4} \text{ with } R^* = \frac{R_o}{S_p} \quad (2.28)$$

$$\tau = \frac{1}{2\beta^* Z} \text{ with } Z = \frac{v_{at}}{2\pi R^{*2}} \sqrt{\frac{R_o}{2v_{at}}} \quad (2.29)$$

#### 2.4.2.4 Gibbs-Thomson effects

Due to the presence of interface between matrix and precipitates, equilibrium mole fractions are modified. This is the so-called Gibbs-Thomson effect [Perez 05]. The interfacial energy expressed as follows:

$$K_{NbC} \exp\left[\frac{R_o}{R}\right] = X_{Nb}^i X_C \quad (2.30)$$

$$K_{VC_z}^R \exp\left[\frac{R_o}{R}\right] = K_{VC_z} \exp\left[\frac{(1-\chi)^2 \Omega_{CN}^V}{kT}\right] \exp\left[\frac{R_o}{R}\right] = \frac{X_V^i (X_C^i)^z}{\chi} \quad (2.31)$$

$$K_{VN}^R \exp\left[\frac{R_o}{R}\right] = K_{VN} \exp\left[\frac{\chi^2 \Omega_{CN}^V}{kT}\right] \exp\left[\frac{R_o}{R}\right] = \frac{X_V^i X_N^i}{1-\chi} \quad (2.32)$$

## 2.4.2.5 Growth and coarsening

The growth of precipitate phase is described by the Fick equation in stationary regime, and the precipitate growth rate is simultaneously bound to the various elements concentrations by:

$$\left\{ \begin{array}{l} \left. \frac{dR}{dt} \right|_{\text{Nb}} = \frac{D_{\text{Nb}}}{R} \frac{X_{\text{Nb}} - X_{\text{Nb}}^i(R)}{\alpha_{\text{NbC}} X_{\text{Nb}}^{\text{NbC}} - X_{\text{Nb}}^i(R)} \\ \left. \frac{dR}{dt} \right|_{\text{C}} = \frac{D_{\text{C}}}{R} \frac{X_{\text{C}} - X_{\text{C}}^i(R)}{\alpha_{\text{NbC}} X_{\text{C}}^{\text{NbC}} - X_{\text{V}}^i(R)} \\ X_{\text{Nb}}^i X_{\text{C}}^i = K_{\text{NbC}} \exp \left[ \frac{R_o}{R} \right] \end{array} \right. \quad (2.33)$$

$$\left\{ \begin{array}{l} \left. \frac{dR}{dt} \right|_{\text{V}} = \frac{D_{\text{V}}}{R} \frac{X_{\text{V}} - X_{\text{V}}^i(R)}{\alpha_{\text{VCN}} X_{\text{V}}^{\text{VCN}} - X_{\text{V}}^i(R)} \\ \left. \frac{dR}{dt} \right|_{\text{C}} = \frac{D_{\text{C}}}{R} \frac{X_{\text{C}} - X_{\text{C}}^i(R)}{\alpha_{\text{VCN}} X_{\text{C}}^{\text{VCN}} - X_{\text{C}}^i(R)} \\ \left. \frac{dR}{dt} \right|_{\text{N}} = \frac{D_{\text{N}}}{R} \frac{X_{\text{N}} - X_{\text{N}}^i(R)}{\alpha_{\text{VCN}} X_{\text{N}}^{\text{VCN}} - X_{\text{N}}^i(R)} \\ X_{\text{V}}^i (X_{\text{C}}^i)^z = \chi K_{\text{VC}_z} \exp \left[ \frac{(1-\chi)^2 \Omega_{\text{CN}}^{\text{V}}}{kT} \right] \exp \left[ \frac{R_o}{R} \right] \\ X_{\text{V}}^i X_{\text{N}}^i = (1-\chi) K_{\text{VN}} \exp \left[ \frac{\chi^2 \Omega_{\text{CN}}^{\text{V}}}{kT} \right] \exp \left[ \frac{R_o}{R} \right] \end{array} \right. \quad (2.34)$$

where  $\alpha_{\text{NbC}}$  and  $\alpha_{\text{VCN}}$  represent the ratio of the mean atomic volume of the austenite over the mean atomic volume of the precipitate.  $X_{\text{Nb}}^{\text{NbC}} = 1/2$  and  $X_{\text{C}}^{\text{NbC}} = 1/2$  for the NbC precipitates, while for the  $\text{VC}_x\text{N}_y$  phase,  $X_{\text{V}}^{\text{VCN}} = 1/(1+x+y)$ ,  $X_{\text{C}}^{\text{VCN}} = x/(1+x+y)$  and  $X_{\text{N}}^{\text{VCN}} = y/(1+x+y)$ .  $D_{\text{Nb}}$ ,  $D_{\text{V}}$ ,  $D_{\text{N}}$  and  $D_{\text{C}}$  are the diffusion coefficients of the niobium, vanadium, carbon and nitrogen respectively. The unknown values of these systems are the interface concentrations,  $\chi$  value and  $dR/dt$  values. Solving these systems gives both the growth rate and the composition of precipitates.

To solve the 2.34 system we used the Newton-Raphson algorithm to calculate numerically the solutions. In our case, we have  $(D_{\text{N}}, D_{\text{C}}) \gg (D_{\text{Nb}}, D_{\text{V}})$  and  $X_j^i \gg X_j^p$  where  $j$  stands for Nb, V, C or N. This leads to the following simplifications:

$$X_{\text{C}}^i = X_{\text{C}} \quad (2.35)$$

$$X_N^i = X_N \quad (2.36)$$

When we obtain the solutions, i.e.  $dR/dt$  and  $\chi$ , we add (or we remove) the shell, and we calculate the new mean chemical composition. This kind of approach has been successfully used for the modelling of the vanadium carbonitride precipitation in austenite [Maugis 05].

During the shrinkage of the  $VC_xN_y$  precipitates, a binary VN precipitate is automatically considered if there is no more carbon within the precipitate. The following equations are then used instead of equation 2.34:

$$\begin{cases} \left. \frac{dR}{dt} \right|_V = \frac{D_V}{R} \frac{X_V - X_V^i(R)}{\alpha_{VN} X_V^{VN} - X_V^i(R)} \\ X_V^i X_N^i = K_{VN} \exp \left[ \frac{R_0}{R} \right] \end{cases} \quad (2.37)$$

In the case where there is no more nitrogen, a binary  $VC_z$  precipitate is considered and the equation 2.34 is replaced by:

$$\begin{cases} \left. \frac{dR}{dt} \right|_V = \frac{D_V}{R} \frac{X_V - X_V^i(R)}{\alpha_{VC_z} X_V^{VC_z} - X_V^i(R)} \\ X_V^i (X_C^i)^z = K_{VC_z} \exp \left[ \frac{R_0}{R} \right] \end{cases} \quad (2.38)$$

Finally, the last stage consists in a mass balance, which allows us to calculate the amount of alloying elements remaining in the solid solution after each step of nucleation and growth/coalescence. Thus, we obtain the atomic fraction  $X_j$  of alloying elements ( $j = Nb, V, C$  or  $N$ ) as a function of the precipitate volume fraction:

$$X_j = \frac{X_j^o - \sum_p X_{j,p} f_p \alpha_p}{1 - \sum_p f_p \alpha_p} \quad (2.39)$$

where  $p = NbC$ , or  $VC_xN_y$ ,  $X_j^o$  is the alloy atomic content and  $f_p$  is the volume fraction of the precipitate  $p$ . In the case of the vanishing of one alloying element in the  $VC_xN_y$  precipitate the mass balance is given by:

$$\begin{cases} X_V^{VC_z} = \frac{1}{1 + z} \\ X_C^{VC_z} = \frac{z}{1 + z} \\ X_N^{VC_z} = 0 \end{cases} \quad (2.40)$$

$$\begin{cases} X_V^{VN} = 0.5 \\ X_C^{VN} = 0 \\ X_N^{VN} = 0.5 \end{cases} \quad (2.41)$$

#### 2.4.2.6 Implementation

Computation is started with a system of size classes describing the precipitation size distribution. This distribution can be either empty<sup>2</sup> or deduced from experiments, for which we want to model the time evolution.

Our model is based on the Lagrange-like approach described in [Perez 08]. This approach is inspired from the “Multi-Préci” model developed by Maugis and Gouné [Maugis 05] and implemented in the PreciSo software developed by D. Acevedo [Acevedo 07]. In this approach, the time evolution of each radius size class is calculated, the class population remaining constant. Then the radius is updated for each existing class by:

$$R(t + \Delta t) = R(t) + \left. \frac{dR}{dt} \right|_{growth} \Delta t \quad (2.42)$$

with  $\left. \frac{dR}{dt} \right|_{growth}$  given by equations 2.33, 2.34, 2.37 and 2.38. More details of this approach are given in [Perez 08].

#### 2.4.2.7 Parameters

In this approach, two simulated distributions obtained from experimental precipitate size distribution are used as input parameters and are described by discrete radius size distributions. The value of  $\chi$  is obtained from EELS analysis on the “Fully precipitated” state and is equal to 0.9.

In his PhD D. Acevedo [Acevedo 07] presented the influence of various input parameters such as the interface energy, the diffusion coefficient, or the solubility product. He highlighted that, during reversion, the interface energy has a small influence that an increase of the vanadium diffusion coefficient speeds up the kinetic, but does not change the thermodynamic equilibrium or the parameters evolution. In these conditions, diffusion coefficient for niobium, vanadium and carbon, as well as the interface energy for NbC are taken from this thesis (i.e. from [Geise 85] for the niobium diffusion coefficient and

---

<sup>2</sup>If nucleation is modelled, which is not the case all along this work.

from [Gladman 97] for the carbon diffusion coefficient). The nitrogen diffusion coefficient comes from [Gladman 97]. The interface energy for  $VC_xN_y$  is that used by [Maugis 05]. The solubility product used in the [Acevedo 07] thesis (and proposed by [Narita 75]) for NbC presents a good agreement with experimental results. For  $VC_xN_y$  precipitates, it is a combination of VN and  $VC_z$  solubility products. To get a better agreement with our experimental results, B factor in the solubility products (i.e.  $\log K_s = -A/T + B$ ) has been slightly changed from data of [Acevedo 07] for  $V_6C_5$  and of [Irvine 67] for VN (4.193 instead of 3.685 for  $V_6C_5$  and 3.859 instead of 3.46 for VN).

Vanadium atomic weight	50.94 g.mol <sup>-1</sup>	
Niobium atomic weight	92.91 g.mol <sup>-1</sup>	
Carbon atomic weight	12.01 g.mol <sup>-1</sup>	
Nitrogen atomic weight	14.01 g.mol <sup>-1</sup>	
Vanadium $D_o$	0.1 10 <sup>-4</sup> m <sup>2</sup> .s <sup>-1</sup>	[Acevedo 07]
Niobium $D_o$	8.3 10 <sup>-5</sup> m <sup>2</sup> .s <sup>-1</sup>	[Geise 85]
Carbon $D_o$	0.1 10 <sup>-4</sup> m <sup>2</sup> .s <sup>-1</sup>	[Gladman 97]
Nitrogen $D_o$	9.1 10 <sup>-5</sup> m <sup>2</sup> .s <sup>-1</sup>	[Gladman 97]
Vanadium activation energy	240000 J.mol <sup>-1</sup>	[Geise 85]
Niobium activation energy	266500 J.mol <sup>-1</sup>	[Acevedo 07]
Carbon activation energy	135700 J.mol <sup>-1</sup>	[Gladman 97]
Nitrogen activation energy	168600 J.mol <sup>-1</sup>	[Gladman 97]
NbC lattice parameter	4.471 10 <sup>-10</sup> m	[Gladman 97]
$VC_xN_y$ lattice parameter	4.159 10 <sup>-10</sup> m	
NbC interface energy	0.5 J.m <sup>2</sup>	[Acevedo 07]
$VC_xN_y$ interface energy	0.5 J.m <sup>2</sup>	[Maugis 05]
$\log(Ks)$ NbC (in atomic %)	-7900/T(K) + 3.42	[Narita 75]
$\log(Ks)$ VC (in atomic %)	-5531/T(K) + 4.193	[Acevedo 07] <sup>1</sup>
$\log(Ks)$ VN (in atomic %)	-8330/T(K) + 3.859	[Irvine 67] <sup>1</sup>
Interaction parameter $\Omega_{CN}^V$	20000 J.mol <sup>-1</sup>	[Frisk 08]

Table 2.6: *Physical and thermodynamical parameters used for the reversion simulation in the alloy FeVNbCN.*

The lattice parameter of  $VC_xN_y$  can be evaluated by a simple mixture law such as:

$$a_{VCN} = \chi a_{VC} + (1 - \chi) a_{VN} \quad (2.43)$$

Here  $\chi$  is obtained from EELS analysis performed on the “Fully precipitated” state ( $\chi = 0.9$ ) and is considered constant. An interaction parameter

<sup>1</sup>See text

$\Omega_{\text{CN}}^{\text{V}}$  of carbon and nitrogen in vanadium is necessary, and we choose to use that proposed by [Frisk 08] (based on [Kieffer 70] results).

#### 2.4.2.8 Comparison with experimental results

In this paragraph, experimental results obtained from the FeVNbCN model alloy will be compared with the model predictions. The table 2.7 presents a summary of experimental techniques performed on all states of the FeVNbCN model alloy.

Time	FPS	2 min	20 min	200 min	2000 min
900°C	R: HAADF f: ICP V,Nb: EDX C/N: EELS	R: HAADF V,Nb: EDX	R: HAADF f: ICP V,Nb: EDX	R: HAADF f: ICP V,Nb: EDX C/N: EELS	R: HAADF V,Nb: EDX
1050°C	R: HAADF f: ICP V,Nb: EDX C/N: EELS	R: HAADF f: ICP V,Nb: EDX C/N: EELS	R: HAADF f: ICP V,Nb: EDX	R: HAADF f: ICP V,Nb: EDX	

Table 2.7: Summary of all experimental techniques. FPS means Fully Precipitated State

The initial precipitate size distributions used for the model are obtained from experimental measurement on HAADF micrographs. Precipitates are then arranged in size classes and distributions are normalized in order to get the correct precipitate volume fraction  $f_v$ :

$$f_v = \frac{4}{3}\pi \sum N_n R^3 \Delta R \quad (2.44)$$

where  $N_n$  is the number density. Figure 2.24 presents initial distributions of NbC and  $\text{VC}_x\text{N}_y$  used for the model. Finally, the experimental precipitate size distributions are fitted by a Log-normal law.

Figure 2.25 presents the comparison between experimental results and prediction of the model for the volume fraction evolution during reversion at 900°C and 1050°C.

There is no significative evolution of NbC volume fraction at 900°C. At 900°C the model kinetics are slower than what we experimentally observe for  $\text{VC}_x\text{N}_y$  precipitates. The model predicts a total vanadium solutionnizing

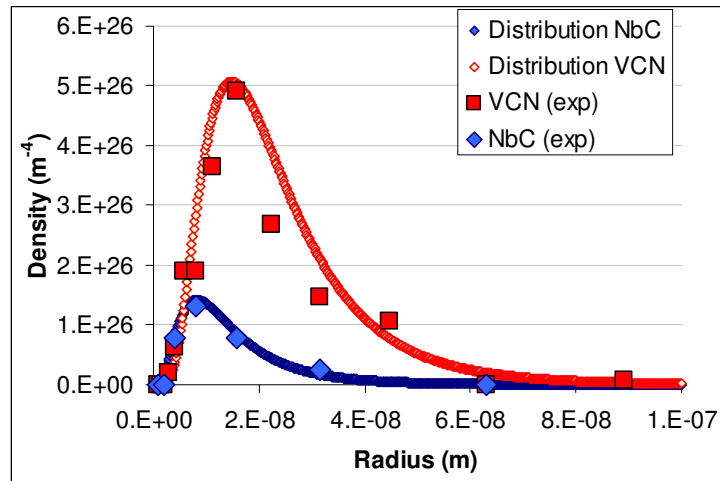


Figure 2.24: Initial precipitate size distributions of NbC and  $VC_xN_y$  used for the model. These distributions are normalized in order to obtain the correct volume fraction.

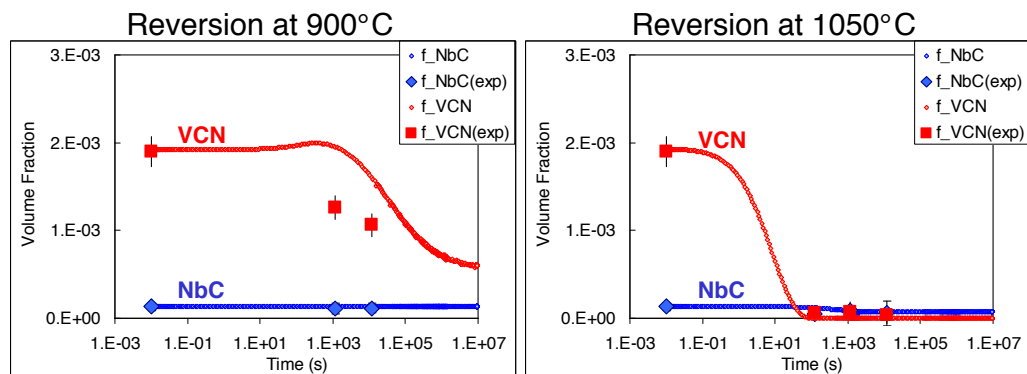


Figure 2.25: Model prediction for the volume fraction evolution during reversion at  $900^\circ\text{C}$  and  $1050^\circ\text{C}$ . Experimental results are shown for  $VC_xN_y$  and NbC precipitates.

at  $1050^\circ\text{C}$ , while experimental results show that some vanadium remains in precipitates.

Figure 2.26 presents experimental results and the model prediction for the precipitate size evolution during reversions at  $900^\circ\text{C}$  and at  $1050^\circ\text{C}$  for both precipitate types.

Predictions for the mean radius evolution for NbC and  $VC_xN_y$  are very similar at  $900^\circ\text{C}$ . The mean radius rises to reach a coarsening regime. Predic-

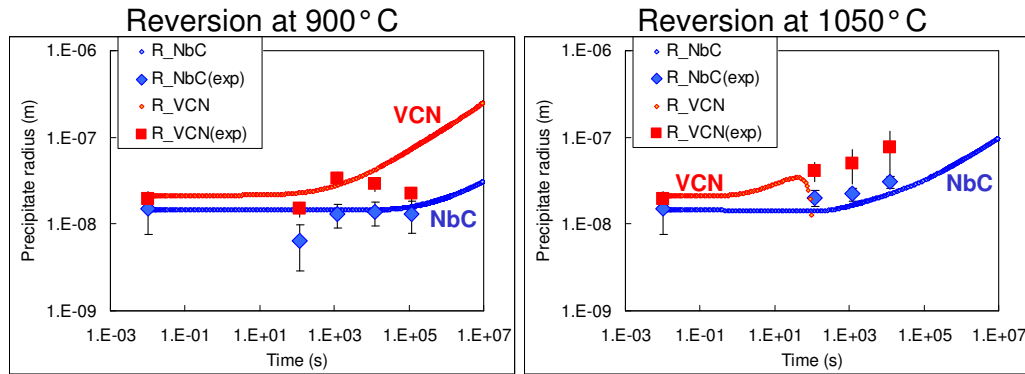


Figure 2.26: Model prediction for the mean radius evolution during reversion at  $900^{\circ}\text{C}$  and  $1050^{\circ}\text{C}$ . Experimental results are shown on the figure for  $\text{VC}_x\text{N}_y$  and  $\text{NbC}$  precipitates.

tions obtained with the model present a good agreement with experimental results for both  $\text{NbC}$  and  $\text{VC}_x\text{N}_y$  mean radius. At  $1050^{\circ}\text{C}$  predictions of the model and experimental results for  $\text{NbC}$  are in good agreement and present a similar behavior than at  $900^{\circ}\text{C}$ . As  $\text{VC}_x\text{N}_y$  are totally solutionnized, the model could not give their mean radii after nearly 100 s.

Finally, this model allows us to compare the chemical evolution of the vanadium carbonitrides. Figure 2.27 presents the model prediction for the chemical composition of the  $\text{VC}_x\text{N}_y$  for reversion at  $900^{\circ}\text{C}$ , and experimental results obtained by EELS analysis on this state. There is a good agreement between experimental results and model prediction and the model predicts an enrichment in nitrogen for long treatment times. This may be due to the selective solution of carbon. This behaviour has been previously observed with the temperature increasing [Crooks 81], [Courtois 05]). The evolution of the precipitate composition at  $1050^{\circ}\text{C}$  since all  $\text{VC}_x\text{N}_y$  precipitates are dissolved after 100s.

Figure 2.28 presents the model prediction for the volume fraction evolution of  $\text{VC}_z$ ,  $\text{VN}$  and  $\text{VC}_x\text{N}_y$  at  $900^{\circ}\text{C}$  and  $1050^{\circ}\text{C}$ .  $\text{VN}$  precipitates are much stable than  $\text{VC}_x\text{N}_y$  and  $\text{VC}_z$  precipitates for both temperatures. The model shows that adding nitrogen will stabilized the precipitate for high temperature.

All these results coming out from the model confirm that the presence of nitrogen has a stabilizing effect on the  $\text{VC}_x\text{N}_y$  particles. The discrepancy observed at  $900^{\circ}\text{C}$  (that is, the predicted dissolution kinetic is slower than the observed one) could be corrected by considering a sub-stoichiometric  $\text{VN}_{1-\epsilon}$

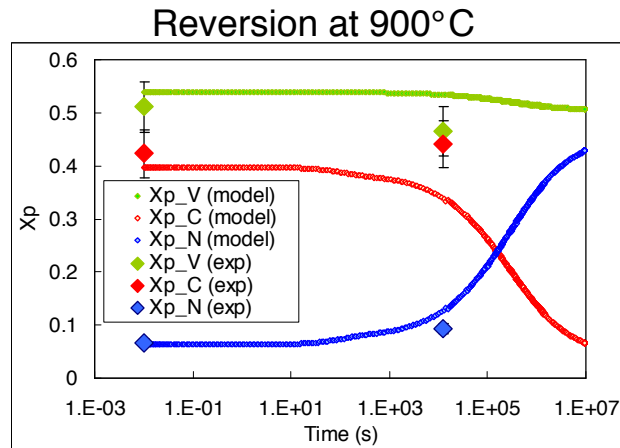


Figure 2.27: Model prediction for the  $VC_xN_y$  composition evolution during reversion at  $900^\circ$ . Experimental results obtain by EELS are shown on the figure.

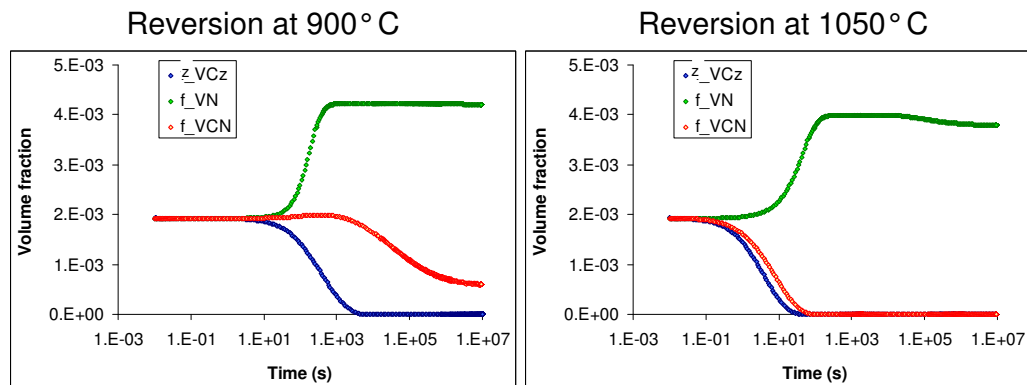


Figure 2.28: Model prediction for  $VC_z$ ,  $VN$  and  $VC_xN_y$  volume fraction evolution during reversion at  $900^\circ$  and  $1050^\circ$  C.

component in the ideal solution introduced in equation 2.7. Furthermore, the experimental study shows that precipitates (and in particular V-rich precipitates) are not totally pure. Indeed vanadium carbonitrides contain nearly 10% of niobium. Hence, it would be necessary to model mixed  $(V,Nb)(C,N)$  instead of  $V(C,N)$  precipitates. The addition of niobium could stabilize the VCN precipitates.

## 2.5 Conclusion

In this chapter, we have studied the nitrogen influence on the precipitation state. Many scientific papers studied the precipitation state evolution in steels containing nitrogen, however, they do not consider the chemical composition of the particles. Here, we used the EELS to quantify the nitrogen and the carbon in precipitates in order to precisely characterize the precipitation state. The principal conclusions are the following:

- There are essentially two precipitate kinds, Nb-rich and V-rich categories.
- EELS analysis shows that V-rich precipitates are carbonitrides while Nb-rich are carbides.
- Vanadium carbonitrides are solutionized during reversion treatment for temperatures higher than 900°C.
- We observe an increase of niobium particles ratio with the increase of the treatment duration or with the temperature. This increase is probably due to the solutionizing of V-rich particles, giving the impression that the number of Nb-rich particles increases.
- A precipitation model, based on the evolution of two populations of precipitates ( $\text{NbC}$  and  $\text{VC}_x\text{N}_y$  phases) has been presented. It exhibits a fairly good agreement with experimental results for both reversion at 900°C and 1050°C. At 900°C, the model kinetics are slightly slower than what is experimentally observed.
- This model further shows that adding nitrogen stabilizes precipitates at high temperature.

## CHAPTER 3

# Correlation between the precipitation state and grain growth

Thermo-mechanical treatments are commonly performed on industrial steels used in gearing such as the 16MnCr5 industrial grade. In particular an isothermal annealing and a carburizing treatment are generally performed, during which the Prior Austenitic Grain Size (PAGS) evolves and may lead to a degradation of the mechanical properties of steel. Thus, it is important to restrict the austenitic grain growth by introducing microalloying elements in order to form carbonitrides with the aim to pin the grain boundaries.

In bulk material, the growth of austenitic grains is governed by a decrease of the total interface energy. The grain boundaries energy depends on grains misorientation [Martin 97] and the mobility of these grain boundaries is inversely proportional to the misorientation ([Humphreys 95] according to [Weygand 98]). The introduction of microalloying elements leads to the formation of precipitates, which may pin austenitic grain boundaries and thus control the grain growth.

Three steps of austenitic grain growth are highlighted during reversion treatments [Cuddy 83], [Gao 98]. Figure 3.1 presents the PAGS evolution versus time during reversion treatments. No growth occurs during the first step when all grain boundaries are pinned by precipitates. Then, with an increase of temperature or time, some precipitates are solutionized leading to a decrease of the precipitation pinning force. Consequently some grains may grow faster than the others: this phenomenon is the so-called Abnormal Grain Growth (AGG) regime. The growth of the austenitic grain size during the AGG regime is fed by the disappearance of small grains. Finally, the pinning force continues to decrease with the increasing of temperature and time, leading to the Normal Grain Growth (NGG) regime [Gladman 97].

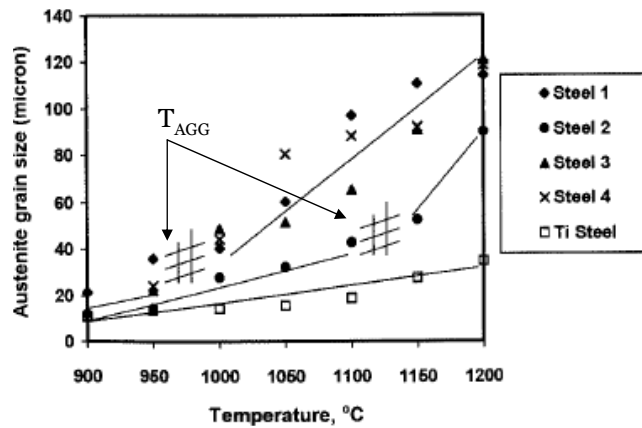


Figure 3.1: Mean austenitic grain size evolution with the increase of austenitizing temperature for Al-V-N and Al-V-Ti-N microalloyed steels. The curve highlights three steps during the growth: the zero growth, the abnormal grain growth and the normal grain growth.  $T_{AGG}$  represents the transition temperature zero growth/abnormal grain growth [Gao 98].

Figure 3.2 presents two optical micrographs of the PAGS microstructure on a microalloyed steel. On figure 3.2.a we can see a normal grain growth (or no growth) structure, while figure 3.2.b shows an AGG structure with the growth of some large grains at the expense of small grains.

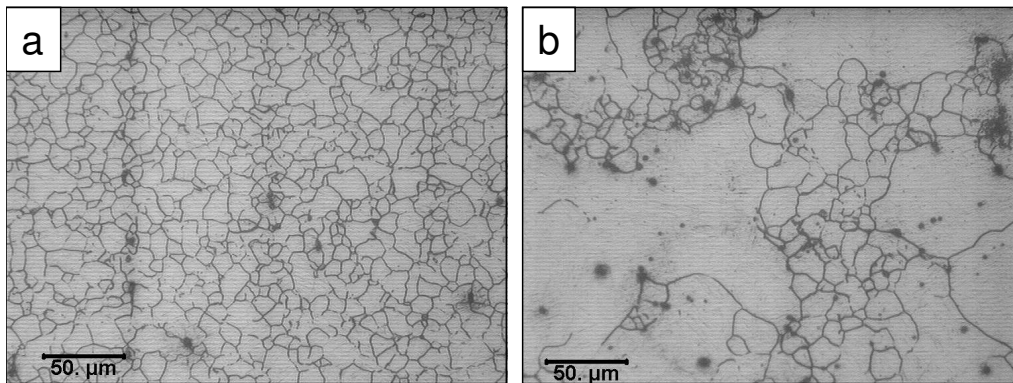


Figure 3.2: Optical micrographies of a microalloying steel after a Bechet-Beaujard etching. a) Normal grain growth or zero growth microstructure with an homogeneous grain size; b) AGG microstructure.

Many studies concerned the austenitic grain growth in presence of precipitates. All of them show that an addition of microalloying elements tends to control the PAGS, i.e. to increase the temperature at which AGG may

occur [Stasko 06], [Fernandez 07], [Gao 98], [Medina 99], [Padilha 99]. However, only few papers present a quantitative connection between detailed studies of the precipitation state and of the austenitic grain size. Moon *et al.* [Moon 07b] [Moon 07a] present a quantitative model that predicts the limiting austenite grain size of a Ti-microalloyed steel in the presence of growing particles, with a volume fraction and a size, which may vary. Likewise, Manohar *et al.* [Manohar 96] propose a mathematical model, which predicts the equilibrium grain size for a given precipitation state. Those model present a good agreement with the experimental results, however they do not take into account the grain boundaries mobility. Taking into account this mobility enables to compare the predictions of the models with experimental PAGS, which does not reach the equilibrium (e.g. for short heat treatments).

The aim of this chapter is to study the correlation between the PAGS and the precipitation state evolution in the 16MnCr5+Nb industrial steel to understand what happens during thermo-mechanical treatments. Indeed, a carburizing treatment is performed on this alloy, during which the PAGS evolves. Then, the PAGS of the FeVNbCN model alloy will be characterized to understand and to predict its evolution in presence of a precipitate phase during reversion treatments. First, a qualitative study of the correlation will be presented, then a quantitative study will be proposed with the implementation of a model.

### 3.1 Materials and treatments

First, the chemical composition and heat treatments of the 16MnCr5+Nb industrial steel will be presented and then, a brief reminder of the FeVNbCN model alloy chemical composition and heat treatments will be given.

#### 3.1.1 16MnCr5+Nb industrial steel steel

##### 3.1.1.1 Chemical composition and industrial process for gears

The chemical composition of the 16MnCr5+Nb steel grade studied here proceed from the composition of the French standard NF EN 10084. This steel present a microalloying in aluminium and niobium. Table 3.1 presents its chemical composition.

Figure 3.3 presents the industrial thermomechanical treatment performed on the 16MnCr5+Nb microalloy. It is composed by four important stages: the

	C	Si	Mn	Ni	Cr	Al	Nb	N
wt.%	0.208	0.178	1.207	0.140	1.146	0.034	0.037	0.00234

Table 3.1: Chemical composition of the 16MnCr5+Nb industrial steel. Values are given in weight %

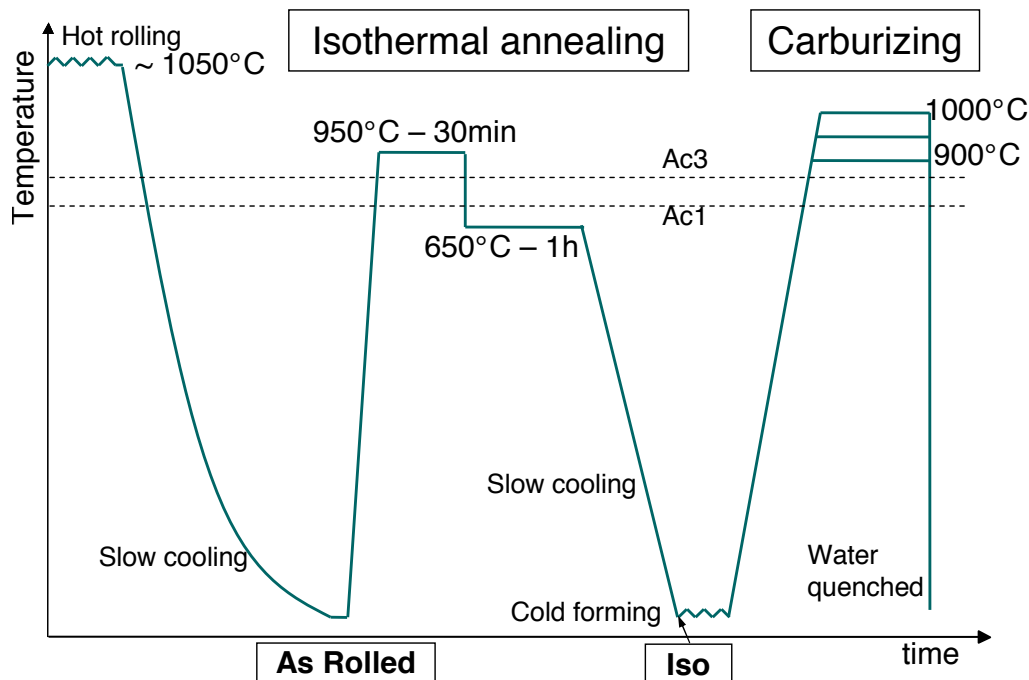


Figure 3.3: Industrial thermomechanical treatment performed on the 16MnCr5+Nb steel. After hot forming, an isothermal annealing followed by a cold forming is performed on the steel. This industrial treatment is finished by a carburizing treatment.

hot forming, the isothermal annealing, the cold forming and the carburizing treatment:

- The hot forming is performed at a temperature higher than 1050°C. It is followed by a slow cooling in air leading to a bainitic microstructure. During this cooling the carbonitrides precipitation is possible. These precipitates will have an important role for the austenitic grain. The state obtain is called “As Rolled”.
- An isothermal annealing is then performed on the *As Rolled* state over the Ac3 temperature followed by a cooling until the perlitic nose and a maintaining at this temperature during 1 hour. The steel is then cooled in air. This treatment promotes a regular repartition of ferrite and fine

lamellar perlite, which leads to a relatively ductile structure. This state will be called *Iso* state for the following.

- This treatment can be followed by a cold forming allowing to obtain very good surface conditions. This is beneficial in the case of the forming of complex shape pieces, such as gears, because it allows to limit the finishing subsequent operations.
- To finish, a carburizing treatment is performed at temperature within 900°C and 1000°C. This treatment leads to a high surface hardness but also provides a good fatigue resistance. It is during this treatment that the precipitation state plays an important role: carbonitrides can pin austenitic grain boundaries and thus control the austenitic grain growth.

### 3.1.1.2 Heat treatments

Two initial states (*As Rolled* and *Iso*) were used in order to study the influence of precipitate volume fraction and precipitate size on the grain size. Then, to monitor the PAGS evolution during the carburizing, reversion treatments have been performed on these two initial states.

Thus, from the *As Rolled* and *Iso* states, several reversion treatments were realized at temperature ranging from 900°C to 1100°C during 2 minutes to 20 hours. The “900°C-2 minutes” states will be considered as the “initial state” in terms of austenitic grain size. The temperature ramp rates are relatively prompt (3 or 4°C/s). Reversion treatments are performed on small samples. For both *As Rolled* and *Iso* states, the alloy is cut in 5 mm thick disks, which are then further cut to obtain 5 mm × 5 mm × 45 mm samples (see figure 3.5). All treatments are performed in quartz capsules under vacuum to avoid decarburizing. The quench is done by breaking the capsule in water. These treatments are presented on figure 3.4.

### 3.1.2 FeVNbCN model alloy

In this paragraph, we quickly recall the chemical composition and heat treatments carried out on the FeVNbCN model alloy. Table 3.2 shows its chemical composition.

To ensure complete dissolution of precipitates the FeVNbCN alloy was maintained at 1280°C for 30 minutes in argon then water quenched. Then, in order to achieve a “fully-precipitated state”, this steel has been treated during 10 hours at 700°C followed by 10 days at 800°C and water quenched. To

### Chapter 3. Correlation between the precipitation state and grain growth

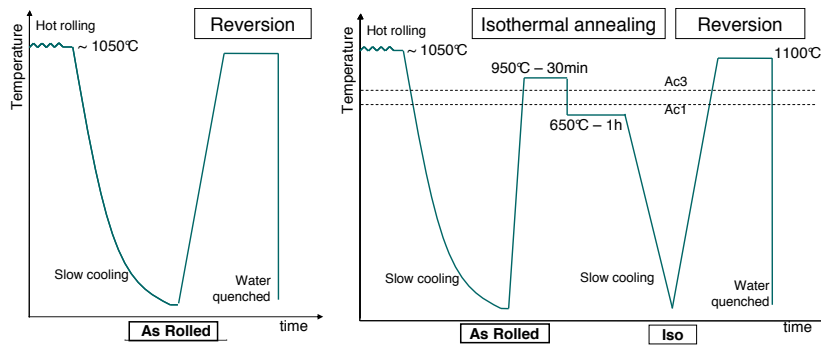


Figure 3.4: Heat treatments performed on the 16MnCr5+Nb steel. Treatments on the Iso state are performed without the cold forming.

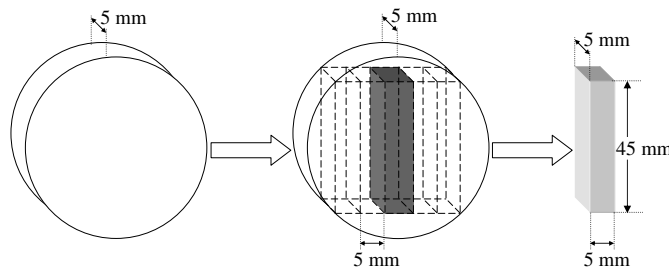


Figure 3.5: Samples preparation of the 16MnCr5+Nb alloy. Grey parts are removed to avoid decarburized and segregated areas.

	C	Si	Mn	S	Ni	Cr
wt.%	0.48	0.028	0.088	0.017	0.023	0.049
at.%	2.2	0.055	0.088	0.029	0.021	0.052
	Mo	Ti	Nb	V	N	
wt.%	0.007	0.001	0.012	0.202	0.0063	
at.%	0.004	0.0011	0.0071	0.217	0.025	

Table 3.2: Chemical composition of the FeVNbCN steel (in wt.% and at.%)

investigate a wide range of precipitation states and grain sizes, the alloy was subjected to different isothermal reversion treatments in the austenitic domain at temperatures ranging from 900°C to 1050°C and for 2 to 2000 minutes, followed by a water quench. All these treatments were performed under vacuum in quartz capsules (see figure 3.6).

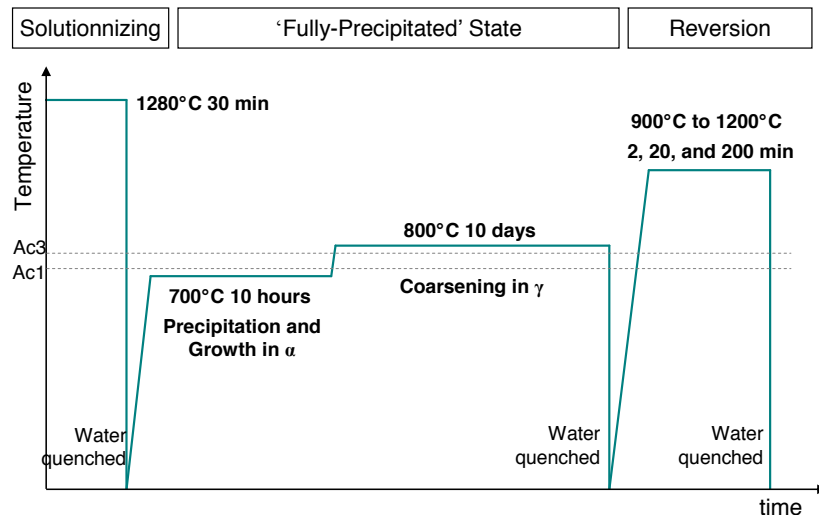


Figure 3.6: Heat treatments for the FeVNbCN alloy.

## 3.2 Experimental techniques

### 3.2.1 Characterization of the precipitation state

The characterization of the precipitation state is performed as in chapter 2. TEM observations of precipitates were performed on aluminium or carbon extraction replicas. The preparation of these replicas is given in Appendix A. Electron microscopy was performed using a JEOL 2010F field emission gun transmission electron microscope operating at 200 kV. The microscope is fitted with a JEOL annular detector allowing High Angle Annular Dark Field (HAADF) imaging in the scanning mode (STEM). The Precipitate distribution size is obtained using a software developed by T. Epicier on HAADF micrographs. Sizes are calculated from the area of the closest ellipse used to approach the particle areas. Precipitate volume fraction is obtained using the electrolytic dissolution technique. Details of this method are given in Appendix B.

### 3.2.2 Characterization of the Prior Austenite Grain Size

PAGS is obtained using a chemical etching called “Bechet-Beaujard” (picric acid + HCl+ Teepol) heated at 50°C on surface polished to 1  $\mu\text{m}$ . Bechet-Beaujard etching is commonly used in austenitic grain growth study [Stasko 06] [Fernandez 07] and in the industry. This etching reveals the prior austenitic grain boundaries by targeting the impurities localized in these grain boundaries.

Figure 3.7 presents the imaging processing performed on optical micrographs. First, a manual tracing of these micrographs is performed and then it is digitized and thresholded (figure 3.7.a). Then we apply a skeletonize procedure (figure 3.7.b) followed by an dilatation (figure 3.7.c) to fill the potential holes. the last stage consists in applying an erosion to obtain very thin grain boundaries and then to reverse the color (figure 3.7.d) in order to treat more easily the tracing with the ImageTool software, and to calculate the "equivalent" diameter of each grain. The diameter is obtained from a circle with the same area as the grain. Only completely closed grains are taken into account in this treatment, open grains (with a discontinuous outline) or interfering with the image border (in red on figure 3.7.d) are not considered. About 200 austenitic grains are counted for each state from optical micrographs. It is therefore important to consider an important number of random areas.

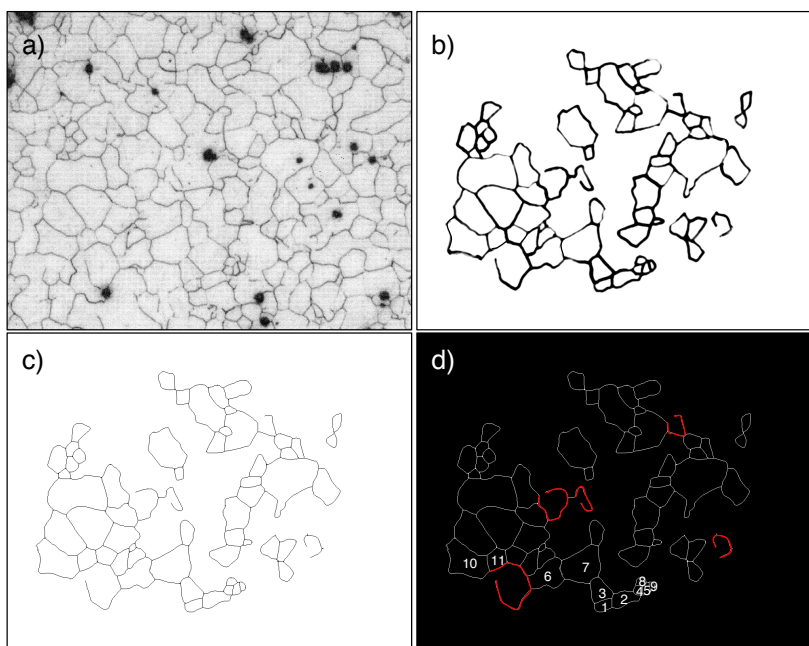


Figure 3.7: Example of a tracing treatment to obtain the grain size distribution. a) Optical micrograph; b) Digitized and thresholded tracing of the micrograph a); c) Skeletonizing of the tracing; d) Colour are reversed to use the ImageTool software. Grain in red, which are not closed, are not counted.

### 3.3 Experimental results

Experimental results of the 16MnCr5+Nb steel grade and the FeVNbCN model alloy are discussed in this part. First, results obtained for the PAGS will be exposed, and then the precipitation state study will be presented. Finally, the correlation between the grain size and precipitation state evolution will be discussed.

#### 3.3.1 Austenitic grain size of the 16MnCr5+Nb

Bechet-Beaujard etching have been performed on all samples. Table 3.3 presents the austenitic mean radius for treatments of 1 hour at 900°C, 1000°C and 1100°C for the *As Rolled* and *Iso* states. Optical micrographs observations and values of the table show that there is no significant grain growth for temperatures lower than 1000°C and treatment durations shorter than 1 hour; and this, for both the *As Rolled* or the *Iso* state.

Temperature	Time	Diameter for <i>As Rolled</i>	Diameter for <i>Iso</i> state
900°C	2 min	6.8 μm	6.0 μm
	1h	6.6 μm	5.4 μm
1000°C	1h	7.4 μm	5.0 μm
1100°C	1h	19.1 μm	8.9 μm

Table 3.3: Austenitic grain mean diameter obtained on the *As Rolled* and *Iso* states after treatments of 2 minutes at 900°C and of 1 hour at 900°C, 1000°C and 1100°C.

Figure 3.8 presents optical micrographs of the *As Rolled* and *Iso* states for a treatment of 1 hour at 1100°C. The *As Rolled* state micrograph shows an abnormal growth while the *Iso* state micrograph does not show any significant grain size evolution.

Figure 3.9 presents the PAGS distributions for all investigated states and treatments. In order to have a good visualization of the type of growth (abnormal vs normal) these distributions are expressed “in volume density” ( $NR^3$ ) instead of number density ( $N$ ) (i.e. volume density ( $NR^3$ ) representation gives more weight to large abnormal grains, that would not appear in “classical” number density representation). With this representation, a distribution exhibiting important proportion of large grains is the signature of AGG, whereas a narrow gaussian-like distribution is related to normal grain growth (an example of the interest of this method is given in figure 3.10).

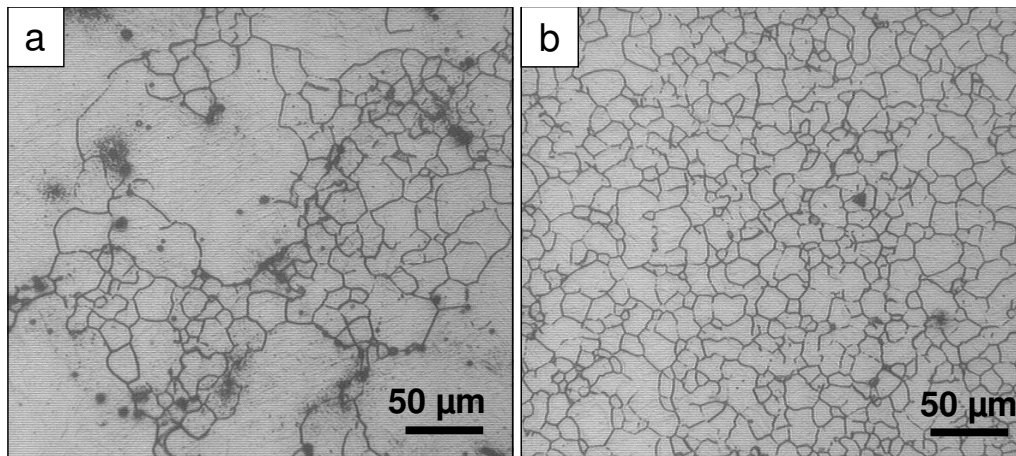


Figure 3.8: Micrographies of the  $16\text{MnCr}_5+\text{Nb}$  alloy after a treatment of 1 hour at  $1100^\circ\text{C}$  for a) *As Rolled* state and b) *Iso* state. We observe an abnormal grain growth in the case of the *As Rolled* state but not for the *Iso* state. Thus we have a better grain growth control for the *Iso* state. Note that initial grain sizes ( $900^\circ\text{C}$  - 2 minutes) are similar for both *As Rolled* and *Iso* states.

For both *As Rolled* and *Iso* states, initial grain size distributions are similar (see figures 3.9.a and b), and no evolution occurs at temperatures lower than  $1100^\circ\text{C}$  (figures 3.9.c to f). For the treatment of 1 hours at  $1100^\circ\text{C}$ , two kinds of distributions were observed: the *As Rolled* state (figure 3.9.g) presents an abnormal grain growth, while the *Iso* state (figure 3.9.h) shows a normal grain growth.

Figure 3.11 presents the grain size distribution for long treatment durations. For all treatments, the *Iso* state exhibits smaller prior austenite grains than the *As Rolled* state. Indeed, there is almost no grain growth for the *Iso* state, except after 10 hours at  $1100^\circ\text{C}$ , where AGG occurs. The *As Rolled* state exhibits AGG for all long duration treatments.

Information given in the literature [Flores 97] [Zavaleta-Gutierrez 07] predicts an influence of the precipitation state on the control of austenitic grain growth. Thus, we can suppose that the *As Rolled* precipitation state is different from that of *Iso* state. Fine characterization of precipitation states present in *Iso* and *As Rolled* states will be presented in section 3.3.3.1.

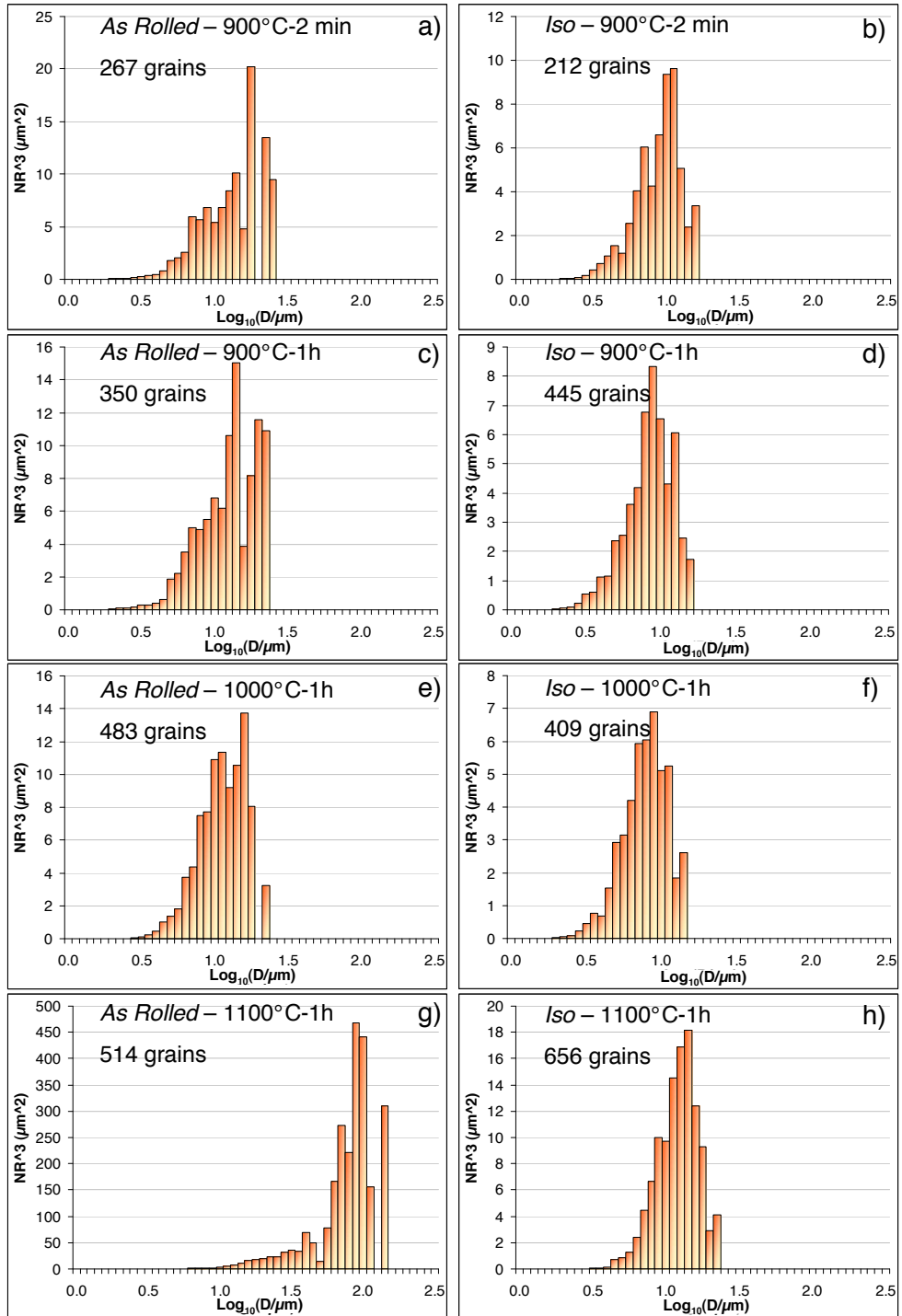


Figure 3.9: Grain size distributions of all reversion treatments. There no evolution for the Iso state, where as we observe an abnormal grain growth for the treatment of 1 hour at 1100°C performed on the As Rolled state.

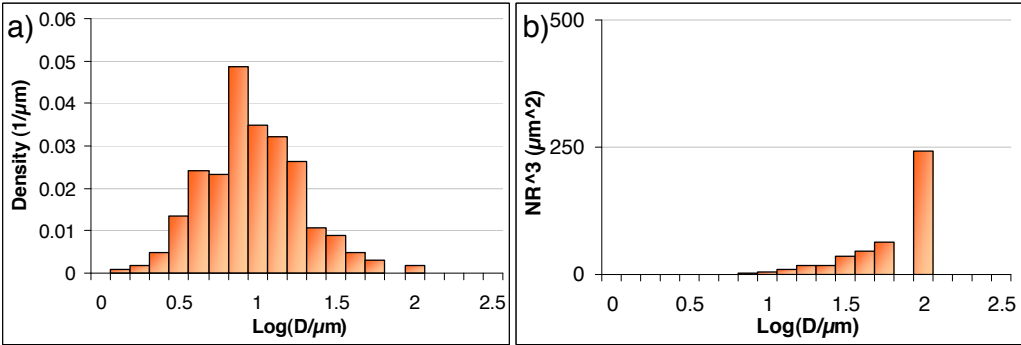


Figure 3.10: a) Number density and b) grain volume density of a same state. With the grain volume density, we clearly observe the presence of small and large grains, while the number density presents Log-normal distribution.

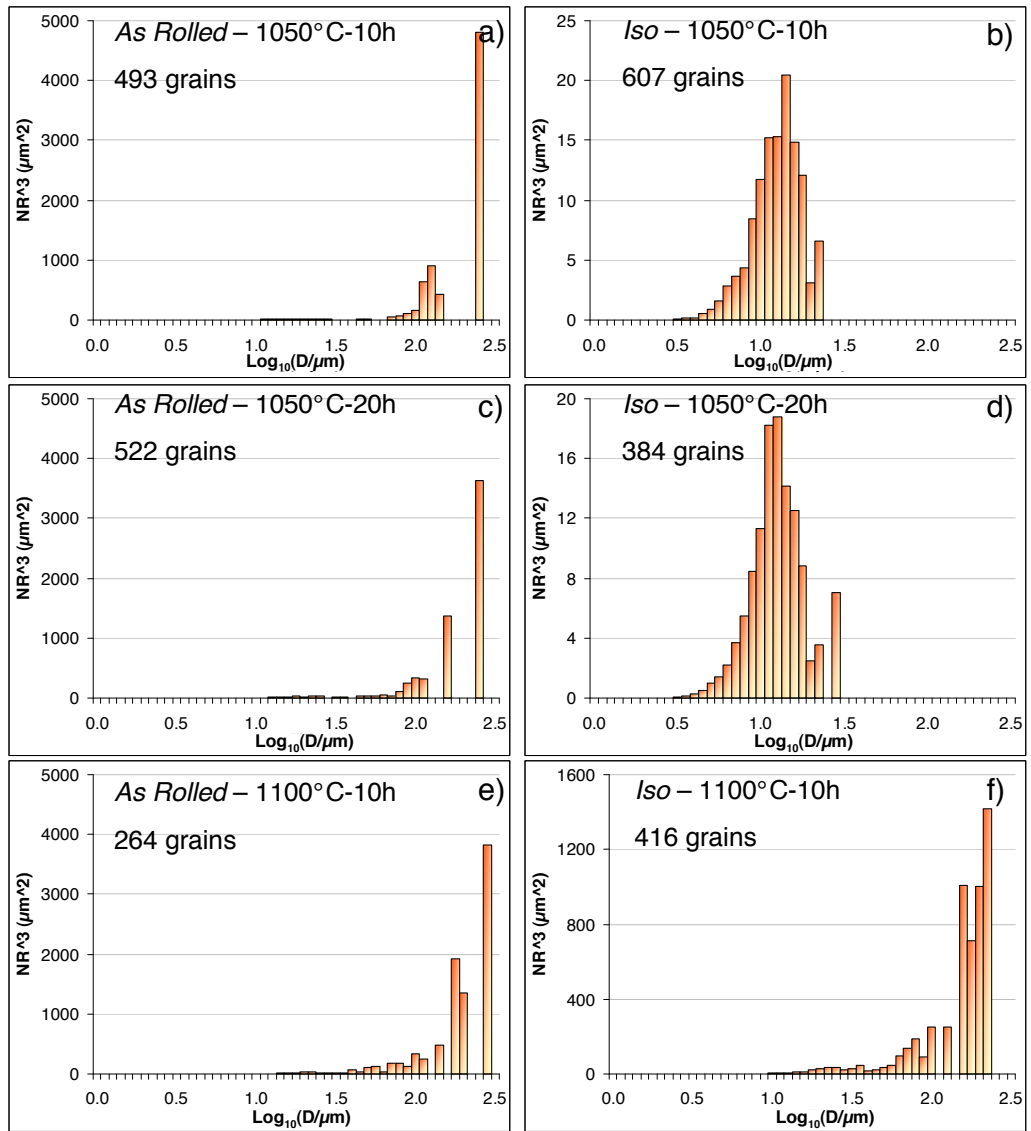


Figure 3.11: Grain size distributions for long heat treatments.

### 3.3.2 Austenitic grain size of the FeVNbCN microalloyed steel

Bechet-Beaujard etching is more difficult to realize on a model alloy since the material is intrinsically relatively “clean” and there is thus only few impurities located at the prior austenitic grain boundaries. Thus, optical micrographs obtained for the FeVNbCN after this etching are not as demonstrative as that of the industrial alloy. Hence, due to the bad quality of these micrographs, prior austenite grains are difficult to visualize, and only few grains are consequently taken into account for the grain size distributions.

Nevertheless, optical micrographs of the FeVNbCN steel after a Bechet-Beaujard etching show an evolution of the austenitic grain size during different reversion treatments. Figure 3.12 presents the austenitic grain size obtain after all treatments. There is no evolution of the mean austenitic grain size at 900°C, whereas we observe an increase of the diameter for treatment temperatures higher than 1050°C. Micrographs from figure 3.13 presents this evolution. Indeed, we observe an homogeneous grain size for all treatments at 900°C, whereas at 1050°C we observe abnormal grain growth even at 2 minutes. These results are confirmed by austenitic grain size distributions presented on figure 3.14.

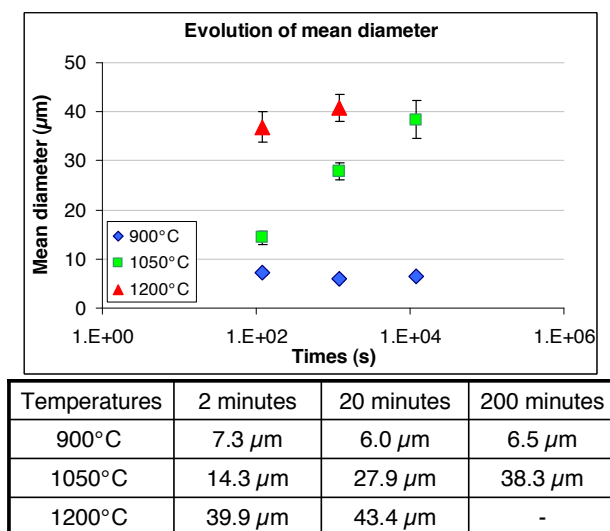


Figure 3.12: Mean grain diameter for all heat treatments. There is no significant difference at 900°C whereas we observe an increase of the mean grain diameter at 1050°C and 1200°C due to the presence of abnormal large grains, that can be seen on figure 3.13.

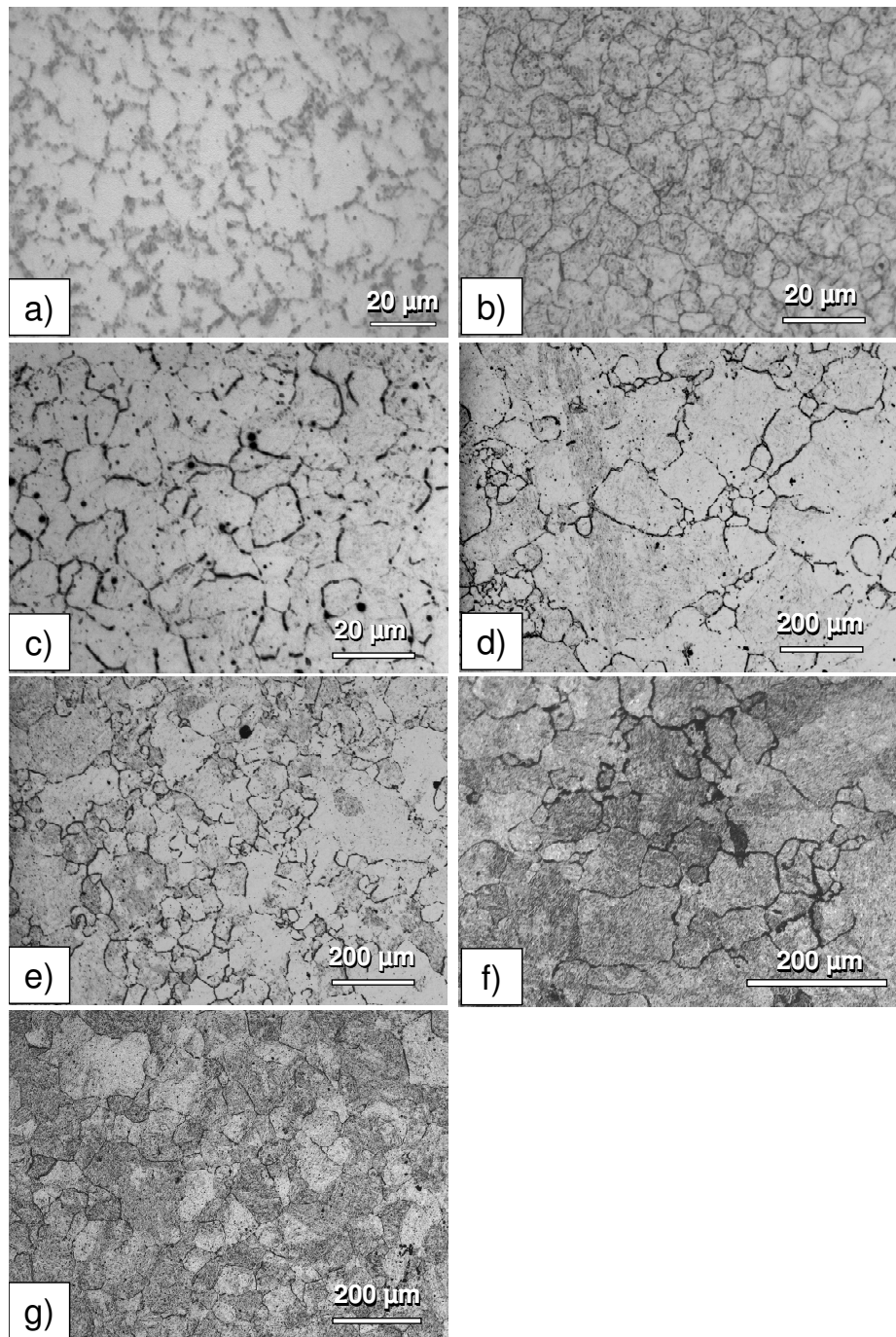


Figure 3.13: Optical micrographies obtained on the FeVNbCN alloy after Bechet-Beaujard etching for various reversion treatments: a) 900°C - 2 minutes; b) 900°C - 20 minutes; c) 900°C - 200 minutes; d) 1050°C - 2 minutes; e) 1050°C - 20 minutes; f) 1050°C - 200 minutes; g) 1200°C - 2 minutes

Chapter 3. Correlation between the precipitation state and grain growth

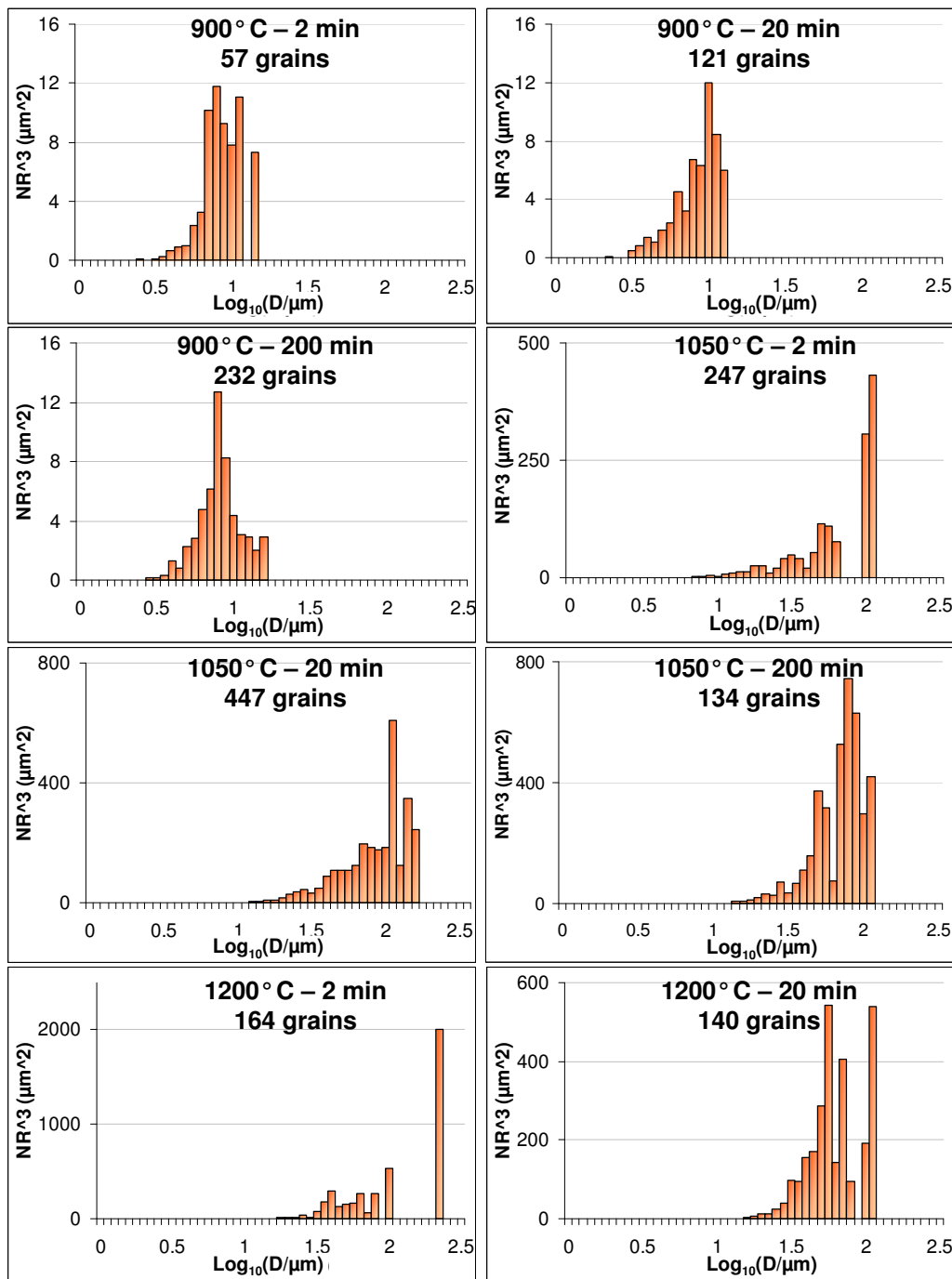


Figure 3.14: Grain size distribution for all heat treatments. AGG regime starts to be observed after 2 minutes at 1050°C.

### 3.3.3 Precipitation state characterization

The experimental study of the precipitation state characterization is necessary to investigate the correlation between the precipitation state and the grain growth evolution. Precipitate (i) chemical composition, (ii) volume fraction and (iii) radii will be presented. Results obtained for the 16MnCr5+Nb microalloyed steel will be detailed and those of the FeVNbCN model alloy will be recalled.

#### 3.3.3.1 16MnCr5+Nb precipitation state

##### 3.3.3.1.1 Precipitate chemical composition

TEM observations have been performed to obtain the precipitate chemical composition and their size distribution. In order to determine the quantity of aluminium in precipitates, it was necessary to realize these observations on carbon replicas instead of aluminium replicas, as performed for the FeVNbCN microalloyed steel in chapter 2.

Figure 3.15 presents STEM-HAADF micrographs of different investigated states. All states show that two precipitate types co-exists: Nb-rich and Al-rich precipitates. For all states, we notice that niobium precipitates frequently observed on aluminium particles. This phenomenon was observed in particular by Leap and Brown [Leap 02] during the study of the duplex precipitate AlN-Nb(C,N) in a 0.2wt% carbon steel. Aluminium is sometimes detected in niobium rich precipitates, but this can be attributed to a superposition effect.

Figure 3.16 presents the ternary diagrams of the precipitate chemical composition for different states of the 16MnCr5+Nb microalloyed steel. This representation allows to locate each particle according to its composition. For the *As Rolled* and *Iso* states we have effectively two precipitate types, the Al-rich and the Nb-rich. A great attention was paid during the observation to identify superimposed particles; red symbols (circles) represent those superimposed particles, Nb-rich on Al-rich precipitates (and vice-versa). It is clear that this population describes almost totally all objects with a mixed (Al,Nb) composition. Moreover, in the *As Rolled* state, we observe that only Nb-rich particles contained titanium. Figure 3.15.a shows a core-shell precipitate type, with a titanium rich core (probably TiN). Hence, it seems that Al-rich and TiN particles may serve as nucleation site for Nb-rich precipitates. For *As Rolled* and *Iso* state treated at 1100°C during 1 hour, we observe more “mixed” precipitates due to superposition effects. Moreover, it seems that the titanium content in Nb-rich precipitates in initial states decreases after a treatment at

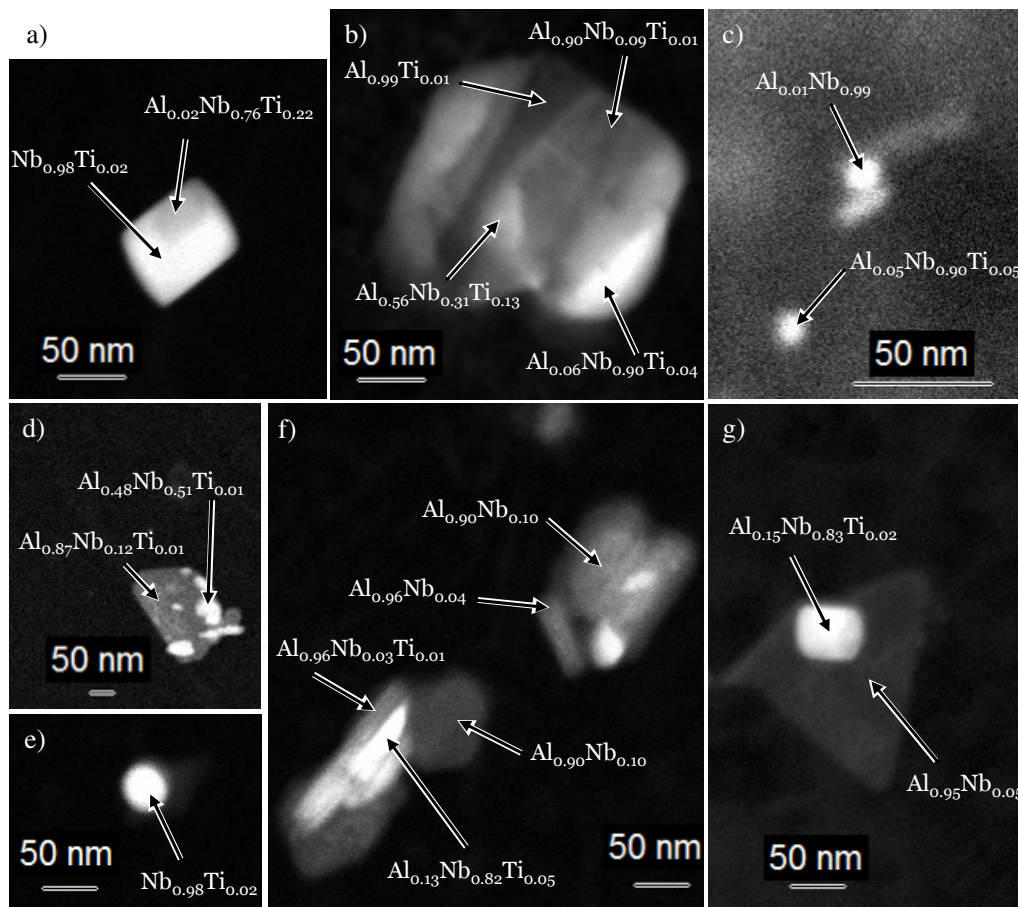


Figure 3.15: *STEM-HAADF micrographs of precipitates extracted from the 16MnCr5+Nb alloy on carbon replicas : a) As Rolled state; b) As a); c) Iso state; d) As c); e) Iso state + 1100°C; f) As e); g) As Rolled state + 1100°C. Chemical compositions written on micrographs is obtained by EDX.*

1100°C.

The precipitate chemistry is obtained by EDX. However it appeared important to confirm by EELS the non-metallic content of the Nb-rich and Al-rich precipitates. Figure 3.17 shows two EELS spectra. Top spectrum represents a Nb-rich particle on an aluminium replica (i.e. without any undesirable carbon). This spectrum corresponds essentially to a NbC-based phase, although a minor nitrogen content is detected. Bottom spectrum comes from an Al-rich particle on a aluminium replica; Although Al-content can obviously not be discussed, it is seen that no significant carbon is detected, which thus confirms that the Al-rich family is, as expected, essentially pure AlN.

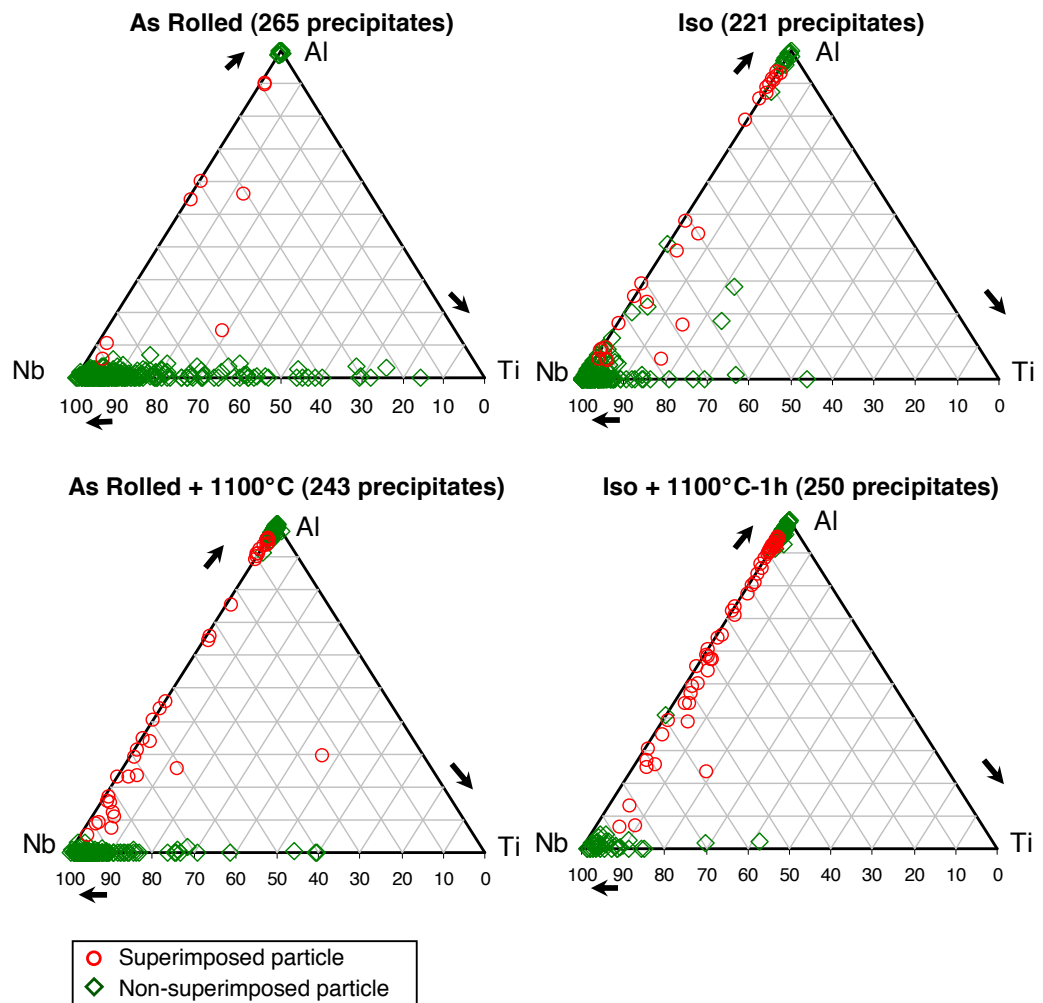


Figure 3.16: Ternary composition diagrams of 16MnCr<sub>5</sub>+Nb grade steel states. Red symbols (circles) represents Nb-rich precipitates superimposed to AlN. Green symbols (diamonds) correspond to non-superimposed precipitates.

The possible correlation between precipitate chemical composition and precipitate size will be discussed in the following. Only non-overlapping particles will be considered in the following.

### 3.3.3.1.2 Precipitated volume fraction

Figure 3.18 presents the evolution of volume fraction of AlN and NbC for *As Rolled* and *Iso* states before and after heat treatment at 1100°C. For these initial states the precipitated volume fraction is much higher for the *Iso* state than for the *As Rolled* state. After a treatment of 1 hour at 1100°C the

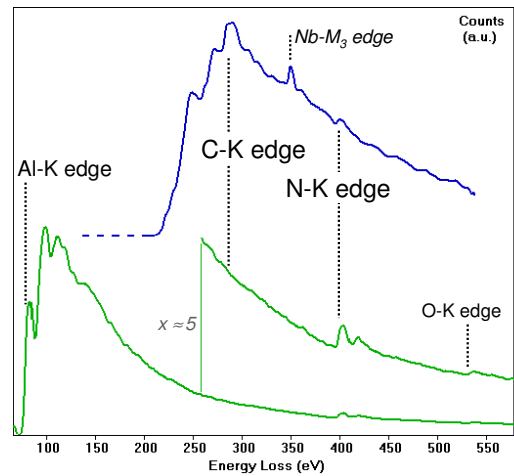


Figure 3.17: EELS spectra from a Nb-rich precipitate observed on an aluminium-based replica (upper spectrum, after background subtraction before the Nb-M edge) and from a Al-rich one (lower spectrum, after background subtraction before the Al-K edge) on a aluminium replica (16MnCr5+Nb alloy in the As Rolled state); for the latter, the zooming by a factor 5 shows the absence of significant carbon.

volume fraction is very similar for both states. For the *Iso* state, the volume fraction for the initial state is almost the same than after a treatment at 1100°C. For the *As Rolled* state, there is an increase of the volume fraction after the treatment at 1100°C, and the volume fraction reaches the equilibrium.

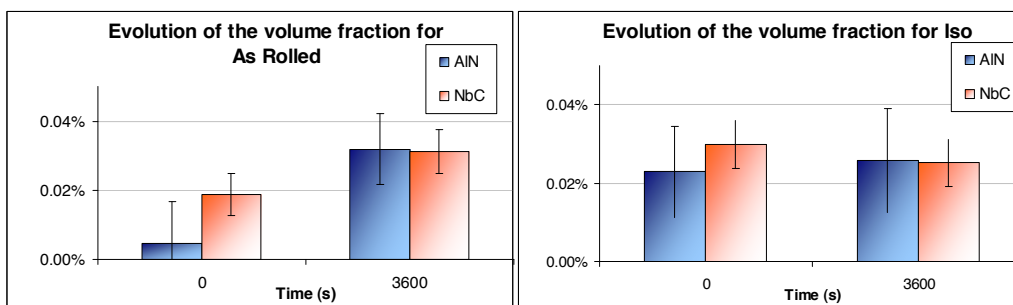


Figure 3.18: Evolution of volume fraction of AlN and NbC before and after 1 hour at 1100°C

### 3.3.3.1.3 Precipitate size evolution

To obtain the precipitate size distribution, HAADF micrographs have been analyzed in order to measure the projected area of precipitates

and deduce their sizes. Precipitates are then arranged in size classes of size  $\Delta r$ . Note that the number of classes, and therefore  $\Delta r$ , have been manually optimized according to the number of analyzed precipitates. In order to compare distributions, numbers of precipitates have to be expressed as number density, which is the number of precipitates in a given class divided by the class size  $\Delta r$ . Then the number density distribution  $N_n$  is normalized in order to get the correct precipitate volume fraction  $f$ :

$$f = \sum_i \left( \frac{4}{3} \pi r_i^3 N_n(r_i) \Delta r \right) \quad (3.1)$$

Figure 3.19 presents the distributions for investigated states of the 16MnCr5+Nb microalloyed steel. We separated the two precipitate types, AlN and NbC. These distributions are Log-normal except for the NbC category of the *Iso* state. Indeed, a bimodal distribution is observed, which may be due to a precipitation of niobium carbides during the isothermal annealing. As we have seen before, there is an increase of the particles number density after an isothermal annealing or after a treatments of 1 hour at 1100°C. It seems for the *Iso* state, that small NbC precipitates are dissolved after a treatments at 1100°C, leading to an increase of the precipitate size. The evolution of the precipitate size is reported on figure 3.20. The precipitate mean radii of NbC in the *Iso* state is much smaller than the all others mean radius. This is due to the apparition of small particles (see figure 3.19) for the same state. For the other states the precipitate mean radius is nearly constant for Nb-rich or Al-rich precipitate.

Figure 3.21 presents the correlation between the precipitate chemical composition and the precipitate size. We notice that for all investigated states there are large and small particles in each precipitate population (Nb-rich and Al-rich). Thus, there is not significative correlation. Furthermore, these results are in agreement with the precipitate volume fraction. Indeed, for the *As Rolled* state there are few AlN precipitates, whereas after an isothermal treatment or a reversion treatment at 1100°C, more AlN can be observed.

#### 3.3.3.1.4 Conclusion on the precipitation state

During the precipitation state study we have highlighted a clear difference between the *As Rolled* state and the *Iso* state concerning the precipitate size. Indeed, the *Iso* state presents a second population of very small precipitates rich in niobium, and the mean radius in the *As Rolled state* is approximately twice that of the *Iso* state. However, after a treatment of 1 hour at 1100°C, distributions become equivalent.

The chemical composition study allowed to observe two precipitate types:

- Aluminium rich, essentially a pure AlN phase
- Niobium rich, essentially NbC precipitate

The presence of “mixed” particles is due to the nucleation of Nb-rich precipitates on aluminium nitrides and seems to be a measurement artefact due to a superposition effect (a possible minor sample drift during the EDX analysis - 20 seconds typically - is also possible, which can contribute to the apparent “mixing”).

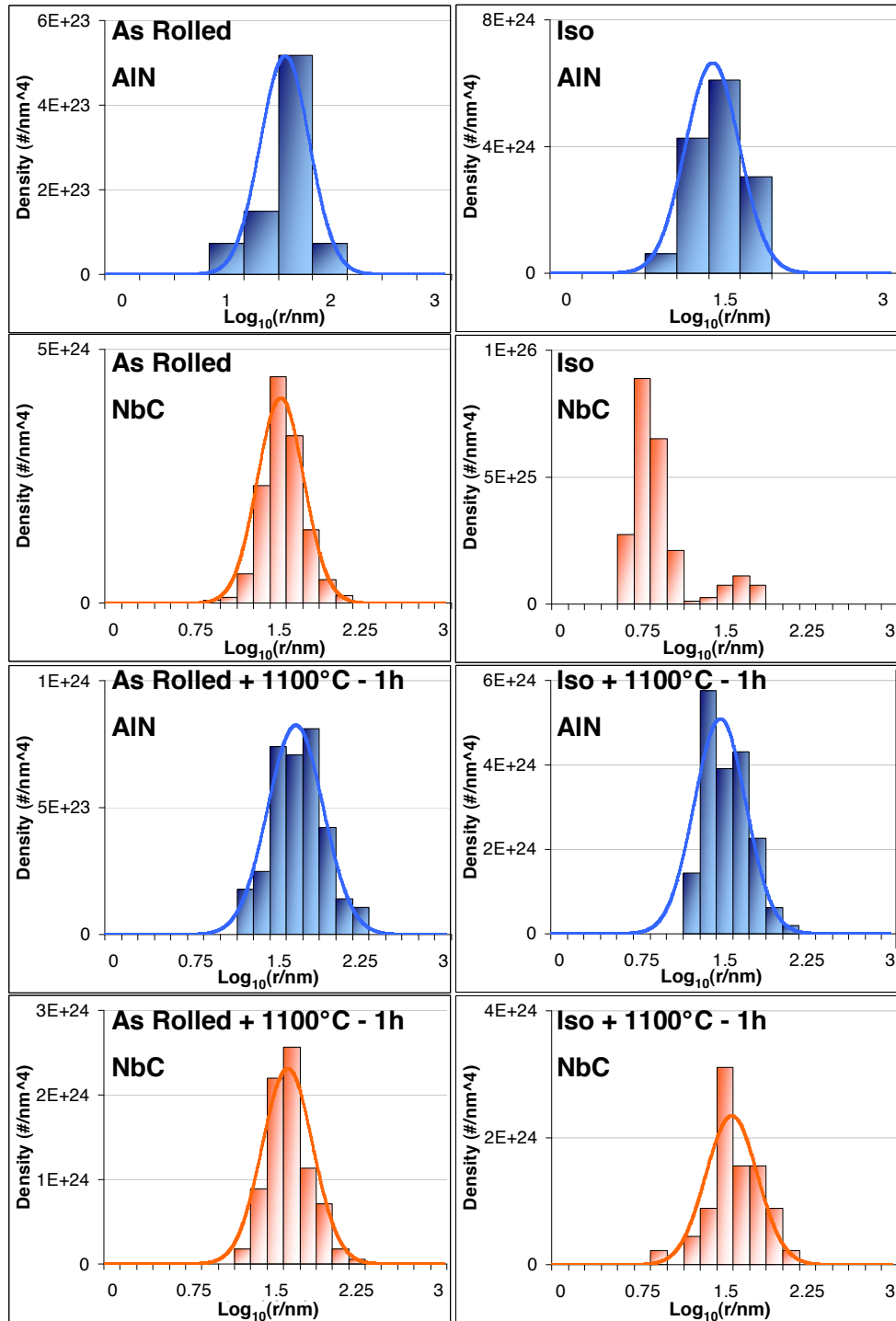


Figure 3.19: Density distribution of AlN and NbC for the As Rolled state, the Iso state, the As Rolled state + 1100°C and the Iso state + 1100°C. Distributions are normalized in order to get the correct volume fraction and are fitted by a Log-normal when it is possible.

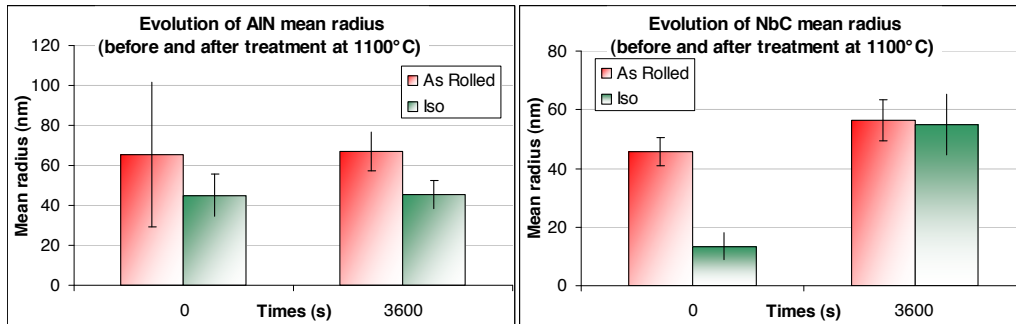


Figure 3.20: Evolution of the particle mean radius during isothermal reversion at  $1100^{\circ}\text{C}$  in  $16\text{MnCr}_5+\text{Nb}$  alloy on As Rolled and Iso states. Values of mean radius have been determined from size distributions measured on STEM in SEM images; the error bar reflects the amount of particles observed.

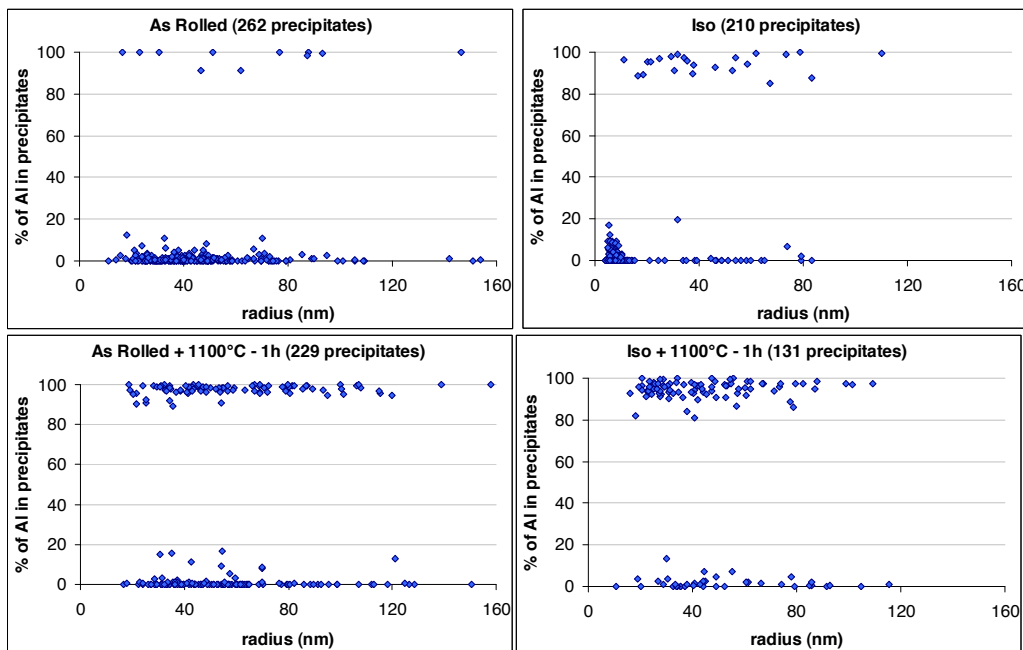


Figure 3.21: Comparison between the precipitate chemical composition and their size a) As Rolled state; b) Iso state; c) As Rolled state +  $1100^{\circ}\text{C}$ ; d) Iso state +  $1100^{\circ}\text{C}$ .

### 3.3.3.2 FeVNbCN precipitation state

For clarity, a brief summary of the FeVNbCN results, detailed in Chapter 2, will be presented in this paragraph.

EDX and EELS analysis were performed on several reversion states; they have clearly evidenced the two types of precipitate: V-rich and Nb-rich precipitates. The fraction of the latter category increases when reversion temperature and/or time increases (see figure 3.22). EELS analysis highlights that V-rich are carbonitrides while Nb-rich are carbides. Figure 3.23 presents ternary diagrams showing the chemical composition of each analyzed precipitates for reversions at 900°C during 200 minutes and 1050°C during 2 minutes. It shows that Nb-rich precipitates are systematically rich in carbon while V-rich precipitates are mixed in carbon and nitrogen.

Figure 3.24 presents the volume fraction evolution for these NbC and VCN precipitates as a function of temperature and treatment time. After 2 minutes at 1050°C the VCN volume fraction is very low and, NbC precipitates start to be solutionized at 1050°C.

Figure 3.25 presents the evolution of the precipitate mean radius for VCN and NbC. At 900°C there is no evolution of the mean radius of VCN as well as of NbC. At 1050°C we observe an increase of the mean radius for the two precipitate types with the increase of treatment duration, which is a signature of the coarsening regime. Furthermore, the size of VCN particles is systematically higher than that of the NbC ones.

### 3.3.4 Correlation between grain size and precipitation state

In a first step we will present the correlation obtained for the  ${}_{16}\text{MnCr}_5+\text{Nb}$  study, and then the correlation obtained for the FeCVNbN model alloy.

#### 3.3.4.1 Simple modelling for grain growth

Experimental results will be compared with two simple thermodynamic models, which predict the austenitic grain size for a given precipitation state, those of Zener [Zener 48] and Rios [Rios 87].

To calculate the equilibrium grain size, both authors assumed that the driving pressure for grain growth  $F$  is equal to the precipitate driving pressure  $F_Z$ . The driving pressure  $F$  arises from the reduction of interface area accompanying grain growth [Gladman 97], with:

### Chapter 3. Correlation between the precipitation state and grain growth

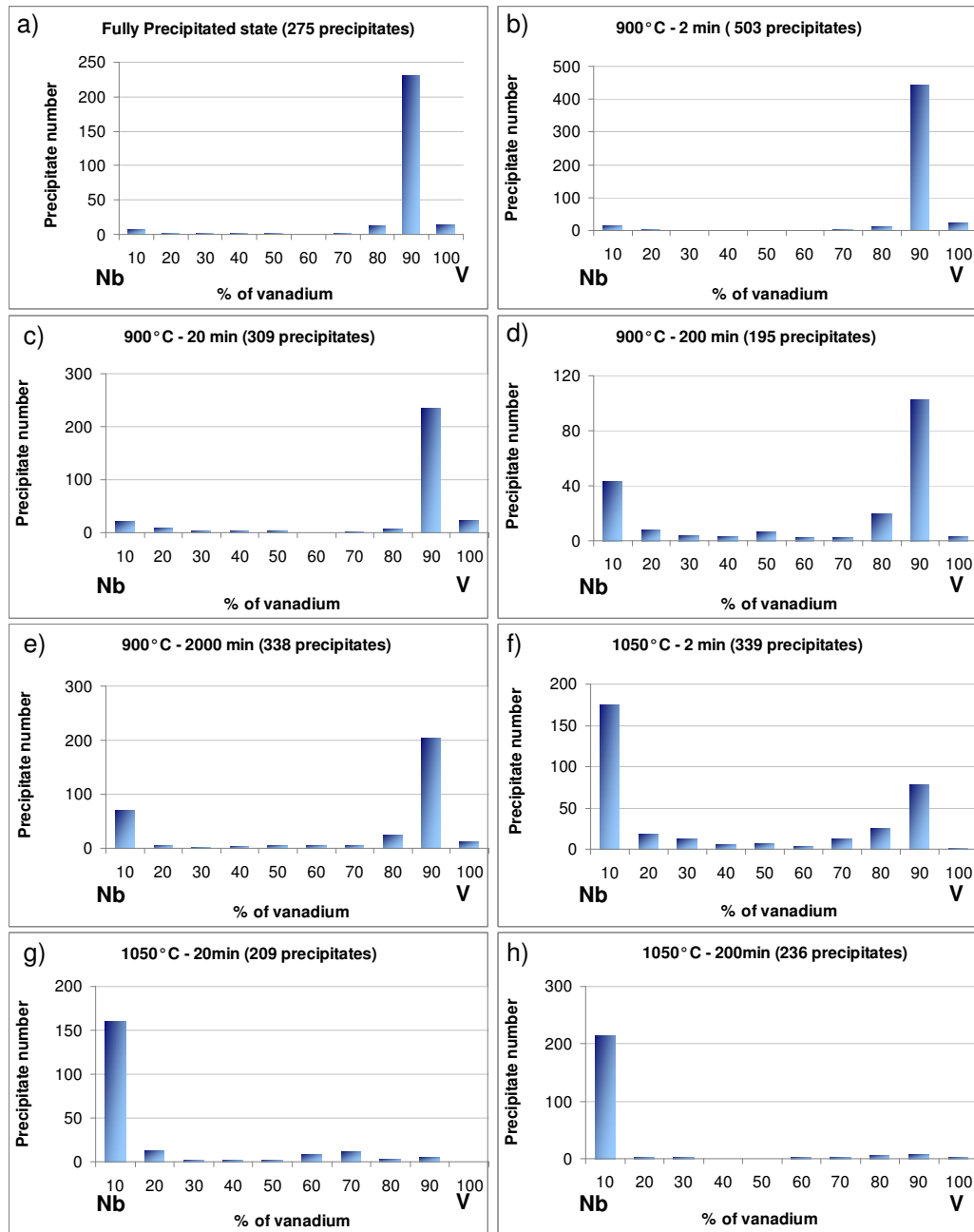


Figure 3.22: Evolution of the precipitate chemical composition with the treatment duration and temperature.

$$F = \lambda \frac{\gamma}{D} \quad (3.2)$$

where  $D$  the average grain size,  $\gamma$  the interfacial energy and  $\lambda$  is a geo-

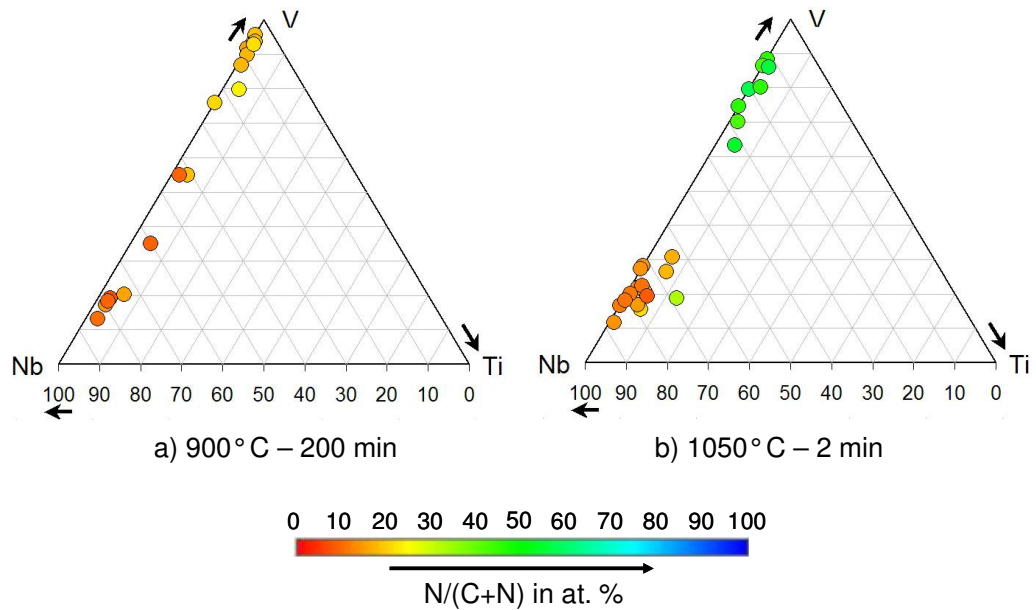


Figure 3.23: Ternary diagrams showing the chemical composition of each analyzed precipitate category for: a) the 900°C - 200 minutes state and b) the 1050°C - 2 minutes state. A nitrogen content scale is presented on the figure, showing that Nb-rich precipitates are carbides while V-rich particles are carbonitrides.

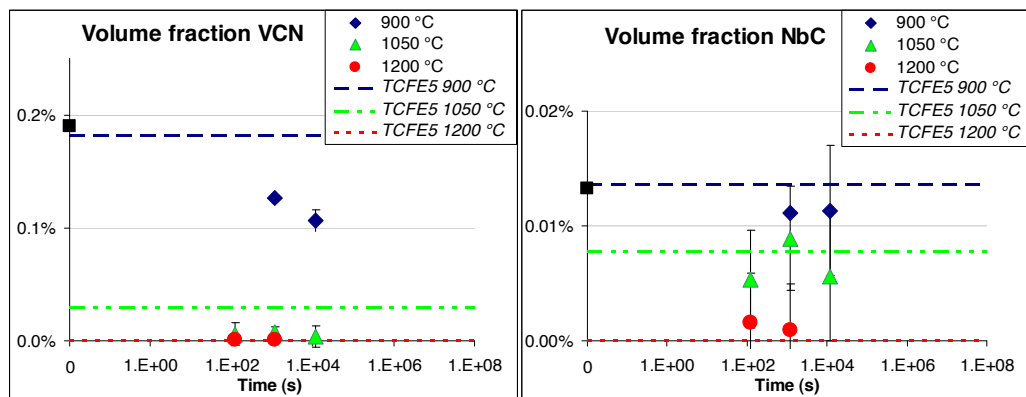


Figure 3.24: Evolution of volume fraction of a) VCN and b) NbC. Thermodynamic equilibrium calculated by [TCFE5 05] are given on the figure.

metrical factor. The pinning pressure  $f_z$  for one precipitate located on a grain boundary and the number density of obstacles are given by:

$$f_z = k_s r \gamma \quad (3.3)$$

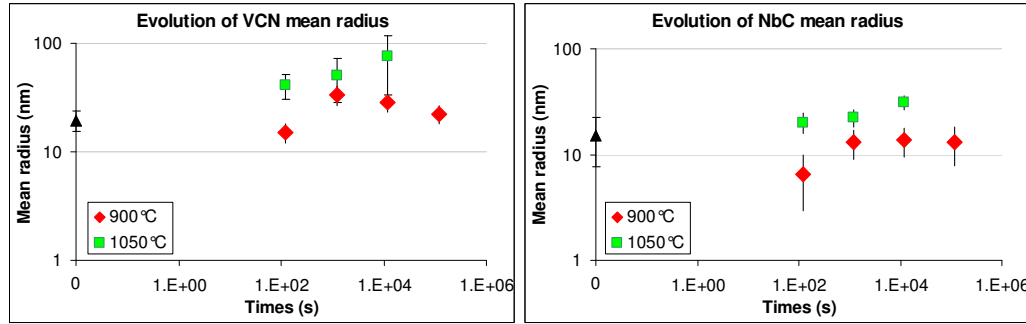


Figure 3.25: Evolution of VCN and NbC mean radius with treatment duration and temperature. Error bars take into account the quantity of observed particles.

$$n = \frac{f}{k_v r^3} \quad (3.4)$$

where  $k_s$  and  $k_v$  are geometrical factors ( $k_s = \pi$  and  $k_v = 4/3\pi$  for a spherical particle) and  $f$  the precipitate volume fraction. From the equations 3.3 and 3.4, the pinning pressure  $F_Z$  can be expressed as:

$$F_Z = 2r \cdot n \cdot f_z = \frac{2k_s \gamma}{k_v} \sum_i \frac{f_i}{r_i} \quad (3.5)$$

where  $i$  stands for each precipitate population. This approach leads to the now classical expression for the critical grain size diameter  $D_c$ , for which pinning and driving pressures equilibrate:

$$\frac{D_c}{2} = \frac{\beta}{\sum_i \frac{f_i}{r_i}} \quad (3.6)$$

with  $\beta$  a geometrical factor (e.g.  $\beta = 4/3$  for Zener [Zener 48],  $\beta = 1/6$  for Rios [Rios 87]). Rios assumed for his model that a “loop” of grain boundary stays around the precipitate after the passage of the grain boundary through the precipitate.

These kinds of models are very useful to predict the grain size in the case of normal grain growth and when the system has time to reach the equilibrium, i.e. when grain boundary mobility is high enough. In other cases, and in particular when abnormal grain growth occurs, these models fail.

#### 3.3.4.2 16MnCr5+Nb industrial steel

The inspection of experimental results (precipitate volume fraction and mean precipitate size) obtained on the 16MnCr5+Nb industrial steel at the final precipitation states does not explain the differences in PAGS (see figure 3.9). It is thus necessary to investigate the initial states. Indeed, the *Iso* state presents a higher volume fraction of small precipitates, which, to restrict the PAGS, is better than a small volume fraction of large precipitates as in the case of the *As Rolled* state.

Comparison between the models and experimental results is given in table 3.4. Here, precipitates are supposed to be a mixture of AlN and NbC, i.e. the global precipitated volume fraction and the mean radius of all precipitates have been considered. We can see that values obtained by Rios are much closer than those obtained by Zener. This latter model is indeed known to give overestimated values with a factor around 10 [Gao 98] [Rios 87]. In the case of the *As Rolled* state, none of these models presents a good agreement with the experimental results. For the *Iso* state at 900°C the prediction of the Rios model is closed to the value of the experimental diameter, whereas, at 1100°C both models fail. In the case of AGG the thermodynamic predictions and the experiments could not be compared because the models do not work in this regime. In other cases (*As Rolled* state at 900°C and *Iso* at 1100°C), if the equilibrium PAGS is not reached, the models could not be in agreement with the experimental results. Furthermore, for the treatment at 900°C the precipitation states of the *As Rolled* state may evolve (the precipitate volume fraction could increase). Thus, it is important to take into account the evolution of the precipitation state during reversion treatments as well as the mobility of grain boundary.

Table 3.5 shows results obtained from the Rios and Zener models when AlN and NbC are considered as two populations. Predictions of the models show that for the *As Rolled* and *Iso* states at 900°C, NbC precipitates, which have a higher volume fraction and a lower precipitate size than AlN, have a better pinning effect than AlN precipitates. When their respective distributions are similar, there is no obvious difference.

#### 3.3.4.3 FeVNbCN model alloy

Results obtained from the precipitation state and the austenitic grain size studies show that a precipitate solutionizing and an increase of the precipitate size leads to an increase in mean grain size. Indeed when the precipitation state does not evolve (e.g. at 900°C) there is no grain growth, whereas at 1050°C, nearly all vanadium-based particles are solutionized, and the precipitate size

	<i>As Rolled</i>				<i>Iso</i>			
	900°C-2min		1100°C-1hour		900°C-2min		1100°C-1hour	
$f$	$2.4 \times 10^{-4}$		$5 \times 10^{-4}$		$4.3 \times 10^{-4}$		$4.1 \times 10^{-4}$	
$\bar{r}$ in nm	47		60		17		45	
$D_{exp}$ in $\mu\text{m}$	7		19*		6		9	
$D_{crit}$ in $\mu\text{m}$	Z	R	Z	R	Z	R	Z	R
	616	77	319	40	105	13	294	37

Table 3.4: Critical diameter calculated with Zener (Z) and Rios (R) equations. Experimental precipitate volume fraction, mean precipitate radii and mean austenitic grain diameter are given in the table for the As Rolled and Iso states. The star means that the growth is abnormal, hence comparison with models is not possible.

AlN								
	<i>As Rolled</i>				<i>Iso</i>			
	900°C-2min		1100°C-1hour		900°C-2min		1100°C-1hour	
$f$	$5.2 \times 10^{-5}$		$3.5 \times 10^{-4}$		$2.5 \times 10^{-4}$		$2.8 \times 10^{-4}$	
$\bar{r}$ in nm	66		67		45		45	
$f/r$	788		5173		5504		6144	
NbC								
	<i>As Rolled</i>				<i>Iso</i>			
	900°C-2min		1100°C-1hour		900°C-2min		1100°C-1hour	
$f$	$1.9 \times 10^{-4}$		$3.1 \times 10^{-4}$		$2.9 \times 10^{-4}$		$2.5 \times 10^{-4}$	
$\bar{r}$ in nm	46		56		13		55	
$f/r$	4108		5515		22367		4587	
$D_{crit}$ in $\mu\text{m}$	Z	R	Z	R	Z	R	Z	R
	545	68	250	31	96	12	249	31

Table 3.5: Critical diameter calculated with Zener (Z) and Rios (R) equations for two populations of precipitates. Experimental precipitate volume fraction and mean precipitate radii are given in the table for the AlN and NbC in As Rolled and Iso states.

increases with the treatment duration. Table 3.6 summarizes volume fraction, precipitate size and grain diameter obtained previously, and further gives the critical grain size calculated by equation 3.6 using Rios or Zener parameter.

Rios results are in agreement with experimental observations for treatments at 900°C, whereas Zener's values are much higher. For treatments at

time	900°C				1050°C					
	20 min		200 min		2 min		20 min		200 min	
$f$	$1.4 \times 10^{-3}$		$1.2 \times 10^{-3}$		$1.1 \times 10^{-4}$		$1.7 \times 10^{-4}$		$9.4 \times 10^{-5}$	
$r$ in nm	33		29		41		50		76	
$D_{exp}$ in $\mu\text{m}$	6		6		14*		28*		38*	
$D_{crit}$ in $\mu\text{m}$	Z	R	Z	R	Z	R	Z	R	Z	R
	64	8	64	8	980	123	800	100	2163	270

Table 3.6: Critical diameter calculated with Zener (Z) and Rios (R) equations. Experimental precipitate volume fraction, mean precipitate radii and mean austenitic grain diameter are given in the table for the FeVNbCN reversion state. The star means that the growth is abnormal.

1050°C both models overestimate the austenitic grain size. This is due to the fact that there is an abnormal growth regime. No comparison is possible at 1200°C because no precipitates are observed at this temperature.

#### 3.3.4.4 Modeling grain growth kinetics

If we want to follow the PAGS evolution during non-isothermal industrial treatments, it is clear that a model predicting the grain size when the precipitation state evolves is needed. Here, we will associate a thermodynamical model for grain growth and the precipitation model presented in chapter 2. The pinning mechanism will be described by a Zener type model, and a grain boundary mobility is incorporated in order to express the austenitic grain growth kinetics. In the presence of non-coarsening spherical particles, the austenite grain growth rate can be expressed by the following equation [Banerjee 09]:

$$\frac{dD}{dt} = M(F - F_Z) \quad (3.7)$$

where  $D$  is the austenitic grain diameter,  $M$  is the grain boundary mobility,  $F$  is the driving pressure for grain growth and  $F_Z$  is the pinning pressure induced by precipitates. The grain boundary mobility is given by:

$$M = M_0 \exp\left(-\frac{Q}{RT}\right) \quad (3.8)$$

with  $M_0$  a pre-exponential factor,  $R$  the gas constant,  $T$  the temperature and  $Q = 350 \text{ kJ}\cdot\text{mol}^{-1}$  the activation energy for grain boundary mobility [Moon 07b]. Driving pressure can be simply expressed by the equation 3.2

with  $\lambda = 4$ . We have seen before that using the Zener expression for the pinning pressure overestimates the critical grain size, thus for the following, we will use the Rios expression given by:

$$F_Z = \frac{12f}{r}\gamma \quad (3.9)$$

In the case of the presence of several types of pinning particles, equation 3.9 can be rewritten as:

$$F_Z = 12\gamma \sum_i \frac{f_i}{r_i} \quad (3.10)$$

where the summation index  $i$  represents all present phases.

This model have been applied to the FeVNbCN model alloy. Figure 3.26 shows the PAGES evolution and the evolution of the  $f/r$  ratio for NbC and VCN precipitates. There is a good agreement between experimental grain sizes and those predicted by the model. We must be careful at 1050°C, because there is an AGG regime, and consequently the model could not be applied. The evolution of the  $f/r$  ratio shows that the austenite grains start to grow when the  $f/r$  ratio (i.e. the pinning force) of VCN precipitates decreases strongly. The principal advantage of this model is that it is possible to compare PAGES even if the precipitate chemistry is not characterized. However, precipitate size distribution are not taken into account and this approach could not be applied if the system experiences AGG.

### 3.4 Conclusion of the chapter

In this chapter we have chosen to study the PAGES evolution for two steels: an industrial gear steel and a FeVNbCN model alloy, which was previously finely characterized (see chapter 2).

To identify the occurrence of PAGES, the Bechet-Beaujard etching, which reveals the impurities located at the prior austenitic grain boundaries, has been used. This etching technique generally gives good results on industrial steels, but can be difficult to apply on a model alloy with few impurities.

The precipitation states have been characterized using techniques developed in Chapter 2, such as the TEM and its associated techniques for size and chemistry, and the electrolytic dissolution for volume fraction.

The 16MnCr5+Nb microalloyed steel presents a better behaviour in terms of grain growth after an isothermal treatment during which fine precipitation

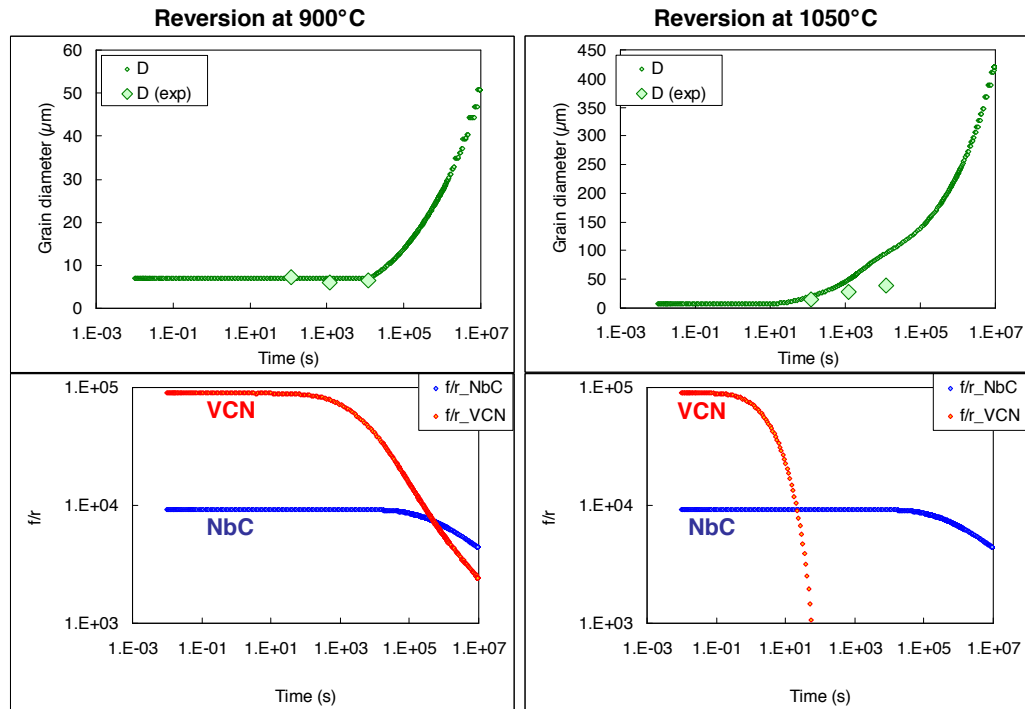


Figure 3.26: Model prediction for the PAGS and evolution of the  $f/r$  ratio (responsible of the pinning) during reversion at  $900^{\circ}\text{C}$  and  $1050^{\circ}\text{C}$ .

NbC and AlN occurs. Hence, this initial precipitation state seems to play an important role in the austenitic grain growth.

No evolution of grain size of the FeVNbCN model alloy occurs during treatments at  $900^{\circ}\text{C}$ , for which the precipitation state does not evolves. After a treatment of 2 minutes at  $1050^{\circ}\text{C}$  AGG appears, probably due to the solutionizing of precipitates and to the increase of their radii.

Experimental results have been compared to analytical models predicting the equilibrium grain size. It appears that the Rios model presents better agreement with experimental results than Zener model for both  $16\text{MnCr5}+\text{Nb}$  and FeCVNbN steels. The Zener model indeed overestimates the critical grain size.

A model predicting the grain size, and taking into account the grain boundaries mobility has been coupled to the precipitation kinetics model developed in Chapter 2. Predictions of this coupled approach are in good agreement with experimental results for the FeVNbCN alloy. Note that this approach can only be applied for normal grain growth.



## CHAPTER 4

# A Criterium for Abnormal Grain Growth

### 4.1 Introduction

High temperature thermo-mechanical processes are commonly involved in manufacturing bar steel components (for example, quenching of spring steels, carburizing of gears, etc). Austenite grain growth is often an issue during high temperature exposure of low and medium alloy steels. This is because, even after quenching and tempering, mechanical properties are negatively impacted by a large Prior Austenite Grain Size (PAGS) [Hyde 94]. Micro-alloying has long been recognized as an efficient way to control PAGS and is therefore widely used, for example, in modern spring or carburizing steel grades.

The problem of predicting grain size in microalloyed steels (or, in general, in steels containing second phase precipitates) has been addressed by a number of authors [Gladman 66][Rios 87][Hillert 88], and basic formulate for grain size prediction, such as that proposed by Zener [Zener 48], can now be found in most metallurgy textbooks. Zener's and other similar models attempt to calculate the equilibrium grain size by deriving expressions for two forces having opposite actions on grain dimensions. First, a driving pressure  $F$  arises from the reduction of interface area accompanying grain growth, with:

$$F = \lambda \frac{\gamma}{D} \quad (4.1)$$

where  $D$  the average grain size,  $\gamma$  the interfacial energy and  $\lambda$  is a geometrical factor wich depends on grain shape assumption. Second, a pinning pressure  $f_z$  is exerted on grain bondary by a particle of radius  $r$ :

$$f_z = k_s r \gamma \quad (4.2)$$

where  $k_s$  is a geometrical factor ( $k_s = \pi$  for a spherical particle). Assuming homogeneous pinning, the number density of obstacles  $n$  is given by:

$$n = \frac{f}{k_v r^3} \quad (4.3)$$

where  $k_v$  is an other geometrical factor ( $k_v = 4/3\pi$  for spherical precipitates) and  $f$  the precipitate volume fraction. These approaches lead to the now classical expression for the critical grain size diameter  $D_c$ , for which pinning and driving pressures compensate:

$$\frac{D_c}{2} = \beta \frac{r}{f} \quad (4.4)$$

with  $\beta$  a geometrical factor (e.g.  $\beta = 4/3$  for Zener [Zener 48],  $\beta = 1/6$  for Rios [Rios 87]).

These models are very useful when used to predict grain size in relatively simple cases (e.g. isothermal treatment), where grains have time to collectively reach their limiting size. However, they completely fail to predict grain size evolution for more complex treatments, essentially for two reasons: (i) since the grain boundary mobility is limited whatever the temperature, kinetics effects are expected and the grain growth will take time to occur; (ii) instabilities like Abnormal Grain Growth (AGG) might occur: one large grain growing at the detriment of its smaller neighbouring.

In this chapter, we will mainly focus on the second point. AGG is indeed a crucial issue for steels makers. It can lead to catastrophic undesirable mechanical instabilities (cavitation, rupture).

Despite of an intense activity, AGG is to date not clearly understood. An overwhelming mass of scientific papers has been published on the modelling of grain growth. Different methods exist, and in particular: (i) vertex modelling, with a basic idea that the minimization of free energy can be achieved exclusively by the motion of the triple junctions [Barrales-Mora 09] [Weygand 99]; (ii) Monte Carlo models assuming that a grain will grow if the total free energy of the system decreases (through the decrease of grain boundaries surface) [Anderson 84] [Srolovitz 84] [Yu 03]; (iii) Phase Field based approaches [Shahandeh 08] [Chang 09]. It is widely accepted that AGG is connected to grain boundaries mobility. It has been showed that texture heterogeneities affect the grain boundaries mobility, and thus can explain AGG [Messina 01] [Grest 90] [Suwa 07]. Secondly, phase particles can also play a primordial role in the onset of AGG [Apel 09] [Maazi 09]: it has been shown that when the mean distance between particles is comparable

to the grain size, larger grains may grow faster than smaller ones, leading to AGG [Bréchet 05].

Some analytical models also treat AGG. Andersen’s model [Andersen 95b] predicts the risk of the propagation of an existing abnormally large grain in a matrix of small grain. It is based on a geometric assumption that small polygonal grains with less than six neighbours will shrink, however, large grain with more than six neighbours will grow. However, this model does not explain the apparition of this abnormal grain.

For a given precipitation state, and thermal treatment, evaluating the risk of AGG to occur is thus primordial. The aim of this chapter is then to develop a new criterion for AGG based on the Bréchet and Militzer model [Bréchet 05]. This criterion will be applied on a model microalloyed steel before treating an industrial microalloyed steel in order to predict the risk of an onset for AGG.

## 4.2 Materials and treatments

In this section two microalloyed steels will be investigated: the model alloy FeVNbCN and the industrial microalloyed steel 16MnCr5+Nb. We quickly recall the chemical composition and heat treatments carried out on these alloys. Tables 4.1 and 4.2 show their chemical composition.

	<b>C</b>	<b>Si</b>	<b>Mn</b>	<b>S</b>	<b>Ni</b>	<b>Cr</b>
wt. %	<b>0.48</b>	0.028	0.088	0.017	0.023	0.049
at. %	<b>2.2</b>	0.055	0.088	0.029	0.021	0.052
	<b>Mo</b>	<b>Ti</b>	<b>Nb</b>	<b>V</b>	<b>N</b>	
wt. %	0.007	0.001	<b>0.012</b>	<b>0.202</b>	<b>0.0063</b>	
at. %	0.004	0.0011	<b>0.0071</b>	<b>0.217</b>	<b>0.025</b>	

Table 4.1: Chemical composition of the FeVNbCN steel (in wt.% and at.%)

	<b>C</b>	<b>Si</b>	<b>Mn</b>	<b>Ni</b>	<b>Cr</b>	<b>Al</b>	<b>Nb</b>	<b>N</b>
wt. %	0.208	0.178	1.207	0.140	1.146	0.034	0.037	0.00234

Table 4.2: Chemical composition of the 16MnCr5+Nb steel (in wt.%)

To ensure complete dissolution of precipitates the FeVNbCN alloy has been heated to 1280°C for 30 minutes in argon then water quenched. Then, in order to achieve a “fully-precipitated state” this steel has been treated during 10 hours at 700°C followed by 10 days at 800°C and water quenched. Justification of this treatment is given in [Epicier 07]. To investigate a wide range of precipitation states and grain sizes, the alloy was subjected to different isothermal reversion treatments in the austenitic domain at temperatures ranging from 900°C to 1050°C and for 2 to 2000 minutes, followed by a water quench. All these treatments were performed under vacuum in quartz capsules (see figure 4.1).

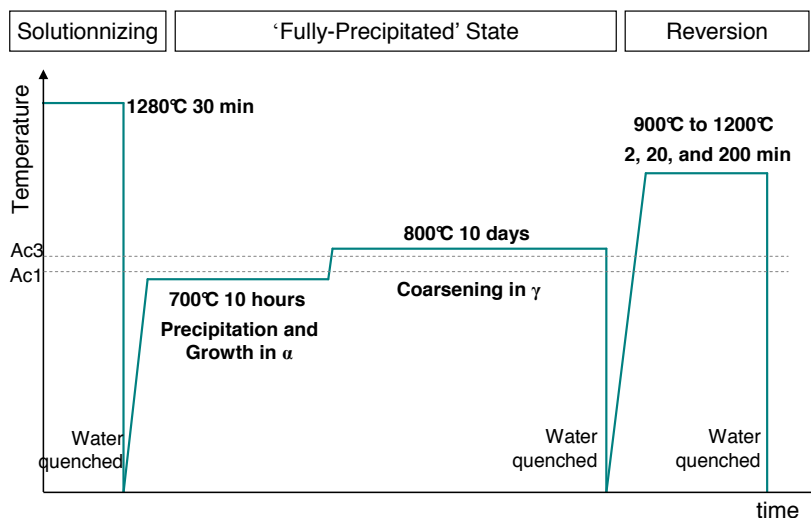


Figure 4.1: Heat treatments for the FeVNbCN alloy.

The industrial microalloyed steel was submitted to the following thermomechanical treatment: after the hot rolling at 1050°C this alloy is cooled slowly in air. This state, called “As Rolled”, undergoes a two steps isothermal treatment: 30 minutes at 900°C and 1 hour at 600°C before being cooled slowly to get the state named “Iso”. Heat treatment of 1100°C for 1 hour have been performed on these two states in order to simulate an industrial carburizing treatment (see figure 4.2).

The austenitic grain size is obtained using a chemical etching called “Béchet-Beaujard” (picric acid + HCl+ Teepol) heated at 50°C on surface polished to 1 μm. This etching reveals the prior austenitic grain boundaries decorated by precipitated impurities. To improve the statistical significance of our study, it is essential to characterize an important number of randomly selected areas. We then measured about 200 austenitic grains from optical

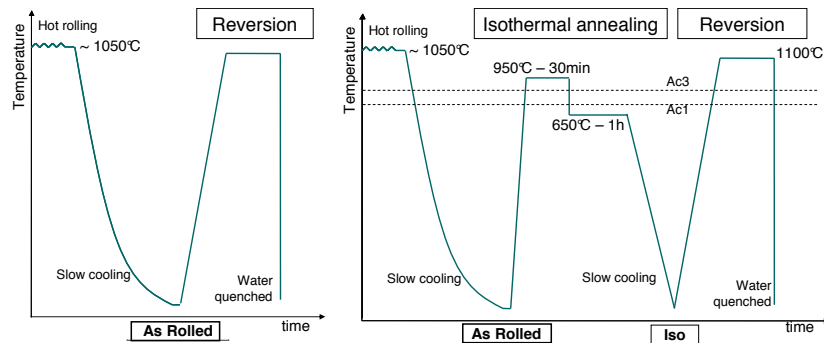


Figure 4.2: Heat treatments for the 16MnCr5+Nb steel.

micrographs. It is therefore essential to take an important number of random areas. A manual tracing of these micrographs is performed and then digitized as a binary image. This tracing is treated by the software Image-Tool in order to calculate the mean equivalent diameter of each grain: this diameter corresponds to the disk with the same area as that of the treated grain.

TEM observations of precipitates were performed on aluminium extraction replicas for carbon analysis. They were prepared by evaporating an aluminium film on the surface of samples polished to  $1\ \mu\text{m}$  finished to diamond paste and slightly etched with a 0.4% Nital solution. The final dissolution of the matrix is performed in an ethanol-nitric acid bath. Electron microscopy was performed using a JEOL 2010F field emission gun transmission electron microscope operating at 200 kV. The microscope was fitted with a JEOL annular detector allowing High Angle Annular Dark Field (HAADF) imaging in the scanning mode (STEM). Precipitate distribution size is obtained from the area of the closest ellipse fitting the projection of particles within HAADF micrographs using a software developed by T. Epicier. More details will be found in Chapter 2.

Precipitate volume fraction is obtained using the electrolytic dissolution technique. This method consists in the dissolution of the matrix into an electrolytic solution (lithium chloride + salicylic acid + methanol). Precipitates are recovered by filtering this solution and the filter is then rinsed several times in methanol before being dissolved in a solution of  $\text{H}_2\text{O}$ ,  $\text{HCl}$ ,  $\text{HF}$ ,  $\text{HNO}_3$  and  $\text{HClO}_4$ . The residue is redissolved in a solution of  $\text{HF}$  and  $\text{HNO}_3$  and is analysed inductively by a coupled plasma spectrometer (ICP). More details are given in [Acevedo 07] and in Appendix B

## 4.3 Experimental results

In this section, we briefly recall the precipitation state and grain size distributions obtained for FeVNbCN alloy and 16MnCr5+Nb industrial steel in Chapter 2 and Chapter 3 respectively.

### 4.3.1 Model alloy FeVNbCN

#### 4.3.1.1 Precipitate size distribution

Precipitates measured from HAADF micrographs were arranged in different size classes of size  $\Delta r$  in order to obtain the precipitate size distribution. Note that the number of classes, and therefore  $\Delta r$ , are optimized depending on the number of analyzed precipitates. In order to compare distributions, numbers of precipitates have to be expressed as number densities, which represent the number of precipitates in a given class divided by the class size  $\Delta r$ . Then the number density distribution  $N_n$  is normalized in order to get the correct precipitate volume fraction  $f$ :

$$f = \sum_i \left( \frac{4}{3} \pi r_i^3 N_n(r_i) \Delta r \right) \quad (4.5)$$

Figure 4.3 presents normalized precipitate size distributions for all heat treatments performed on the FeVNbCN steel. We can see that there is a decrease in precipitate number when increasing the treatment duration and temperature. For heat treatments performed at 1050°C we observe an increase of the mean radius when increasing the treatment duration, which is a signature of the coarsening regime.

#### 4.3.1.2 Volume fraction

Figure 4.4 presents the evolution of the volume fraction of VCN and NbC, the two precipitates species observed in this alloy (see chapter 2). These measurements point out a quick solutionizing of vanadium from 1050°C. For niobium, at 900°C there is no change in the volume fraction but from 1050°C it starts to be solutionized.

#### 4.3.1.3 Austenitic grain size distribution

The grain size distributions plotted on figure 4.3 are expressed in terms of number density (number of grains of a given  $N_i(D)$  divided by the class width  $\Delta D$ ), normalized to 1 such as:

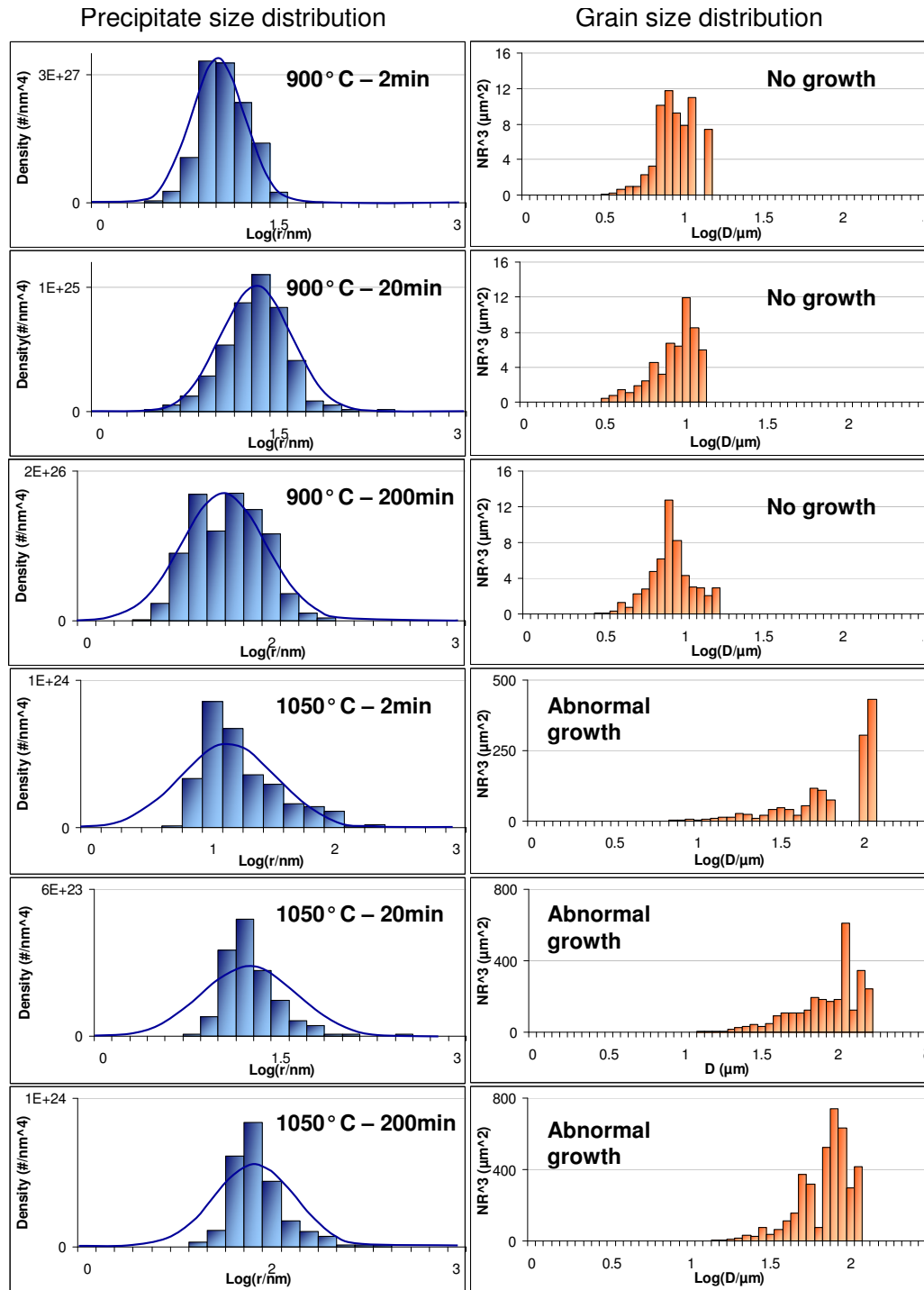


Figure 4.3: Experimental precipitate and grain size distribution of the FeVNbCN model alloy. The kind of grain growth is indicated on the graphs of grain size distributions.

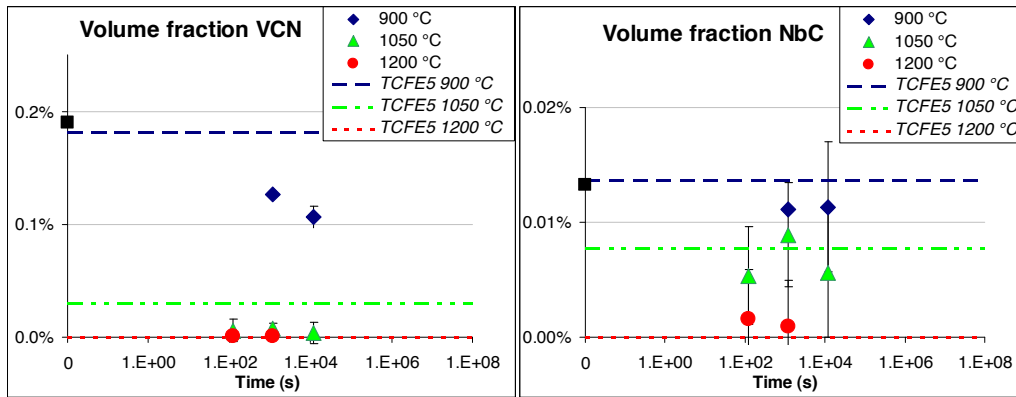


Figure 4.4: Evolution of volume fraction of a) VCN and b) NbC. Thermodynamic equilibria calculated by [TCFE5 05] are given on the figure.

$$I = \sum_i N_i(D) \Delta D \quad (4.6)$$

In order to have a good visualization of the type of growth (abnormal vs normal) these distribution are “in volume”, i.e.: instead of number density, grain volume density ( $NR^3$ ) are used to give a more representative weight to large abnormal grains. With this representation, a wide distribution exhibiting an important part of volume of matter due to large grains is characteristic of AGG, whereas a narrow gaussian-like distribution is related to normal grain growth. We can see in figure 4.3 that there is no grain growth for treatments at 900°C, whereas, at 1050°C we observe an AGG for all treatments. These results indeed confirm the tendency deduced by eye from experimental observations of microstructures after a Béchét-Beaujard etching.

### 4.3.2 Industrial steel 16MnCr5+Nb

#### 4.3.2.1 Precipitate size distribution

Figure 4.5 shows the normalized precipitate size distributions  $N_n$  for the *As Rolled* and *Iso* states. The mean radius of precipitates for *As Rolled* state is much larger than for the *Iso* state. This is due to the isothermal annealing, which allows a dissolution of precipitates at 950°C and a new precipitation at 600°C, leading to a fine precipitation. The *Iso* state presents a bimodal distribution, for which the notion of mean radius is irrelevant. This bimodal distribution is due to the precipitation of fine Nb-rich particles during the isothermal annealing. Finally, there are much more precipitates in the *Iso* state than in the *As Rolled* state.

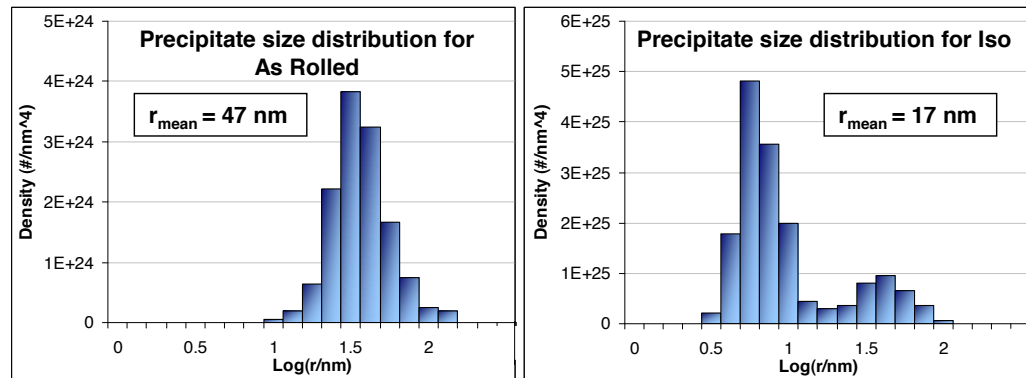


Figure 4.5: *Experimental precipitate size distributions for the As Rolled and Iso states in the industrial steel 16MnCr5+Nb.*

#### 4.3.2.2 Volume fraction

In this steel we observed two types of precipitates: Nb-rich and Al-rich precipitates. Figure 4.6 presents the evolution of volume fraction of both types for the *As Rolled* and *Iso* states before and after heat treatment at 1100°C. We observe an increase of the volume fraction for Al-rich and Nb-rich precipitates after the heat treatment for the *As Rolled* state, while there is no evolution for *Iso* state. After a treatment of 1 hour at 1100°C the volume fraction is nearly identical for all families in both *As Rolled* or *Iso* state.

#### 4.3.2.3 Austenitic grain size distribution

Figure 4.7 presents the austenitic grain size distributions for *As Rolled* and *Iso* states after a treatment at 1100°C during 1 hour. We observe an AGG for *As*

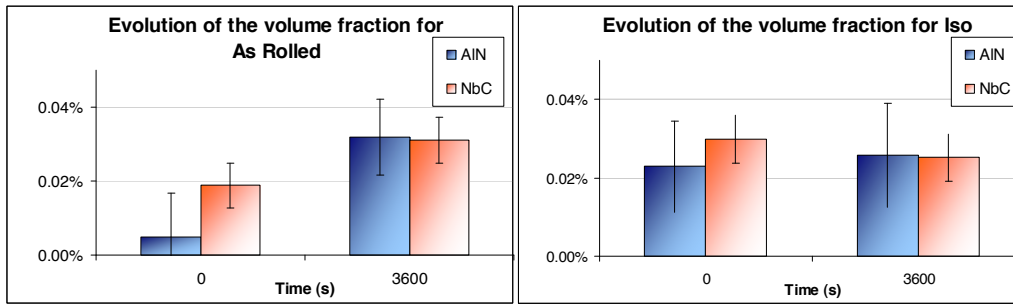


Figure 4.6: Evolution of volume fraction of AlN and NbC before and after 1 hour at 1100°C

*Rolled* state while for *Iso* state there is no grain growth<sup>1</sup>. This is certainly due to the precipitation state prior to any heat treatment: we indeed observed a larger volume fraction of fine precipitates in the *Iso* state than in the *As Rolled* state, which most probably leads to a more efficient pinning.

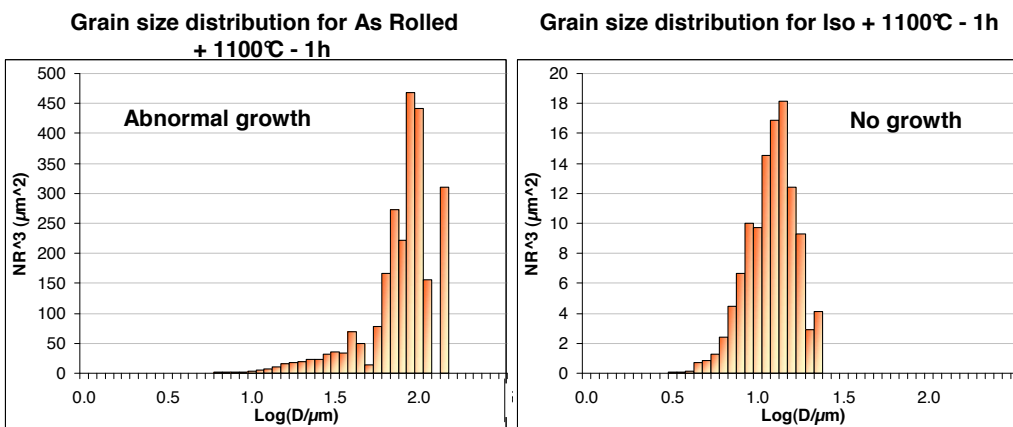


Figure 4.7: Experimental grain size distributions for both *As Rolled* and *Iso* state after a treatment at 1100°C during 1 hour. The kind of grain growth is as indicated on both graphs.

<sup>1</sup>In chapter 3 we have seen that the PAGS of the *Iso* state at 1100°C is similar to that of the initial state.

## 4.4 Heterogeneous model for pinning

### 4.4.1 Model description

In this section we present the equations of a heterogeneous pinning model developed by Bréchet and Militzer [Bréchet 05]. They assumed that there are two kinds of precipitate locations for pinning grain boundaries: (i) the interface between two grains (leading to the Zener-type pinning pressure); (ii) the corner points (or quadruple points). It is important to note that precipitates have a better pinning efficiency in the latest location, which can be easily understood for geometrical reasons (figure 4.8).

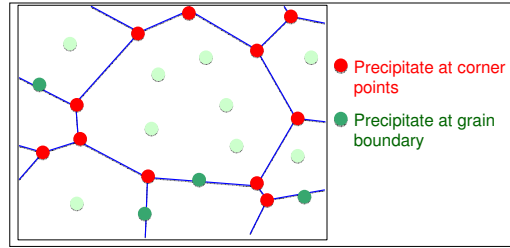


Figure 4.8: Schematic representation of different location types for precipitates in a polycrystalline material. Spheres in red represent precipitates, which pin corner points, and green ones are for precipitates pinning grain boundaries.

The pinning pressure  $f_z$  for one precipitate located on a grain boundary is given by equation 4.2. From this equation and the expression of the number density  $n$  of obstacles (equation 4.3), the pinning pressure  $F_Z$  can be expressed as:

$$F_Z = 2r \cdot n \cdot f_z = \frac{2k_s}{k_v} \frac{f\gamma}{r} \quad (4.7)$$

where  $k_s$  and  $k_v$  are geometric factors (see equations 4.2 and 4.3),  $\gamma$  is the precipitate/matrix or matrix grain boundary interfacial energy,  $f$  is the precipitate volume fraction and  $r$  the mean radius of precipitates.

According to Bréchet and Militzer, if precipitates are located on quadruple points the pinning pressure for one precipitate  $f_z$  is increased by a factor  $\alpha_o$ :

$$f_z^* = \alpha_o f_z \quad (4.8)$$

$\alpha_o$  is thus an amplification factor due to the better efficiency of such locations. The number of these quadruple (corner) points  $N^*$  per unit volume is a function of grain size  $D$ :

$$N^* = \frac{K_o}{K_V D^3} \quad (4.9)$$

where  $K_o$  is the average number of quadruple points per grain and  $K_V$  is a geometric constant describing the grain shape. Each grain has a boundary area obviously proportional to its mean diameter  $D$ , that we will then write as  $K_A D^2$  with  $K_A$  another geometric constant.  $K_V$  and  $K_A$  are based on an average volumetric grain size. Realistic values for these parameters will be given later (see table 4.3). The expression for the pinning pressure  $F_p$  per unit area depends on whether the number density of precipitates  $n$  is smaller or larger than  $N^*$ .

If  $n < N^*$ , (i) there are more corner points than available precipitates and (ii) all corner points are preferentially located on a precipitate. We then have:

$$F_p = \frac{n \alpha_o f_z K_o}{N^* K_A D^2} \quad (4.10)$$

If  $n > N^*$ , (i) there are more precipitates than corner points, (ii) all corner points are pinned by precipitates and (iii) resulting precipitates are involved in classical Zener-type pinning. Giving thus:

$$F_p = \frac{\alpha_o f_z K_o}{K_A D^2} + (n - N^*) 2r f_z \quad (4.11)$$

In the second regime ( $n > N^*$ ), as  $F_p$  decreases when  $D$  increases, large grains may be less efficiently pinned than smaller grains leading to an instability that may provide a mechanism for AGG onset. Consequently a simple expression for the growth rate  $\dot{D}$  is given by:

$$\dot{D} = \begin{cases} M(F - F_p) & \text{if } F > F_p \\ 0 & \text{if } F < F_p \end{cases} \quad (4.12)$$

Here  $M$  is the grain boundary mobility. A simple criterion for AGG may be that the growth rate increases with grain size, thus any initially large grain will tend to always become larger. In this case:

$$\frac{\partial}{\partial D}(\dot{D}) > 0 \quad (4.13)$$

In conclusion:

- if  $\dot{D} = 0$ , there is no grain growth
- if  $\dot{D} > 0$  and  $d\dot{D}/dD > 0$ , there is a risk of AGG

- if  $\dot{D} < 0$  and  $d\dot{D}/dD < 0$  there is normal grain growth

This particular scenario is explained by figure 4.9, where the pinning pressure is plotted versus the ratio of austenitic grain size over mean precipitate radius. The pinning pressure increases with the grain diameter  $D$  until all “corner points” are pinned by precipitates (points 1 and 2 on the figure). Then, as  $D$  increases, some precipitates will have a Zener type pinning pressure and the total pinning pressure will decrease (points 3 on the figure) until the “corner points” type pinning pressure becomes negligible compared to the Zener type pinning pressure (when the pinning pressure is equal to the Zener type pinning pressure).

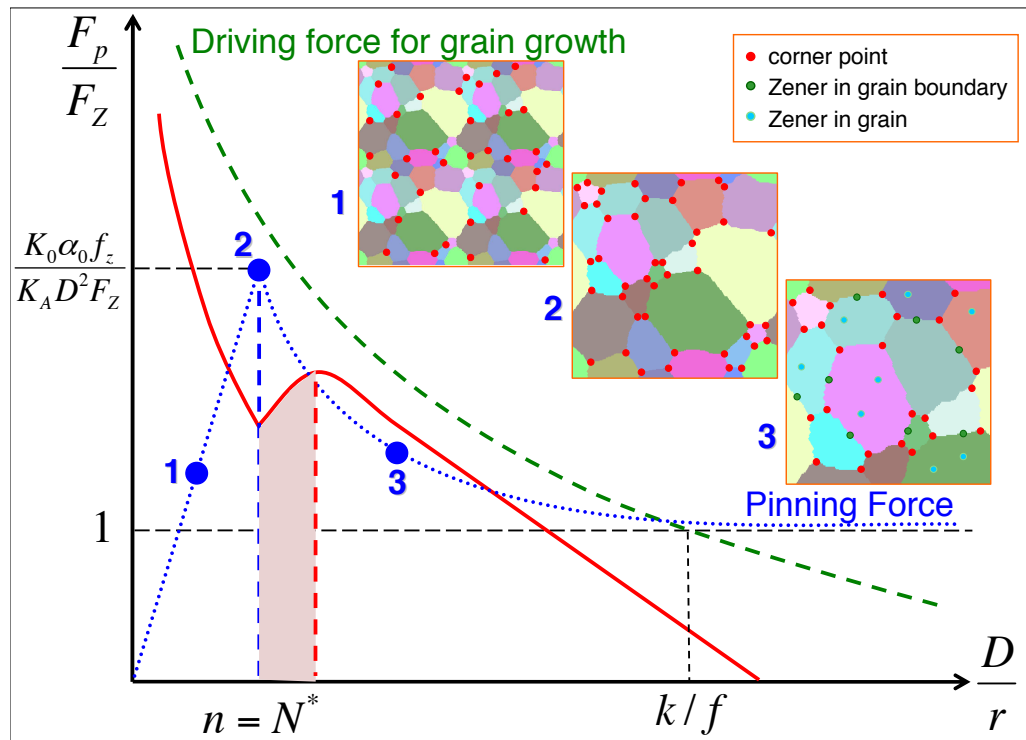


Figure 4.9: Schematic representation of the evolution of the driving pressure for grain growth (green curve, heavy dotted line), the pinning pressure of precipitates (blue curve, light dotted line) and the growth rate (red curve, full line). The first part of blue curve (point 1) corresponds to the pinning of some corner points by precipitates, then, if all corner points are pinned, the pinning pressure reaches its maximum (point 2). Finally, some grain boundaries start to be pinned and the pinning pressure decreases until reaching the Zener pinning pressure (point 3). The instability region (shaded in red under the curve) is characteristic of a risk of AGG.

In conclusion, this model can predict the onset of a large grain in a matrix composed by small grains and describes the risk of AGG as a consequence of an instability.

#### 4.4.2 Comparison with experiments

In order to compare results obtained with the heterogeneous pinning model and experimental results, we used the same set of parameters (table 4.3) as in [Bréchet 05], except for  $\alpha_o$ , which is considered to be adjustable (from 1 to 6).

	Values
$K_V$	$(1.1)^3 \pi / 6$
$K_A$	$(1.1)^2 \pi / 2$
$K_o$	5
$k_v$	$4\pi / 3$
$k_s$	$\pi$
$\gamma$	0.5

Table 4.3: Values of constants for equiaxed grains and spherical precipitates from [Bréchet 05].

Figure 4.10 shows results on the FeVNbCN alloys. On figure 4.10.a) we can observe after 200 minutes at 900°C an homogeneous structure, which means that normal growth occurs. However, as observed in figure 4.10.c), the model predicts a risk of AGG. Note that, in this particular case, we do not have a real disagreement since the model only predicts a risk of AGG. The situation is different for the case of a treatment of 20 minutes at 1050°C. The micrograph of figure 4.10.b) clearly evidences AGG, whereas the model does not predict any risk of AGG. The model was tested with several amplification factor  $\alpha_o$ , none of them giving satisfactory agreement for any heat treatments. This model is therefore in disagreement with our experimental results (considering that a unique amplification factor should apply for all conditions). For these calculations, the amplification factor  $\alpha_o$  has been fixed to 3, the choice of this value will be explained later.

There are two arguments to explain these discrepancies. The first one is the shape of the precipitate size distribution. If there is a bimodal distribution, i.e. two types of particles (some very large particles and a lot of small particles), the calculation of the precipitate average radius is meaningless. The second argument lies in the calculation of precipitates number density  $n$ : (i) if equation

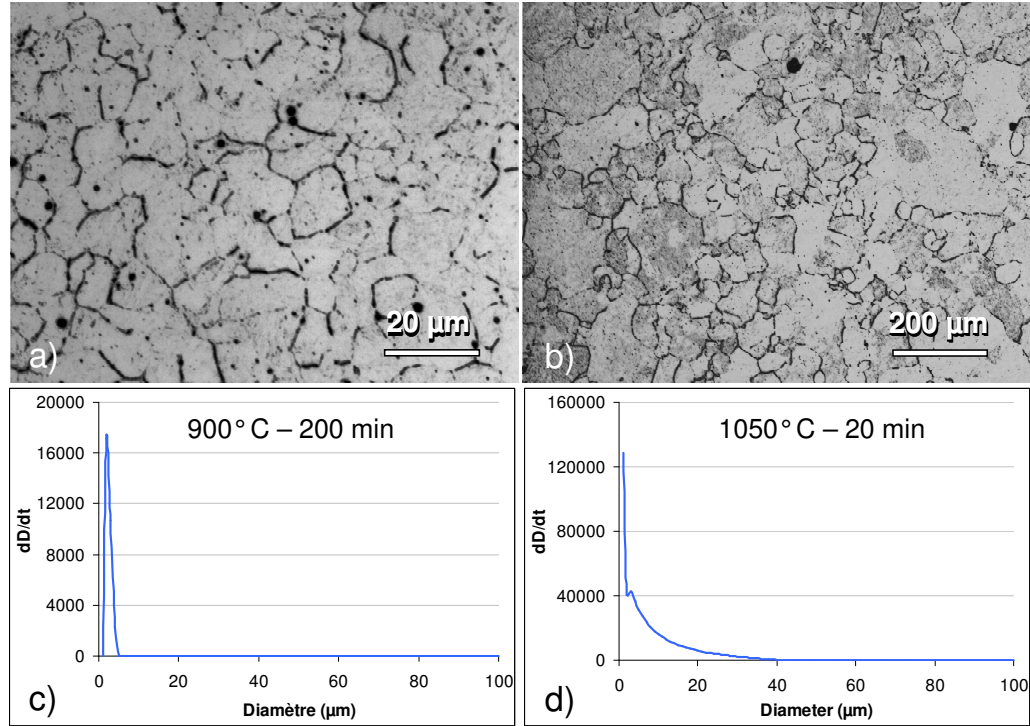


Figure 4.10: Comparison between experimental results and the model of Bréchet and Militzer. *a* and *b*: Optical micrographies obtain after Béchét-Beaujard etching for FeVNbCN alloy treated at 900°C during 200 minutes and 1050°C during 20 minutes respectively; *c* and *d*: growth rates obtained for these treatment respectively. As it can be seen, both calculation and experiments are not in perfect agreement, especially for the treatment at 1050°C.

4.3 is used,  $n$  is calculated from the precipitate mean radius, (ii) if one accounts for the precipitate size distribution,  $n$  is then calculated from:

$$n = \sum_i (N_n(r_i) \Delta r) \quad (4.14)$$

Where  $N_n(r_i)$  is the number density of precipitate in the class  $i$  and  $\Delta r$  the width of each class. Figure 4.11 presents the size distribution of precipitates for the FeVNbCN alloy treated at 1050°C during 20 minutes. The average radius of precipitates and the calculated values of  $n$  (with both the distribution equation 4.14 and the averaged radius equation 4.3) are shown on the figure. As we can see, these two numbers are different by two orders of magnitude.

Note that running the previous model (equation 4.12) with a more realistic number of particles  $n$  (measured from precipitate size distributions and volume fraction  $f$ ) does not lead to a better agreement. Therefore, it is

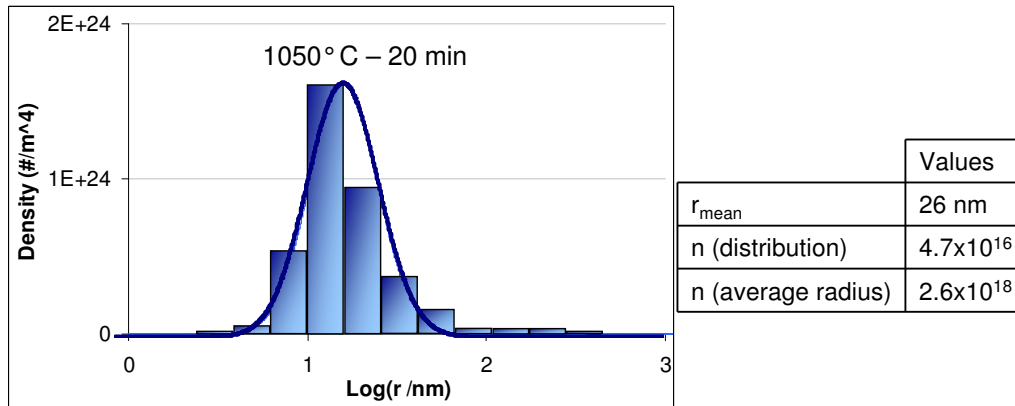


Figure 4.11: Size distribution of precipitates for FeVNbCN alloy treated at 1050°C during 20 minutes. The mean radius, and the number of precipitates (calculated from the distribution or from the average radius) are indicated on the figure.

necessary to improve the model, which is the aim of the next section, in which we will propose a new criterion for AGG.

## 4.5 A new criterion for abnormal grain growth

### 4.5.1 The model

In this model, we suppose that “corner points” are pinned preferentially by big particles because (i) larger particles have a larger pinning pressure and (ii) pinning efficiency is increased at corner points. Figure 4.12 represents the cumulative precipitate distribution showing the two different pinning types. To evaluate the total pinning pressure, we incorporate the size distribution (using equation 4.14) into equations 4.10 and 4.11, then we assume (i) that large particles (with class index  $i$  larger than a critical value  $i^*$ ) have a “corner points”-type pinning pressure (giving by equation 4.10), and (ii) that small particles (with class index  $i$  smaller than  $i^*$ ) have a Zener-type pinning pressure (giving by equation 4.11). The class index  $i^*$  is defined by:

$$\sum_{i < i^*} N_n(r_i) \Delta r < N^* \text{ and } \sum_{i \geq i^*} N_n(r_i) \Delta r > N^* \quad (4.15)$$

Precipitates in this class are divided into two parts such as:

$$\begin{cases} N_n(r_{i^*}) = N_n(r_{i^*})^c + N_n(r_{i^*})^Z \\ \sum_{i>i^*} N_n(r_{i^*}) + N_n(r_{i^*})^c = N^* \end{cases} \quad (4.16)$$

Here,  $N_n(r_{i^*})^c$  and  $N_n(r_{i^*})^Z$  are numbers of precipitates in class  $i^*$ , which have a corner points-type pinning and a Zener-type pinning respectively. We find, for each class  $i$ :

for  $n < N^*$

$$F_p = \sum_i \frac{N_n(r_i)\Delta r}{N^*} \frac{\alpha_o f_z(r_i)K_o}{K_A D^2} \quad (4.17)$$

for  $n > N^*$

$$F_p = \sum_{i \geq i^*} \frac{\alpha_o f_z(r_i)K_o}{K_A D^2} + \sum_{i \leq i^*} N_n(r_i) 2r_i f_z(r_i) \quad (4.18)$$

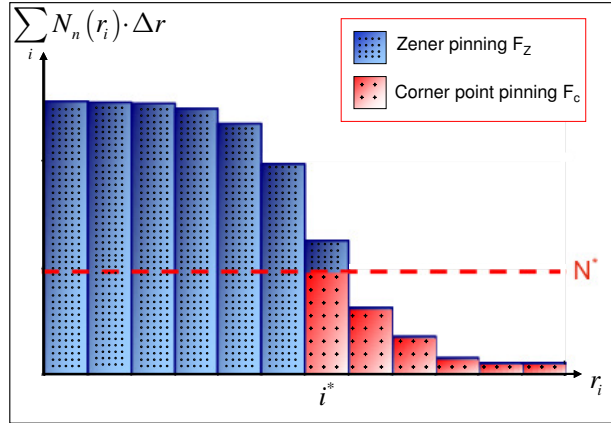


Figure 4.12: *Integration of the size distribution (starting from the end). In this graph, the red part on the right corresponds to particles, which pin “corner points”, and the blue part on the left corresponds to particles, which have a Zener-type pinning pressure. The class  $i^*$  is divided into two parts: Zener and corner points pinning types.*

Figure 4.13 shows the importance of taking into account the whole precipitate size distribution. Indeed, we can compare the model prediction for two precipitate size distributions, which lead to the same precipitate mean radius and volume fraction (figures 4.13.a and c). In the first case there is no risk of abnormal grain growth (see figure 4.13.b), but changing the width

of the distribution (second case) leads to a risk of AGG (see figure 4.13.d). Hence, the “shape” of the precipitate size distribution has a great influence on the grain growth behaviour.

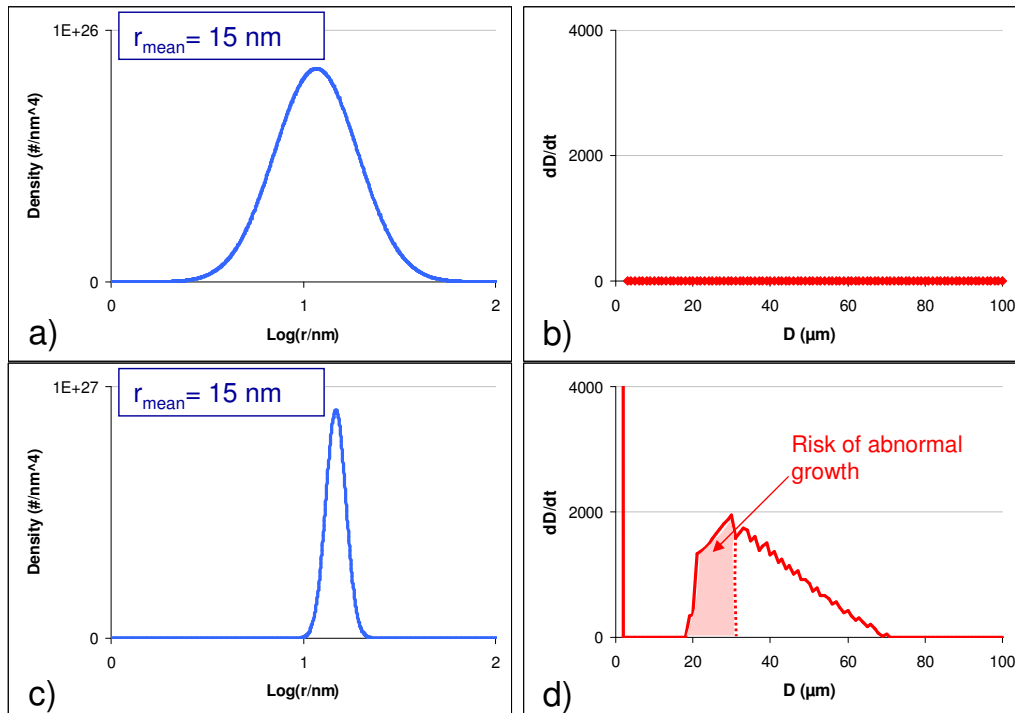


Figure 4.13: a) and c): Example of two precipitate size distribution with the same precipitate average radius and same volume fraction, but with different widths. b) and d); Prediction of the model for these distributions. In the second case there is a risk of AGG.

#### 4.5.2 Comparison with experiments

The model has been tested first on the model alloy FeVNbCN. The amplification factor  $\alpha_0$  have been adjusted to 3 to get the best possible agreement with experiment. Note that, simple geometrical considerations given in [Bréchet 05] would suggest a value of 2. All others parameters were chosen identical to those of [Bréchet 05] (see table 4.3).

All states of the FeVNbCN alloy presented in paragraph 4.3 were treated with this model. Figure 4.14 shows an optical micrograph of normal austenitic grains and the prediction of the model with the precipitate size distribution for the treatment at 900°C during 2 minutes. The model predicts a total

locking of all grain boundaries, leading to the absence of grain growth (as long as precipitate state remains like this), which is consistent with the observation.

Figures 4.15 and 4.16 present results for the FeVNbCN alloy after heat treatments at 900°C and 1050°C respectively. At 900°C during 20 and 200 minutes the precipitate state is very similar to the “First State” (900°C - 2 minutes). Figures 4.15.b and d present optical micrographs without grain growth, and the model in figures 4.15.a and c predicts a blocking of all grains. However, after a heat treatment at 1050°C during 2, 20 or 200 minutes the precipitate state has changed (see section 4.3) and the model predicts an AGG (figures 4.16.a, c and e), which is consistent with the experimental observations (figure 4.16.b, d and f).

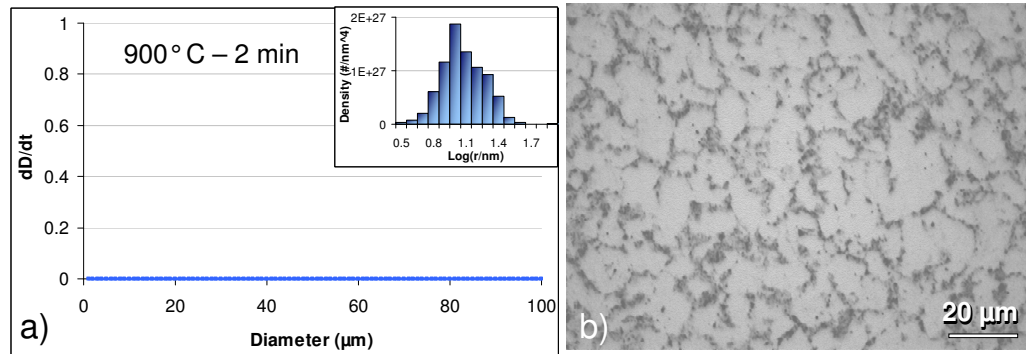


Figure 4.14: Comparison between experimental results and the model. *a*: Growth rate obtained for the “first state” and precipitate size distribution; *b*: Optical micrograph obtained after Béchet-Beaujard etching for FeVNbCN alloy treated at 900°C during 2 minutes. There is a good agreement between the model, which predicts an inhibition of the grain growth, and the experimental results.

Table 4.4 is a summary of experimental results (in terms of grain growth) and model predictions. The Bréchet and Miltzer model [Bréchet 05] is not in total agreement with experiments, while a model, which takes into account the whole precipitate size distribution gives good predictions for all investigated treatments. Furthermore, this approach could be associated to a precipitation model in order to evaluate the risk of AGG during a thermal treatment (i.e. when precipitation state evolves).

From the above, it is seen that this model can predict the risk of AGG, by describing the onset of this phenomenon. It is actually not valid to predict if the abnormal grains are large enough to continue growing faster than their neighboring smaller grains. To do so, the complementary model of

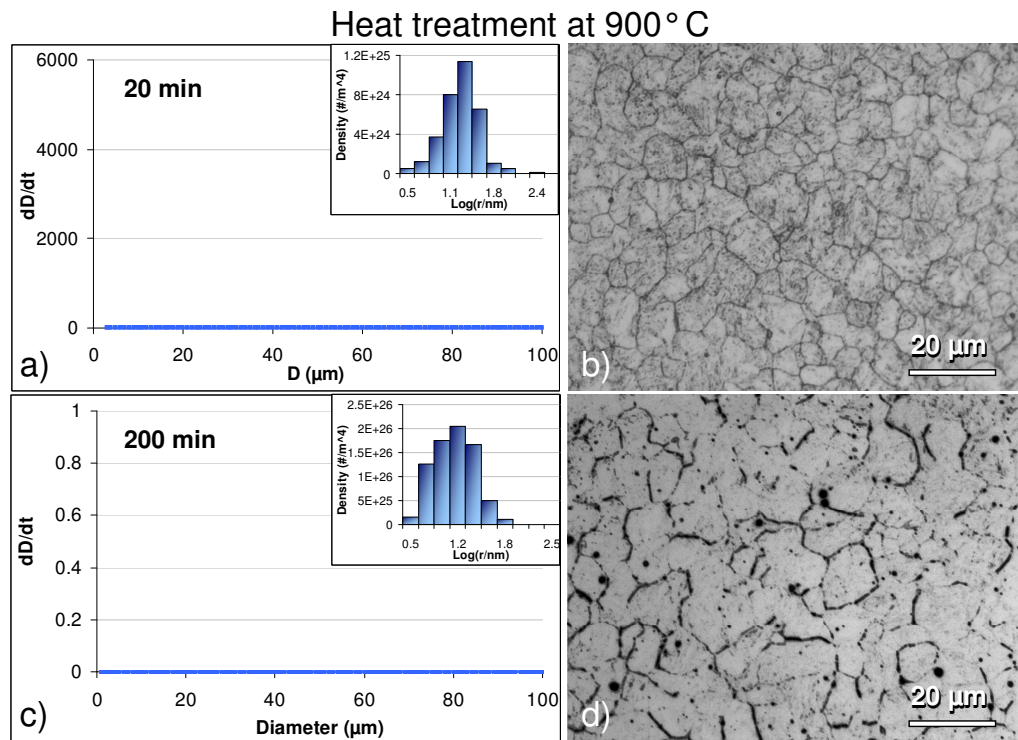


Figure 4.15: Comparison between experimental results and the model for heat treatments at 900°C. a and c: Growth rate obtained after 20 minutes and 200 minutes; b and d: Optical micrographs obtained after Béchot-Beaujard etching for these treatments. There is a good agreement between the predictions of the model and the experimental results.

Andersen *et al.* [Andersen 95a] describes the stability of an existing large grain surrounded by smaller grains. In other words, Andersen’s model deals with the propagation of AGG, whereas ours aims at describing the onset of AGG.

In table 4.5, we compare the maximum size of the abnormal grain resulting from our approach (i.e. the diameter at which  $\dot{D}(D)$  is maximum), with the Andersen’s minimum size of an existing large grain necessary to the propagation of AGG. It seems that the size of the abnormal grain predicted by our model corresponds approximatively to the size, from which AGG does not need any particle to progress, which is in agreement with experimental observations.

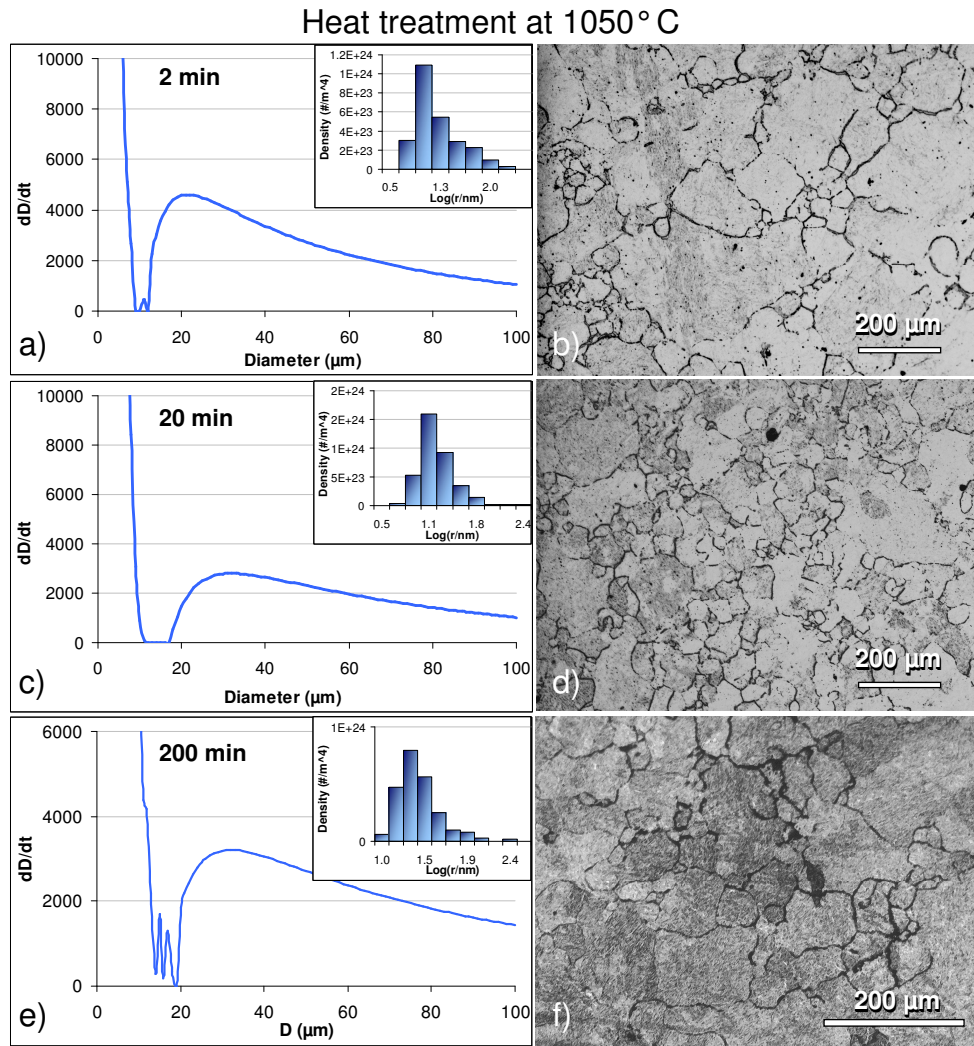


Figure 4.16: Comparison between experimental results and the model for heat treatments at 1050°C. a), c) and e): Growth rate obtained after 2 minutes, 20 minutes and 200 minutes; b), d) and f): Optical micrographs obtained after Béchét-Beaujard etching for these treatments. There is a good agreement between the predictions of the model and the experimental results.

## 4.6 Application to the industrial steel: 16MnCr5+Nb

We will now discuss on the industrial steel, the 16MnCr5+Nb alloy. Recall that after a treatment at 1100°C during 1 hour we observe two kinds of grain growth:

- AGG after this treatment on the *As Rolled* state (see figure 4.17.c)

treatments	No growth/Normal/ Abnormal ? [Bréchet 05]	No growth/Normal/ Abnormal ?	Experience
900°C-2min	No growth	No growth	No growth
900°C-20min	Abnormal	No growth	No growth
900°C-200min	Abnormal	No growth	No growth
1050°C-2min	Normal	Abnormal	Abnormal
1050°C-20min	Normal	Abnormal	Abnormal
1050°C-200min	Normal	Abnormal	Abnormal

Table 4.4: Results for all treatments concerning the FeVNbCN steel. in each case the predicted (first two columns) and observed (last columns) microstructures are characterized.

treatment	$\bar{D}/D_{lim}$	$D_{ab}$ [Andersen 95b]	$D_{ab}$
1050°C - 2 min	0.25	26 $\mu$	21 $\mu$
1050°C - 20 min	0.65	45 $\mu$	32 $\mu$

Table 4.5: Comparison between the size of the abnormal grain  $D_{ab}$  necessary to have an AGG according to [Andersen 95b] and the size of the abnormal grain predicted by the present model.  $\bar{D}$  is the experimental mean diameter of grain and  $D_{lim}$  the diameter calculated with the equation  $D_{lim} = \lambda r / f$  with  $\lambda = 1/4$  [Rios 87]. Abnormal sizes of grains are very similar.

- no grain growth after this treatment on the *Iso* state (see figure 4.17.d)

Figures 4.17.a) and b) present predictions of the model for the alloy at initial *As Rolled* and *Iso* states respectively, using the same parameters as in the case of the FeVNbCN steel. In all cases there is a risk of AGG when we consider both *As Rolled* and *Iso* states without further treatment, but only *As Rolled* state presents an AGG after heat treatment. However, we observe on figure 4.17.b) that large grains, that could eventually grow considering large versus small grains instability (treated by [Andersen 95a]), will be pinned by precipitates, since the pinning pressure is much larger than the driving pressure for large grains. Moreover, if the treatment is longer, AGG will occur, as it has been observed for a 10 hours treatment at 1100°C.

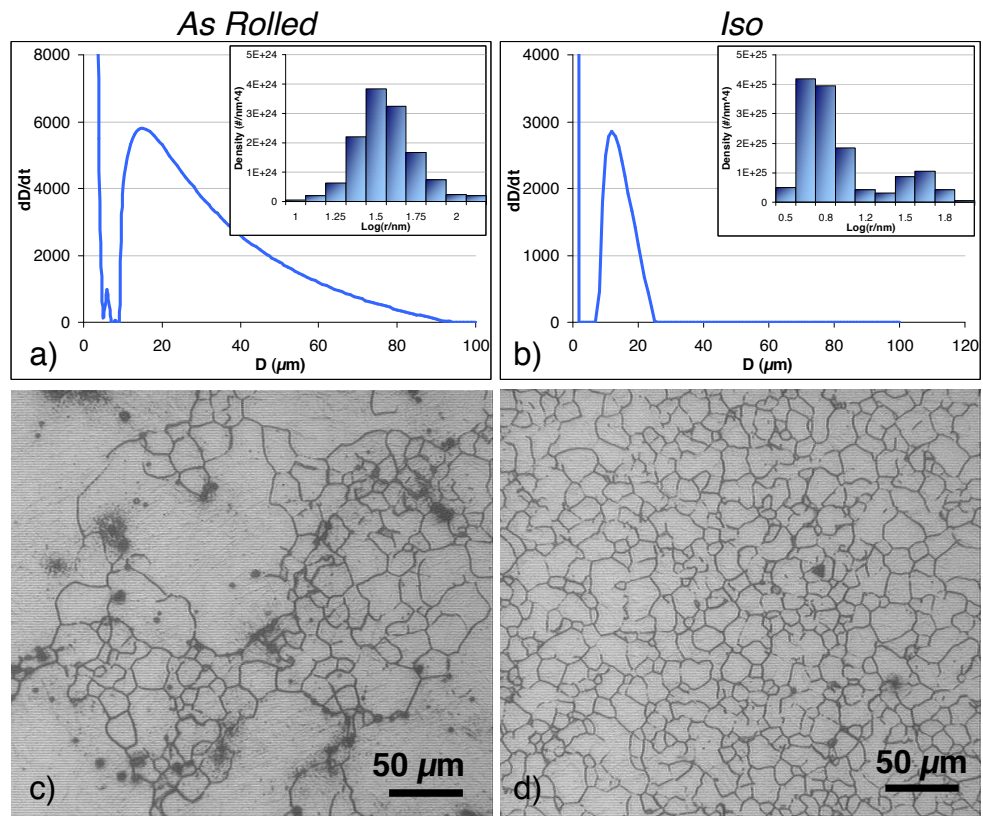


Figure 4.17: Comparison between prediction of the model and experimental observations. a) and b): Prediction of the model for As Rolled and Iso states respectively. c) and d): Optical micrographies of As Rolled and Iso states after a treatment at 1100°C during 1 hour respectively.

## 4.7 Conclusion of the chapter

In the present investigation the most important points are:

- When large grains grow faster than small grains, AGG may occur.
- There is AGG only if an onset exists (apparition of large grains surrounded by smaller ones), and, then, if this onset propagates (faster growth of larger grains than smaller ones).
- In this chapter a model for predicting the existence of such an onset has been proposed on the basis of a 'thermodynamical' accounting for special locations for the pinning particles (quadruple or corner points vs grain boundaries). To be correct, the treatment further requires to consider the whole precipitate size distribution.

- Only one parameter (the amplification factor  $\alpha_o$ ) have been adjusted. Results of the proposed model are in good agreement with experiments for all treatments performed on FeVNbCN and 16MnCr5+Nb steels with a unique value of  $\alpha_o$ .

This approach could be fruitfully combined with a precipitation model (see Chapter 2) in order to monitor the risk of AGG through thermal treatment, during which the precipitation state does evolve. Such a model enables to know the risk even in cases where heat treatments could not be performed.

## Conclusion and Perspectives

This work is integrated into a larger project, which started several years ago at MATEIS with A. Bogner's Master thesis and was followed by D. Acevedo's PhD thesis [Acevedo 07]. The general aim of this project is to provide a better understanding of the relationship between the thermo-mechanical treatments performed on Ascometal steels and their Prior Austenitic Grain Size (PAGS), which itself, is highly correlated with final mechanical properties (fatigue, yield, strength, ...).

At first, the main results and conclusions of this work will be recalled. Then, some possible prospects will be proposed.

### Main results

One of the main interests of this work was to finely characterize the precipitation state of steels containing both carbon and nitrogen. Thus, we needed a method to quantify these elements within precipitates. Indeed, EDX is not suitable to measure light elements. Therefore, Electron Energy Loss Spectroscopy (EELS) has been used. However, no adequate methods to treat EELS spectra of complex carbonitrides such as (Nb,V,Ti)(C,N) were found in the literature. A routine, based on the Least Mean Square Fitting (LMSF) method, has been implemented in order to treat such spectra. This technique gives good agreements with EDX analysis for metallic elements, which brings some further credibility to the method when applied to interstitial light elements. Finally, this routine brings further information on (Nb,V,Ti)(C,N) core-shell type structures in the 60SiCrV7+Nb industrial steel, where an enrichment in titanium and nitrogen is observed in the core of these particles.

In order to understand the influence of the nitrogen on the precipitation state, a FeVNbCN model alloy has been elaborated. This alloy presented a small undesirable titanium content, probably not enough to form core-shell

structures with a TiN rich core (as it was observed for the 60SiCrV7+Nb industrial steel). EDX analysis have shown the presence of two kinds of precipitates, V-rich and Nb-rich particles. For all observed states, the mean radius of V-rich particles is systematically higher than that of Nb-rich precipitates. EELS analysis performed on these particles reveal that the Nb-rich precipitates are NbC carbides whereas, V-rich precipitates are V(C,N) carbonitrides. Moreover, experimental results show that vanadium carbonitrides present an enrichment in nitrogen with the increase of the treatment temperature, thus is probably due to the selective dissolution of the carbon. Except for the particles chemistry, comparison of the precipitation state between the FeVNbCN model alloy and the 60SiCrV7+Nb industrial steel does not reveal significant difference. However, only few results have been compared, hence the conclusion on this point is delicate

A model based on classical nucleation and growth theories was implemented in the software PreciSo [Acevedo 07]. It takes into account two precipitate types:  $VC_xN_y$  and NbC. A comparison between predictions for the various  $V_6C_5$ , VN and  $VC_xN_y$  shows that precipitates containing nitrogen are more stable and thus dissolve slower.

The correlation between the precipitation state and the prior austenite grain size evolution was obtained for both the industrial steel (16MnCr5+Nb gear steel) and the FeVNbCN model alloy. This correlation shows that there is no influence of the precipitate chemistry on the control of the prior austenite grain size, as observed in the literature, but only an influence of the volume fraction and of the precipitate size distributions. The implementation of a simple grain growth model into the precipitation model, in which the precipitation state evolves, shows that the austenitic grains start to grow when the ratio  $f/r$  ( $r$  is the mean precipitate radius and  $f$  the precipitate volume fraction) of  $VC_xN_y$  strongly decreases.

Finally, a criterion to predict a risk of Abnormal Grain Growth (AGG) was proposed. It is based on Bréchet and Miltzer's model [Bréchet 05], but unlike their model, the whole precipitation size distribution is taken into account. Thus, for a given precipitation state (size distribution and volume fraction), we can predict if there is a risk that abnormal grain growth occurs. The predictions obtained with the model give a good agreement with experimental results for both the 16MnCr5+Nb industrial steel and the model alloy.

## Prospects

### Cross checking results from both thesis

At this stage, many experimental results have been accumulated since the beginning of D. Acevedo's PhD. It would be interesting to synthesize all these results. Note that this review is not straightforward, since thermo-mechanical treatments that have been performed, were not standardized: e.g. isothermal treatments, temperatures and durations were different.

First, an experimental comparison of the precipitation state between the FeVNbCN and the FeVNbC [Acevedo 07] model alloys would allow us to have a better understanding of the influence of nitrogen. Furthermore, the comparison between the model alloy and the 60SiCrV7+Nb industrial steel has shown that a sufficient addition of titanium leads to the formation of core-shell structures with a richer core in nitrogen and titanium. Thus, it will be interesting to elaborate a model alloy based on the FeVNbCN grade by adding a consistent amount of titanium. Then, it will be interesting to perform long heat treatments in order to understand the coarsening of core-shell structures. EELS would thus be needed to control the presence of nitrogen in the particle core.

### Precipitation modelling

The precipitation model needs to be improved to get a better agreement with experimental results. A few tracks are given in the following:

- Chemical analysis of precipitates have shown that particles are more (Nb,V)(C,N) than Nb(C,N) and/or V(C,N). Hence, it is necessary to model the evolution of complex (Nb,V)(C,N) precipitates.
- Moreover the model has to take into account the titanium and the aluminium to predict the evolution of the precipitation state in a FeVNbTiCN model alloy and in the 16MnCr5+Nb industrial steel.
- Core-shell structures have to be considered in the modelling of the precipitation state reversion. To do this, the model would have to keep in memory the composition profile for each precipitate class.
- Instead of starting with solubility products of the literature, the model could be fed by thermodynamic databases, such as TCFE5.

Furthermore, the model could be favourably used to compare the evolution of the precipitation state of several steels. In particular, that of the FeVNbC (elaborated during D. Acevedo's PhD) and FeVNbCN model alloys, for which treatment temperatures and durations were different.

### Thermo-mechanical treatment simulations

The elaboration of special steels involves complex thermo-mechanical treatments. However, all treatments performed in this work do not involve any mechanical solicitations. Therefore, it would be interesting to perform mechanical treatments during austenitizing in order to study the influence of the deformation on the precipitation state. This could be realized in the "Geeble" thermo-mechanical simulator recently acquired in MATEIS group. The prior austenite grain size and the precipitation state could be evaluated for several treatments with variable parameters (temperature, strain rate, ...). This experimental study could provide a better understanding of the precipitation state and prior austenite grain size evolution during real industrial treatments. A model could be then implemented to take into account the evolution of the precipitation state during such treatments. And finally, this approach could be fruitfully coupled with a model predicting austenitic grain size.

### Modeling grain growth

Regarding the austenitic grain growth, a more complex model combining a precipitation model and the criterion of abnormal grain growth would predict the risk of abnormal grain growth through thermal treatment, during which the precipitation state evolves.

In the literature, the evolution of prior austenite grain size has been studied and modelled at the many different scales. Among them:

- Works of Elizabeth Holm and co. *et al.* show that molecular dynamics simulations could be used to determine the energies and mobilities of grain boundaries.
- Rollett *et al.* have modelled the kinetics of grain growth in presence of fine particles by Monte Carlo simulation [Rollett 92]
- The Vertex method was fruitfully used by Weygand *et al.* [Weygand 99] to model the particle-inhibited grain growth in two dimensions.
- Phase Field simulations are frequently used to model the interaction between austenitic grains and precipitates. We can cite for example the

works of Militzer *et al.*.

It would be interesting to review all these modelling approaches. Then, a grain growth model fed by PreciSo (precipitation model) could be developed. This is a difficult task: in particular the choice of the simulation methods (Molecular Dynamics, Monte Carlo, Phase Field, Vertex and analytical approaches), or the optimization of the dialog between different techniques and scales, is a great material sciences challenge.

### **Characterizing of grain growth**

Characterizing the prior austenite grain size through etching and optical analysis is time consuming and provides only 2D information. Laser-ultrasonics for metallurgy (LUMet), an emerging technology could provide a non-destructive technique for fast and precise measurements of microstructures. Laser-ultrasonics is the generation and detection of ultrasound using lasers. A first laser generates an ultrasound pulse, which travels inside the metal and interacts with the microstructure. Another laser coupled to an interferometer detects the ultrasound pulse at some later time. An analysis of the detected ultrasonic pulse provides the microstructure information. The system has been demonstrated to provide measurements of Young's moduli, Poisson's ratio, texture, recovery and recrystallization, grain size, phase transformations and internal friction. By installing it on a Gleeble thermo-mechanical simulator or on a pilot scale line, the LUMet can do those measurements in-situ to characterize almost any thermo-mechanical process. LUMet has many advantages as compared to other metallurgical measurements. In particular the in-situ measurement of the prior austenite grain size in low carbon steels, which cannot be done in any other way. A project is already underway at the University of British Columbia to perform in-situ metallurgical measurements on various steels.

### **TEM characterization**

Some interesting features were found during the course of the present microstructure investigations by TEM.

One concerns the core-shell precipitates in the 60SiCrV7+Nb industrial steel. Although, our EELS analysis has provided some data on such structures, we could not confirm the presence of pure TiN in the core as it was observed elsewhere. Indeed, all measured performed in the core are "polluted" by the

contribution of the precipitate shell lying over and below the core. To follow the evolution of these core-shell structures and, in particular, to determine the exact composition of the core, a geometrical model, accounting for the exact position of the probe on the precipitate and the particle morphology, and thus enabling to separate the contribution due to the core to that of the shell, has to be refined.

In High Angle Annular Dark Field (HAADF) mode, the scattered intensity is theoretically proportional to the square of the atomic number  $Z$ . Thus, in our model alloys, which does not contain impurity, it would be possible to determine the precipitate chemistry only by greys level analysis, since the vanadium ( $Z = 23$ ) and the niobium ( $Z = 41$ ) have a quite different atomic number.

## Bibliography

- [Acevedo 07] D. Acevedo. *Evolution de l'état de précipitation au cours de l'austénitisation d'aciers microalliés au vanadium et au niobium*. PhD thesis, 2007.
- [Ahn 83] C. C. Ahn, O. L. Krivanek, R.P. Burgner, M.M. Disko & P.R. Swann. *EELS Atlas*. Rapport technique, Warrendale, PA: Gatan, Inc., 1983.
- [Andersen 95a] I. Andersen & O. Grong. *Analytical modelling of grain growth in metals and alloys in the presence of growing and dissolving precipitates. - I. Normal grain growth*. Acta Metallurgica and Materialia, vol. 43, pages 2673–2688, 1995.
- [Andersen 95b] I. Andersen, O. Grong & N. Ryum. *Analytical modelling of grain growth in metals and alloys in the presence of growing and dissolving precipitates. - II. Abnormal grain growth*. Acta Metallurgica and Materialia, vol. 43, pages 2689–2700, 1995.
- [Anderson 84] M.P. Anderson, D.J. Srolovitz, G.S. Grest & P.S. Sahni. *Computer simulation of grain growth - I. Kinetics*. Acta Materialia, vol. 32, pages 783–791, 1984.
- [Apel 09] M. Apel, B. Bottger, J. Rudnizki, P. Schaffnit & I. Steinbach. *Grain growth simulations including particle pinning using the multiphase-field concept*. ISIJ international, vol. 49, pages 1024–1029, 2009.
- [Baker 09] T.N. Baker. *Processes, microstructure and properties of vanadium microalloyed steels*. Materials Science and Technology, vol. 25, pages 1089–1107, 2009.

## BIBLIOGRAPHY

---

- [Banerjee 09] K. Banerjee, M. Perez & M. Militzer. *Non-isothermal austenite grain growth kinetics in a microalloyed X-80 pipeline steel*. Preprint submitted to Acta Materialia, 2009.
- [Barrales-Mora 09] L.A. Barrales-Mora. *2D vertex modeling for the simulation of grain growth and related phenomena*. Mathematics and Computers in Simulation, 2009.
- [Bréchet 05] Y. Bréchet & M. Militzer. *A note on grain size dependent pinning*. Scripta Materialia, vol. 52, pages 1299–1303, 2005.
- [Caifu 00] Y. Caifu, Z. Yongquan & L. Shuping. *Precipitation behavior of vanadium in V-N microalloyed rebar steels*. The Metallurgical Industry Press, pages 152–157, 2000.
- [Chang 09] K. Chang, W. Feng & L-Q. Chen. *Effect of second-phase particle morphology on grain growth kinetics*. Acta Materialia, vol. 57, pages 5229–5236, 2009.
- [Cliff 75] G. Cliff & G.W. Lorimer. *The quantitative analysis of thin specimens*. Journal of Microscopy, vol. 103, page 203–207, 1975.
- [Courtois 05] E. Courtois. *Etude de la précipitation des carbures et carbonitrures de niobium dans la ferrite par microscopie électronique en transmission et techniques associées*. PhD thesis, 2005. p.
- [Courtois 06] E. Courtois, T. Epicier & C. Scott. *EELS study of niobium carbo-nitride nano-precipitates in ferrite*. Micron, vol. 37, pages 492–502, 2006.
- [Craven 00a] A.J. Craven, K. He & L.A.J. Garvie T.N. Baker. *Complex heterogeneous precipitation in titanium-niobium microalloyed Al-killed HSLA steels - I. (Ti,Nb)(C,N) particles*. Acta Materialia, vol. 48, pages 3857–3868, 2000.
- [Craven 00b] A.J. Craven, K. He, A.J. Garvie & T.N. Baker. *Complex heterogeneous precipitation in titanium-niobium microalloyed Al-killed HSLA steels - II. Non-titanium based particles*. Acta Materialia, vol. 48, pages 3869–3878, 2000.

- [Crooks 81] M.J. Crooks, A.J. Garrat-Reed, J.B. Vander Sande & W.S. Owen. *Precipitation and recrystallisation in some vanadium and vanadium-niobium microalloyed steels*. Metallurgical Transaction A, vol. 12A, pages 1999–2013, 1981.
- [Cuddy 83] L.J. Cuddy & J.C. Raley. *Austenite grain coarsening in microalloyed steels*. Metallurgical Transactions, vol. 14A, pages 1989–1995, 1983.
- [Egerton 79] R.F. Egerton. *K-shell ionization cross-sections for use in microanalysis*. Ultramicroscopy, vol. 4, page 169, 1979.
- [Egerton 86] R.F. Egerton. *Eels in the electron microscope*. 1986.
- [Epicier 07] T. Epicier, D. Acevedo & M. Perez. *Crystallographic structure of vanadium carbide precipitates in a model Fe-C-V steel*. Philosophical Magazine, pages 1–15, 2007.
- [Erasmus 64] L.A. Erasmus. *Journal of Iron and Steel Institute*, vol. 292, pages 32–41, 1964.
- [Fernandez 07] J. Fernandez, S. Illescas & J.M. Guilemany. *Effect of microalloying elements on austenitic grain growth in a low carbon HSLA steel*. Materials Letters, pages 2389–2392, 2007.
- [Flores 97] O. Flores & L. Martinez. *Abnormal grain growth of austenite in a V-Nb microalloyed steel*. Journal of materials science, vol. 32, pages 5985–5991, 1997.
- [Frisk 08] K. Frisk. *Thermodynamic modelling of multicomponent cubic Nb, Ti and V carbides/carbonitrides*. Calphad, vol. 32, pages 326–337, 2008.
- [Fu 07] R.D. Fu, T.S. Wang, W.H. Zhou, W.H. Zhang & F.C. Zhang. *Characterization of precipitates in a 2.25Cr-1Mo-0.25V steel for large-scale cast-forged products*. Materials Characterization, vol. 58, pages 968–973, 2007.
- [Gao 98] N. Gao & T.N. Baker. *Austenite grain growth behaviour of microalloyed Al-V-N and Al-V-Ti-N steels*. ISIJ International, vol. 38, pages 744–751, 1998.

## BIBLIOGRAPHY

---

- [Geise 85] J. Geise & C.Z. Herzig. *Lattice and grain boundary diffusion of niobium in iron*. Metallkd., vol. 76, pages 622–626, 1985.
- [Gladman 66] T. Gladman. *On the theory of the effect of precipitate particules on grain growth in metals*. Proceeding of the Royal Society of London, vol. 294A, pages 298–309, 1966.
- [Gladman 92] T. Gladman. *Grain refinement in multiple microalloyed steels*. The Minerals, Metals and Materials Society, 1992.
- [Gladman 97] T. Gladman. *The physical metallurgy of microalloyed steels*. Cambridge : Univ. Press Cambridge, 1997.
- [Grest 90] G.S. Grest, M.P. Anderson, D.J. Srolovitz & A.D. Rollett. *Abnormal grain growth in three dimensions*. Scripta Metallurgica et Materialia, vol. 24, pages 661–665, 1990.
- [Hald 03] J. Hald & L. Korcakova. *Precipitate stability in creep resitant ferritic steels - Experimental investigations and modelling*. ISIJ International, vol. 43, pages 420–427, 2003.
- [Hillert 88] M. Hillert. *Inhibition of grain growth by second-phase particules*. Acta Metallurgica, vol. 36, pages 3177–3181, 1988.
- [Hong 02] S.G. Hong, K.B. Kang & C.G. Park. *Strain-Induced precipitation of NbC in Nb and Nb-Ti microalloyed HSLA steels*. Scripta Materialia, vol. 46, pages 163–168, 2002.
- [Hong 03] S.G. Hong, H.J. Jun, K.B. Kang & C.G. Park. *Evolution of precipitates in Nb-Ti-V microalloyed HSLA steels during reheating*. Scripta Materialia, vol. 48, pages 1201–1206, 2003.
- [Humphreys 95] F.J. Humphreys & M. Hatherly. *Recrystallization and related annealing phenomena (first edition)*. Elsevier Science Ltd., 1995.
- [Hyde 94] R.S. Hyde, G. Krauss & D.K. Matlock. *The effect of reheat treatments on fatigue and fracture of carburized*

- steels. SAE Technical paper N° 940788, vol. 103, pages 588–596, 1994.
- [Inoue 01] K. Inoue, N. Ishikawa, H. Ohnuma & K. Ishida. *Calculation of phase equilibria between austenite and (Nb,Ti,V)(C,N) in microalloyed steels*. ISIJ International, vol. 41, pages 175–182, 2001.
- [Irvine 67] K.J. Irvine, F.B. Pickering & T. Gladman. Iron and Steel Institute, vol. 205, page 161, 1967.
- [Kampmann 91] R. Kampmann & R. Wagner. *Materials Sciences and Technology: a comprehensive treatment*, Weinheim: VCH, 1991.
- [Kieffer 70] R. Kieffer, H. Nowotny, P. Ettmayer & M. Freudhofmeier. *Über die beständigkeit von übergangsmetallecarbiden gegen stickstoff bis zu 300 at*. Monatshefte für Chemie, vol. 101, pages 65–82, 1970.
- [Klinkenberg 04] C. Klinkenberg, K. Hulka & W. Bleck. *Niobium carbides precipitation in microalloyed steel*. Steel Research, vol. 75, pages 744–758, 2004.
- [Källqvist 00] J. Källqvist & H.O. Andrén. *Development of precipitate size and volume fraction of niobium carbonitrides in stabilised stainless steel*. Materials science and technology, vol. 16, pages 1181–1185, 2000.
- [Kuziak 95] R. Kuziak, T. Bold & Y-W. Chen. *Microstructure control of ferrite-pearlite high strength low alloy steel utilizing microalloying additions*. Journal of Materials Processing Technology, vol. 53, pages 255–262, 1995.
- [Leap 02] M.J. Leap & E.L. Brown. *Effects of composition and processing on development of grains coarsening resistance in cold forged and carburised steel*. Materials Science and Technology, vol. 18, pages 945–958, 2002.
- [Leapman 80] R.D. Leapman, P. Rez & D.F. Mayers. *K, L and M shell generalized oscillator strengths and ionization cross sections for fast electron collisions*. J. Chem. Phys., vol. 72, no. 2, pages 1232–1243, 1980.
- [Maazi 09] N. Maazi & R. Penelle. *Introduction of preferential Zener drag effect in Monte Carlo simulation of abnormal Goss grain growth in the Fe-3Si magnetic alloys*.

## BIBLIOGRAPHY

---

- Materials Science and Engineering A, vol. 504, pages 135–140, 2009.
- [MacKenzie 06] M. MacKenzie, A.J. Craven & C.L. Collins. *Nanoanalysis of very fine VN precipitates in steel*. Scripta Materialia, vol. 2006, pages 1–5, 2006.
- [Manohar 96] P.A. Manohar, D.P. Dunne, T. Chandra & C.R. Killmore. *Grain growth predictions in microalloyed steels*. ISIJ International, vol. 36, pages 194–200, 1996.
- [Martin 97] J.W. Martin, R.D. Doherty & B. Cantor. *Stability of microstructure in metallic systems*. Cambridge University Press, Second Edition 1997.
- [Maruyama 98] N. Maruyama, R. Uemori & M. Sugiyama. *The role of niobium in the retardation of the early stage of austenite recovery in hot-deformed steels*. Materials Science and Engineering, vol. A250, pages 2–7, 1998.
- [Maugis 05] P. Maugis & M. Gouné. *Kinetics of vanadium carbonitride precipitation in steel : A computer model*. Acta Materialia, vol. 53, pages 3359–3367, 2005.
- [Medina 99] S.F. Medina, M. Chapa, P. Valles, A. Quispe & M.I. Vega. *Influence of Ti and N contents on austenite grain control and precipitate size in structural steels*. ISIJ International, vol. 39, pages 930–936, 1999.
- [Messina 01] R. Messina, M. Soucail & L. Kubin. *Monte Carlo simulation of abnormal grain growth in two dimensions*. Materials Science and Engineering, vol. A308, pages 258–267, 2001.
- [Moon 07a] J. Moon, S. Kim, J. Lee & C. Lee. *Limiting austenite grain size of TiN-containing steel considering the particle size*. Scripta Materialia, vol. 56, pages 1083–1086, 2007.
- [Moon 07b] J. Moon, J. Lee & C. Lee. *Prediction for the austenite grain size in the presence of growing particles in the weld HAZ of Ti-microalloyed steel*. Materials Science and Engineering A, vol. 459, pages 40–46, 2007.
- [Narita 75] K. Narita. *Physical chemistry of the groups IVa (Ti, Zr), Va (V, Nb, Ta) and the rare earth elements in steel*. Transactions ISIJ, vol. 15, pages 145–152, 1975.

- [Onizawa 06] T. Onizawa, T. Wakai, M. Ando & K. Aoto. *Effect of V and Nb on precipitation behavior and mechanical properties of high Cr steel*. Nuclear Engineering and Design, 2006.
- [Ooi 06] S.W. Ooi & G. Fourlaris. *A comparative study of precipitation effects in Ti only and Ti-V Ultra Low Carbon (ULC) strip steels*. Materials Characterization, vol. 56, pages 214–226, 2006.
- [Padilha 99] A.F. Padilha, J.C. Dutra & V. Randle. *Interaction between precipitation, normal grain growth and secondary recrystallisation in austenitic stainless steel containing particles*. Materials science and technology, vol. 15, pages 1009–1014, 1999.
- [Perez 05] M. Perez. *Gibbs-Thomson effects in phase transformations*. scripta Materialia, vol. 52, pages 709–712, 2005.
- [Perez 08] M. Perez, M. Dumont & D. Acevedo-Reyes. *Implementation of classical nucleation and growth theories for precipitation*. Acta Materialia, vol. 56, pages 2119–2132, 2008.
- [Perez 09] M. Perez, V. Massardier & X. Kleber. *Thermoelectric power applied to metallurgy: principle and recent applications*. International Journal of Materials Research, vol. 100, pages 1461–1465, 2009.
- [Perrard 04] F. Perrard. *Caractérisation et modélisation de la précipitation du carbure de niobium et du cuivre dans les aciers bas carbone*. PhD thesis, Grenoble INPG, 2004.
- [Rios 87] P.R. Rios. *A theory for grain boundary pinning by particles*. Acta Metallurgica, vol. 35, pages 2805–2814, 1987.
- [Rollett 92] A.D. Rollett, D.J. Srolovitz, M.P. Anderson & R.D. Doherty. *Computer simulation of recrystallization-III: Influence of a dispersion of fine particles*. Acta metallurgica et materialia, vol. 40, pages 3475–3495, 1992.
- [Russell 68] K.C. Russell. *Nucleation in solid*. In *Phase Transformations*. papers presented at a seminar of the American Society for Metals, Oct. 12 and 13, 1968. Metal Park: American Society for Metals, pages 219–268, 1968.

## BIBLIOGRAPHY

---

- [Scott 01] A.J. Scott & R. Brydson. *Theoretical investigation of the ELNES of transition metal carbides for the extraction of structural and bonding information*. Physical Review B, vol. 63, pages 1–13, 2001.
- [Scott 02] C.P. Scott, D. Chaleix, P. Barges & V. Rebischung. *Quantitative analysis of complex carbo-nitride precipitates in steels*. Scripta Materialia, vol. 47, pages 845–849, 2002.
- [Sennour 02] M. Sennour. *Apport de la microscopie électronique en transmission et de la spectroscopie EELS à la caractérisation de nitrures (AlN, CrN) dans le fer et l'alliage Fe-Cr*. PhD thesis, INSA de Lyon, 2002.
- [Shahandeh 08] S. Shahandeh. *Developing a grain boundary particle pinning model using phase field method*. Rapport technique, Departement of Materials Engineering, The University of British Columbia, 2008.
- [Shimose 54] T. Shimose & K. Narita. *Tetsu-to-Hagané*. Iron and Steel Institute of Japan, vol. 40, pages 242–243, 1954.
- [Smith 62] R.P. Smith. Trans. A.I.M.E, vol. 224, page 190, 1962.
- [Speer 87] J.G. Speer, J.R Michael & Hansen. *Carbonitride precipitation in Niobium/Vanadium microalloyed steels*. Metallurgical Transaction A, vol. 18, pages 211–222, 1987.
- [Srolovitz 84] D.J. Srolovitz, M.P. Anderson, G.S. Grest & P.S. Sahni. *Computer simulation of grain growth - II. Grain size distribution, topology and local dynamics*. Acta Materialia, vol. 32, pages 793–802, 1984.
- [Stasko 06] R. Stasko, H. Adrian & A. Adrian. *Effect of nitrogen and vanadium on austenite grain growth kinetics of a low alloy steel*. Materials Characterization, vol. 56, pages 340–347, 2006.
- [Suwa 07] Y. Suwa, Y. Saito & H. Onodera. *Phase-field simulation of abnormal grain growth due to inverse pinning*. Acta Materialia, vol. 55, pages 6881–6894, 2007.
- [TCFE<sub>5</sub> 05] TCFE<sub>5</sub>. *Thermo-Calc Software. TCFE<sub>5</sub> - TCS Steel and Fe-alloys database version 5*, 2005.

- [Vega 06] M.I. Vega, S.F. Medina, A. Quispe, M. Gomez & P.P. Gomez. *Recrystallisation driving forces against pinning forces in hot rolling of Ti-microalloyed steels*. Materials Science and engineering, pages 253–261, 2006.
- [Wagner 91] R. Wagner, R. Kampmann & P.W. Voorhees. *Homogeneous second phase precipitation*. In KOSTORZ, Gernot (ed.). Phase transformation in materials. Weinheim : Wiley-VCH, 1991.
- [Weygand 98] D. Weygand. *Simulation numérique de la croissance de grains*. PhD thesis, Institut national Polytechnique de Grenoble, 1998.
- [Weygand 99] D. Weygand, Y. Bréchet & J. Lépinoux. *Zener pinning and grain growth: a two dimensional vertex computer simulation*. Acta Metallurgica, vol. 47, pages 961–970, 1999.
- [Williams 96] D.B. Williams & C.B. Carter. Transmission electron microscopy: paragraphs 32 to 35, volume IV. New York: Plenum Press, 1996.
- [Yu 03] Q. Yu & S. K. Esche. *A Monte Carlo algorithm for single phase normal grain growth with improved accuracy and efficiency*. Computational Materials Science, vol. 27, pages 259–270, 2003.
- [Zavaleta-Gutierrez 07] N. Zavaleta-Gutierrez, M.I. Luppó & C.A. Danon. *Heterogeneous austenite grain growth in ASTM A213-T91 steel*. ISIJ International, vol. 47, pages 1178–1187, 2007.
- [Zener 48] C. Zener. *private communication to C.S. Smith*. Trans TMS-AIME, vol. 175, page 15, 1948.

## BIBLIOGRAPHY

---

## APPENDIX A

### Preparation of TEM sample

In order to quantify the carbon and nitrogen content within precipitates, extraction replicas exempt from carbon (and nitrogen) have been made. A similar method has been used by Scott *et al.* [Scott 02] and Courtois *et al.* [Courtois 05], using replicas of non crystalline aluminium oxide. In our case, nano-crystalline aluminium replicas have been made. The preparation of these replicas is similar to that of carbon. However, the deposition is under a control argon atmosphere and not under vacuum as for the carbon, and aluminium electrodes are used. The method to prepare replicas is the following:

- The first step is to obtain a metallographic section. For samples that are embedded in a thermosetting resin. They are then mechanically polished on SiC paper with water at first, and then a polished diamond in thinner is made. Finally samples were rinsed with absolute ethanol and then dried to prevent oxidation. Finally, the coating is broken.
- The second step consists in an etching of the sample surface to dissolve the iron matrix and show the precipitates in relief. For this, we used Nital at 0.4 % (low concentration allows better control of the etching) and let sit for 10 seconds.
- The next step involves depositing by spraying an aluminium foil on the surface by plasma sputtering. Aluminium replicas have to be thin (~20 nm) for TEM observations. The equipment used is a secondary vacuum metallizing SCD 500 BALTEC (see figure A.1)
- The last step is the dissolution of the iron matrix to retrieve only the aluminium foil with precipitates. For this, we begin by scarifying, with a cutter, the sample surface and then immerse it in absolute ethanol and add 4 drops of nitric acid every hour until the film begins to delaminate. Then we grab the foil pieces with a copper grid. They are then rinsed

by passing through several bathes of ethanol and methanol. Finally the replicas are collected on copper grids and then dried for several hours before being stored in specialized boxes.

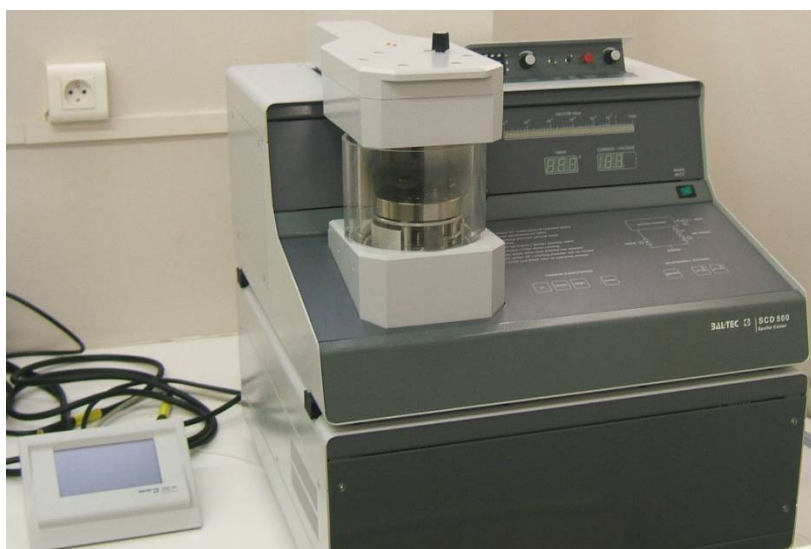


Figure A.1: *Secondary vacuum metallizing SCD 500 BALTEC*

Figure A.2 presents the schematic procedure to make aluminium extraction replicas.

The method presented here leads to the production of nano-crystalline aluminum foils as illustrated in Figure A.3.a. In order to avoid the presence of nano-crystalline aluminium, the original method used by Scott *et al.* [Scott 02] and Courtois *et al.* [Courtois 06] was to make oxidized foils. During our initial tests with the BALTEC installation a small amount of nitrogen and oxygen mixture was introduced in the deposition chamber. We have been able to obtain a very low crystalline deposits, significantly oxidized (see Figure A.3.b). EELS analysis presented on figure A.3.c clearly confirms the oxydation of the replica b) compared to the replica a). However, the implementation of these pulverizations has been quite restretive due to the very low deposition rate and potentially damaging for the metallizing (significant heating of the “head” housing aluminium targets). During these first tests we found that the deposition of pure aluminum, i.e. without oxygen introduction, does not prevent the detection of carbonitride precipitates in STEM-HAADF mode, due to their high contrast with the replica.

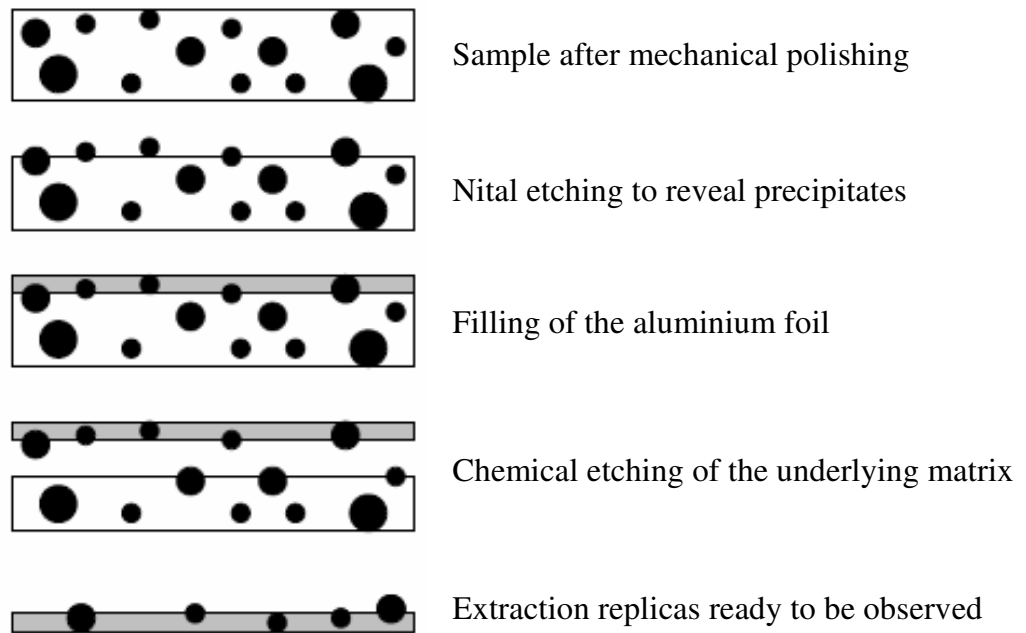


Figure A.2: *Schematic procedure of the preparation of aluminium replicas.*

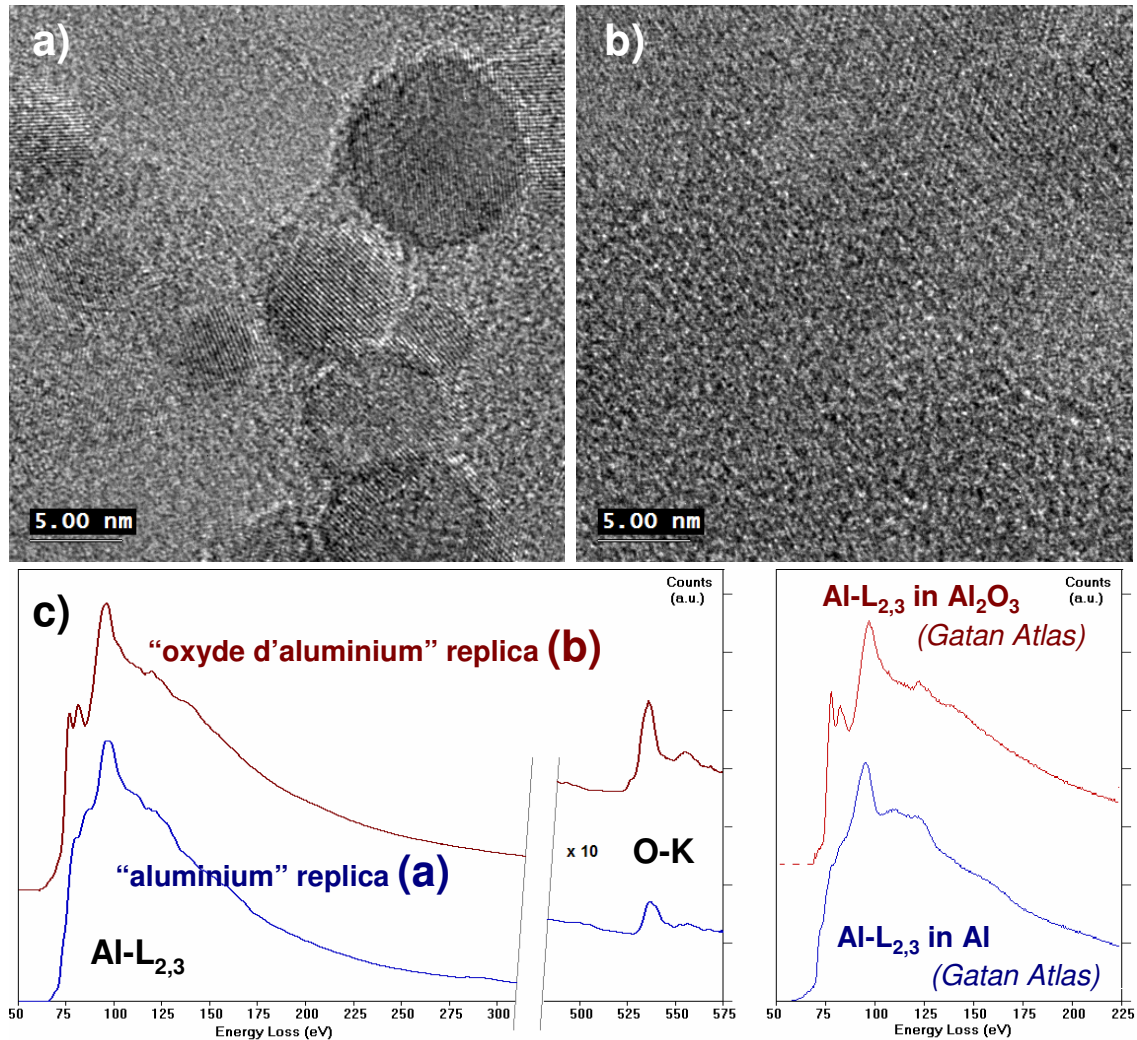


Figure A.3: Analysis of aluminium based replicas. a): typical microstructure of an aluminium replica; we clearly distinguish the nano-grains, which contain fringes of atomic planes. b): typical microstructure of an aluminium oxyde replica; nano-crystallization is less marked than in the case of a); c): comparison of EELS spectra of the replicas a) and b) (left) with the Gatan Atlas references for the Al-L<sub>2,3</sub> edge in alumina Al<sub>2</sub>O<sub>3</sub> and the metallic alluminium. We note that the replica b), which shows a significant presence of oxygen, presents an Al-L<sub>2,3</sub> edge very similar to that of the alumina reference, whereas the replica a) is clearly of type “metal” (although superficially oxidized).

## APPENDIX B

# Electrolytic dissolution

The electrolytic dissolution is a method commonly used at Ascometal to measure the content of precipitated elements in industrial grades. To realize this dissolution, we use a system constituted of a potentiostat, a platinum basket (cathode), the sample (anode) and a dissolution cell, in which the electrolytic solution is placed (see figure B.1).

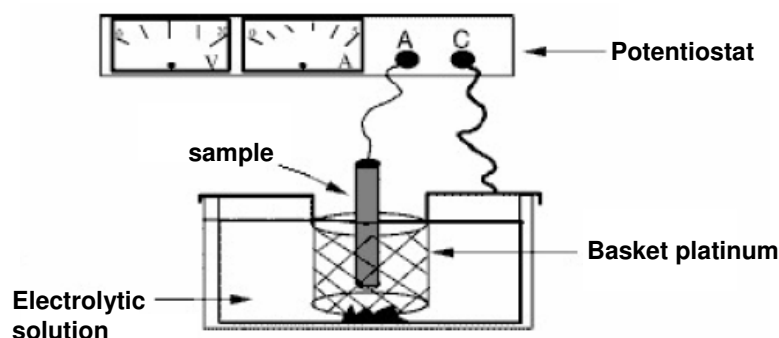


Figure B.1: *Scheme of the electrolytic dissolution system.*

The sample to be treated must have a square or circular section less than 10 mm width and its length should not exceed the height of the basket (here 50 mm). Before fixing the sample in its holder, it is cleaned to remove any oxide.

A too large current should be avoided because a too quick matrix dissolution leads to instabilities in the etching front (possible formation of iron “straws” that could imprison carbon).

The electrolyte used is a mixture of lithium chloride and salicylic acid in methanol. It is recommended not to exceed 10 g weight of sample dissolved in 2.5 l solution. Finally, the dissolution time is estimated from the Faraday law:

$$m = \frac{I \cdot t_d \cdot M}{e \cdot F} \quad (\text{B.1})$$

- où  $I$ : imposed intensity (A)  
 $t$ : electrolysis time (s)  
 $M$ : Fe molar mass ( $\text{g} \cdot \text{mol}^{-1}$ )  
 $F$ : Faraday constant = 96500 Coulomb  
 $e$ : electron number at stake during the reaction

A rough estimate can predict a dissolution time of about 10 hours a 1 g sample. The sample is weighed before and after the dissolution to determine the precise amount of dissolved material. After the matrix dissolution, precipitates are recovered by filtering the electrolyte solution on a grid (Nucleopore) of 0.2  $\mu\text{m}$  using a vacuum pump. The sample is then removed and immersed in methanol and passed through an ultrasonic tank to remove any residue. It is then filtered in the same way as the liquid electrolyte. The filter is washed several times with methanol and then dissolved in a solution of  $\text{H}_2\text{O}$ ,  $\text{HCl}$ ,  $\text{HNO}_3$ ,  $\text{HF}$  and  $\text{HClO}_4$ . This mixture is heated to perchloric fumes (white smoke) until the filter is completely dissolved.

For the determination of the precipitated phases, the residue is dissolved again in a mixture of  $\text{HNO}_3$  and then the  $\text{HF}$  solution is heated gently until a clear solution is got. Finally it is cooled at room temperature and then completed and homogenized.

The mineralized samples were analyzed by spectrometry in an Inductively Coupled Plasma (ICP) spectrometer with a SPECTRO CIROS CCD. Before analyzing the samples, a straight calibration must be made. In fact the measurement is made by comparing the measured intensity of a spectral line with the same line in a control sample containing a given concentration of element to be determined. Thus, several solutions of known concentration will be analyzed to construct the calibration points. The results are calculated by linear regression from the calibration points. The determination of real concentrations of the elements is done taking into account the dissolved sample mass during electrolysis.

## APPENDIX C

### Calculation of the $VC_xN_y$ equilibrium

For all phases,  $n_{Fe}$ ,  $n_V$ ,  $n_C$  and  $n_N$  are the atom quantities of iron, vanadium, carbon and nitrogen respectively. The total atom number is  $n = n_{Fe} + n_V + n_C + n_N$ . We define  $X_{Fe}$ ,  $X_V$ ,  $X_C$  and  $X_N$  as the mole fractions of iron, vanadium, carbon and nitrogen respectively.

We assumed that the regular solid solution is diluted ( $X_{Fe} \approx 1$ ,  $X_V \ll 1$ ,  $X_C \ll 1$  and  $X_N \ll 1$ ). The Gibbs energy of the matrix and the chemical potentials are given by:

$$G^{mat} = n_s G_{Fe:Va}^o + kT [n_{Fe} \ln \gamma_{Fe} + n_{Va} \ln \gamma_{Va} + n_V \ln \gamma_V + n_C \ln \gamma_C + n_N \ln \gamma_N] \quad (C.1)$$

$$\mu_{Fe}^{mat} = G_{Fe:Va}^o + kT \ln X_{Fe} \quad (C.2)$$

$$\mu_V^{mat} = G_{V:Va}^o + kT \ln X_V \quad (C.3)$$

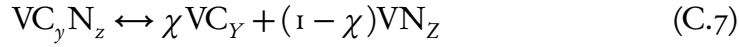
$$\mu_C^{mat} = \frac{1}{3} (G_{Fe:C}^o - G_{Fe:Va}^o) + \Omega_{VaC}^{Fe} + kT \ln \frac{X_C}{3} \quad (C.4)$$

$$\mu_N^{mat} = \frac{1}{3} (G_{Fe:N}^o - G_{Fe:Va}^o) + \Omega_{VaN}^{Fe} + kT \ln \frac{X_N}{3} \quad (C.5)$$

Carbonitrides are assumed to be an ideal solid solution of  $VC_Y$  and  $VN_Z$ , both precipitates having a FCC structure. Let  $\chi$  be the fraction of  $VC_Y$  precipitates over the total number of precipitates:

$$\chi = \frac{n_{VC_Y}}{n_{VC_Y} + n_{VN_Z}} \quad (C.6)$$

Assuming the global composition of the precipitates being  $VC_yN_z$ , we have:



The Gibbs free energy of carbonitrides is then:

$$G^{VC_yN_z} = n_{VC_Y} G_{VC_Y} + n_{VN_Z} G_{VN_Z} + kT n_p [\chi \ln \chi + (1 - \chi) \ln(1 - \chi)] \quad (C.8)$$

with:

$$G^{VC_Y} = (1 - Y)G_{V:Va}^o + YG_{V:C}^o + Y(1 - Y)\Omega_{VaC}^V + kT [((1 - Y) \ln(1 - Y) + Y \ln Y)] \quad (C.9)$$

$$G^{VC_Z} = (1 - Z)G_{V:Va}^o + YG_{V:N}^o + Z(1 - Z)\Omega_{VaN}^V + kT [((1 - Z) \ln(1 - Z) + Z \ln Z)] \quad (C.10)$$

Transferring  $(1 + y + z)dn$  atoms or  $dn$  molecules of  $VC_yN_z$  from the solid solution to the precipitates will change the Gibbs energy of the solid solution by:

$$-dG_n^{mat} = dn \frac{\partial G_n^{mat}}{\partial n_V} + y dn \frac{\partial G_n^{mat}}{\partial n_C} + z dn \frac{\partial G_n^{mat}}{\partial n_N} \quad (C.11)$$

and will change the precipitates Gibbs energy by:

$$dG_n^{VC-yN_z} = \chi dn \frac{\partial G_n^{VC-yN_z}}{\partial n_{VC_Y}} + (1 - \chi) dn \frac{\partial G_n^{VC-yN_z}}{\partial n_{VN_Z}} \quad (C.12)$$

At equilibrium, the global energy of the system will not change ( $dG_n^{mat} + dG_n^{VC-yN_z} = 0$ ) leading to:

$$\begin{aligned} (G_{V:Va}^o + \Omega_{FeV}^{Va} + kT \ln X_V) + y \left( \frac{1}{3} (G_{Fe:C}^o - G_{Fe:Va}^o) + \Omega_{VaC}^{Fe} + kT \ln \frac{X_C}{3} \right) \\ + z \left( \frac{1}{3} (G_{Fe:N}^o - G_{Fe:Va}^o) + \Omega_{VaN}^{Fe} + kT \ln \frac{X_N}{3} \right) \\ = \chi (G_{VC_Y} + kT \ln \chi) + (1 - \chi) (G_{VN_Z} + kT \ln(1 - \chi)) \end{aligned} \quad (C.13)$$

which is equivalent to:

$$\chi \Delta G_{VC_Y} + (1 - \chi) \Delta G_{VN_Z} + \chi kT \ln \left[ \frac{3^Y \chi}{X_V X_C^Y} \right] + (1 - \chi) kT \ln \left[ \frac{3^Z (1 - \chi)}{X_V X_N^Z} \right] = 0 \quad (C.14)$$

with  $\Delta G_{VC_Y} = G_{VC_Y} - (G_{V:Va}^o + \Omega_{FeV}^{Va}) - Y((G_{Fe:C}^o - G_{Fe:Va}^o)/3 + \Omega_{VaC}^{Fe})$  and  $\Delta G_{VN_Z} = G_{VN_Z} - (G_{V:Va}^o + \Omega_{FeV}^{Va}) - Z((G_{Fe:N}^o - G_{Fe:Va}^o)/3 + \Omega_{VaN}^{Fe})$ . The last equation can be expressed as follow:

$$\chi F + (1 - \chi)G = 0 \quad (C.15)$$

with:

$$F = \Delta G_{VC_Y} - kT \ln \left[ \frac{X_V X_C^Y}{3^Y \chi} \right]$$

$$G = \Delta G_{VN_Z} - kT \ln \left[ \frac{X_V X_N^Z}{3^Z (1 - \chi)} \right]$$

The global energy of the system has also to remain constant for a small change in  $\chi$ , which means that the derivative of the equation C.15 with respect to  $\chi$  has to be zero, giving:

$$F - G = 0 \quad (C.16)$$

Combining the last equation and equation C.15 gives:  $F = G = 0$ , leading to:

$$\Delta G_{VC_Y} = kT \ln \left[ \frac{X_V X_C^Y}{3^Y \chi} \right] \quad (C.17)$$

$$\Delta G_{VN_Z} = kT \ln \left[ \frac{X_V X_N^Z}{3^Z (1 - \chi)} \right] \quad (C.18)$$

Two solubility products can then be defined:

$$K_{VC_Y} = 3 \exp \left[ \frac{\Delta G_{VC_Y}}{kT} \right] = \frac{X_V^e X_C^{eY}}{3^{Y-1} \chi} \quad (C.19)$$

and

$$K_{VN_Z} = 3 \exp \left[ \frac{\Delta G_{VN_Z}}{kT} \right] = \frac{X_V^e X_N^{eZ}}{3^{Z-1} (1 - \chi)} \quad (C.20)$$